Diffusive Acoustic Confocal Imaging System (DACI): A novel method for prostate cancer diagnosis

by

Wen Yin
Bachelor of Engineering, Shanghai Maritime University, 2011

A Thesis Submitted in Partial Fulfillment
of the Requirements for the Degree of

MASTER OF APPLIED SCIENCE

in the Department of Mechanical Engineering

Supervisory Committee

Diffusive Acoustic Confocal Imaging System (DACI): A novel method for prostate cancer diagnosis

by

Wen Yin
Bachelor of Engineering, Shanghai Maritime University, 2011

Supervisory Committee

Dr. Rodney Herring (Department of Mechanical Engineering)
Supervisor

Dr. Barbara Sawicki (Department of Mechanical Engineering)
Departmental Member

Abstract

This thesis is part of the project undertaken to develop a diffusive acoustic confocal imaging system (DACI) that aims to differentiate between healthy and the diseased tissues in the prostate. Speed of sound is chosen as the tool to quantify the alterations in the tissues' mechanical properties at different pathological states.

The current work presents a scanning configuration that features three components: an acoustic emitter, a focusing mirror and a point receiver. The focusing mirror brings the collimated acoustic beam from the emitter into a focused probe position, which needs to be located within the bladder or at the near surface of the prostate. This position is introduced as the virtual source, where the acoustic intensity diffusively scatters into all directions and propagates through the specimen.

The system design was simulated using ZEMAX and COMSOL to validate the concept of the virtual source. Lesions in a phantom prostate were found in the simulated amplitude and phase images. The speed of sound variation was estimated from the 1D unwrapped phase distribution indicating where the phase discontinuities existed.

The measurements were conducted in a water aquarium using the tissue-mimicking prostate phantom. Two-dimensional projected images of the amplitude and the phase distributions of the investigating acoustic beam were measured. A USRP device was set up as the signal generation and acquisition device for the experiment. Two different signal extractions methods were developed to extract the amplitude and the phase information. The experimental results were found to generally agree with the simulation results.

The proof-of-concept design was successful in measuring both the phase and the amplitude information of the acoustic signal passing through the prostate

phantom. In future, the 2D/3D speed of sound variation needs to be estimated by an appropriate image reconstruction method.

Table of Contents

List of Tables

List of Figures

List of Acronyms

ADC: analog-to-digital converter

AVR: a family of microcontrollers developed by Atmel.

BPH: benign prostatic hyperplasia

CIRS: Computerized Imaging Reference Systems, Inc.

COMSOL:powerful platform for physics-based simulations

CT: computed tomography

DAC: digital-to-analog converter

DACI: diffuisve acoustic confocal imaging system

DDC: digital down-converter

DFT: discrete Fourier transform

DRE: digital rectal exam

DSP: digital signal processing

DUC: digital up-converter

FFT: fast Fourier transform

FPGA: field programmable gate array

GUI: graphical user interfaces

I/Q: in phase and quadrature

IDFT: inverse discrete Fourier transform

IF: intermediate frequency

IFT: inverse Fourier transform

ISR: interrupt service routine

LFRX: low frequency reception daughterboard

LFTX: low frequency transmission daughterboard

LO: local oscillator

MRI: magnetic resonance imaging

MTU: maximum transmission unit

NCO: numerically control oscillator

NEMA: National Electrical Manufacturers Association

PET: positron emission tomography

PSA: prostate-specific antigen

RF: radio frequency

SDR: software defined radio

SPL: sound pressure level

TOA: time of arrival

TRUS: transrectal ultrasound

USRP: universal software radio peripheral

ZEMAX: an optical design software

List of Symbols

c_l	speed of sound in a liquid or gas	$[m/s\ ]$
ρ_l	density of the liquid or gas	$[kg/m^3]$
κ_l	compressibility of the liquid or gas	$[m^2/N]$
K_l	bulk modulus of the liquid or gas (inverse of κ_l)	$[N/m^2]$
K	bulk modulus	$[N/m^2]$
G	shear modulus of the solid material	$[N/m^2]$
E	Young's modulus	$[N/m^2]$
ν	Poisson's ratio	
c_s	speed of sound in a solid material	$[m/s]$
ρ_s	density of a solid material	$[kg/m^3]$
c_T	propagation speed of transverse wave	$[m/s]$
p	acoustic pressure	$[Pa]$
∇	gradient operator	
$\boldsymbol{r}$	position vector	
k	wavenumber	$[rad/m]$
ω	angular frequency	$[rad/s]$
λ	wavelength	$[m]$
T	period	$[s]$
f	frequency	$[Hz]$
φ	phase	$[rad]$

φ_{tot}	total phase variation of the wavefront	$[rad]$
L	path length of acoustic beam	$[m]$
Z	acoustic impedance	$[kg/s \cdot m^2]$
I	instantaneous acoustic intensity	$[W/m^2]$
L_p	sound pressure level	$[dB]$
η	the material on either side of the material discontinuity	
θ_i	angle of incidence	$[deg]$
θ_t	angle of transmission	$[deg]$
θ_r	angle of reflection	$[deg]$
α	amplitude attenuation coefficient	$[Np/m]$
α_{dB}	attenuation attenuation in decibel	$[dB/m]$
α_R	intensity reflection coefficient	
R	pressure reflection coefficient	
α_T	intensity transmission coefficient	
θ_{crit}	the critical angle of incidence	$[deg]$
θ_{intro}	angle of intromission	$[deg]$
$\Delta\varphi$	phase discontinuity between transmission and reception	$[deg]$
D	diameter of the emitter	$[cm]$
F	Fresnel zone distance	$[cm]$
Ω	beam width of the acoustic ray from the emitter	$[deg]$
$s(t)$	a time signal	
$\phi(t)$	the phase of a signal	
f_c	center frequency	$[Hz]$

$\mathcal{F}\{\cdot\}$	Fourier transform operator	
$\mathcal{F}^{-1}\{\cdot\}$	Inverse Fourier transform operator	
N	the decimation/interpolation factor	
FL	frame length used in the USRP	
f_s	master clock rate in the USRP	$[MS/s]$
f_s/N	baseband sampling frequency	$[Hz]$
T_{sto}	the time period of data streaming assigned by the USRP	$[s]$

Acknowledgments

Upon the completion of this thesis, I feel like this is a great opportunity to look back at the past few years. The equipment in the lab, the simulation models, the collected data and so on recalled the moments I felt excited for a little progress, the tears for the struggles and the ordinary everyday life as a graduate student. I am grateful that my research ability and writing skill have been improved through the studies. More importantly, I have learnt that one's faith, attitude and willpower determine who he or she is. I would like to take this opportunity to acknowledge the contribution of the people I encountered in the University of Victoria who have offered their selfless help to me.

First and foremost, I would like to express my deepest gratitude towards my supervisor, Professor Rodney Herring. It has been a great honor to work on this project to make it possible to save men's life. His passion in the research field truly influenced me. He is very goal-oriented and always emphasizes the goal is to measure the phase. His thoughtful ideas and advice guided me towards the final step of this research. His trust in me greatly encouraged me to move forward, especially when I was having difficulties writing up my thesis.

Next, I would like to thank my committee members, Dr. Barbara Sawicki and Dr Adam Zielinski, for their time and valuable comment on my thesis. Dr. Sawicki's extensive knowledge in the field of computed tomography and medical imaging brought more insight to this project. She has known this project and the related preceding work for so long that she can always come up with many constructive suggestions. Dr. Zielinski's course, Underwater Acoustics, gave me a fundamental understanding of the acoustic wave propagation behaviour in various media.

I have been lucky to receive favors from other research engineer and faculty staff at UVic in the process of building the diffusive acoustic confocal imaging system. Thank you to Dr. Peter Jacqueman, one of the members in our research

group who put tremendous effort into this project. He participated in the layout design of the system and the improvement of the graphic user interface. He also built the electronic amplifier circuit to enhance the signal. Thank you to Kevin Jones for your suggestions about choosing the appropriate microstepping driver. Thanks to all the members in Dr. Herring's research group for their insightful questions and valuable suggestions. In addition, the knowledge sharing of their work broadened my perception in my own work.

I would like to thank my parents and my grandmother, who may not fully understand the reason I decided to pursue this path but still offer continuous support both financially and spiritually. I would like to thank my dear friends both in Canada and in China for keeping me inspired over the years. Last, but not the least, thank you to Haijia Zhu for being by my side. I would not have made it through without his support.

Chapter 1 Introduction

1.1 Problem Statement

In 2017, there are 21,300 Canadian men estimated to be diagnosed with prostate cancer [1]. As a matter of fact, prostate cancer has been found to be the most frequently diagnosed cancer among men in both the United States [2] and Canada [1]. The digital rectal exam (DRE) and the prostate-specific antigen (PSA) blood test are often performed as the preliminary tests. If cancer is suspected, a further imaging method will be recommended. For example, the biopsy guided by the transrectal ultrasound (TRUS) is commonly used for the prostate cancer detection and staging. The needle of the biopsy can only reach the posterior zone of the prostate gland so that the result accuracy will be influenced by the samples collected. Also, patients may experience side effects after the biopsy such as soreness, bleeding or inflammation. Magnetic Resonance Imaging (MRI) is another imaging method used to visualize the prostate and localize the lesions. It shows detailed information about the tissue structures but is expensive and time-consuming. In 2016, the FDA has approved the positron emission tomography/computed tomography (PET/CT) scan used for the recurrent prostate cancer diagnosis [3]. It was proven to be able to characterize the diseases with structural and functional information of the tissues and the cells [4]. Since it uses radioactive imaging technique, specialists are required to ensure the safety during the scanning process. Each imaging method has its own benefits and limitations. A non-invasive, fast, cost-effective and easy-to-use imaging method is still in high demand to be used as a routine test for prostate disease diagnosis.

Acoustic wave imaging, which is non-invasive to the human body, has achieved wide and sophisticated application in medical imaging over the past four decades. Even if it has several other forms of application, it is often considered synonymously with ultrasound imaging. For example, TRUS sends sound waves

from the rectum into the prostate to pick up the echoes for imaging. However, the intensity distribution that TRUS collected can just show the outline of the prostate gland without displaying the detailed internal structure and surrounding tissues of the prostate. Owing to the low sensitivity of the greyscale image TRUS provides, the malignant tumors appear to overlap with benign tumors as a hypoechoic focal lesions [5]. Therefore, TRUS is used to check the prostate size rather than finding the tumor location. If a new acoustic imaging method could be developed to distinguish the cancerous and non-cancerous tissues, then it could provide the potentiality as a reliable and safe solution for prostate cancer detection.

Mechanical properties such as the elasticity of biological tissues can be used as a diagnostic tool. For instance, DRE is a physical palpation exam used for early detection of prostate cancer where doctors insert a gloved finger into the rectum to sense any abnormalities in size, shape and texture of the prostate. In fact, studies have demonstrated that the mechanical characteristics of benign and malignant prostatic tissues are different [6]. Tissues stiffen with disease due to the depletion of collagen. The speed of sound, which is related to tissue compressibility and density, is different between tumors and healthy regions. Thus, the speed of sound variation of the acoustic beam propagating through the biological tissues can provide useful information regarding the presence or absence of tumors.

1.2 Motivation

The understanding of the nature of acoustic wave propagation in soft biological tissues is fundamental to developing an approach for quantifying the speed of sound. When an acoustic wave interrogates the biological tissue, the speed of sound varies with the composition of the tissue. The phase variation of the wavefront of the interrogated acoustic beam is accumulated along the travel path from the source to the detector and proportional to the speed of sound. If there is any material discontinuity existing along the path, the acoustic beam may

experience an abrupt phase shift at the interface between the healthy and diseased tissues according to the laws of reflection and transmission. This phase shift of the acoustic wave gives a hint where the tissue discontinuity lies and can be extracted concurrently with the intensity distribution by signal processing.

Another consideration of this project is how to develop an imaging modality that can fulfill practical clinical examination. The design layout of the new imaging system is expected to be developed as a prototype used as a routine examination tool on the patients in the future. More specifically, the investigating acoustic beam is brought into focus within the human body and the intensity at this focal point diffusively scatters in all directions. Our method is to detect the change in the acoustic beam scattered from the focusing probe position. Scattering is known as a very common phenomenon during the propagation of acoustic waves. Conventionally, the scattered acoustic signal in the human body is always considered difficult to interpret due to the complex structure of biological tissues [7]. On the other hand, the scattering signal contains valuable information regarding the tissue's structures.

This thesis is undertaken to design a new diffusive acoustic confocal imaging system (DACI) that can measure both the amplitude and the phase variation of the acoustic signal passing through the prostate specimen. To obtain a more practical scanning configuration, a scattering signal from the focusing probe position is collected for analysis. With the relationship between the phase variation and the speed of sound variation being closely investigated, this system is demonstrated to have the ability to distinguish the changes in the mechanical properties of the tissues at different pathological states.

1.3 Objective

The following summarizes the objectives in the process of developing DACI and the main new features of the imaging system which makes it different from the previous work:

- **Present a new design layout for more practical use.** The new design layout presented is developed to achieve a more practical configuration that can ensure the patient's comfort during the scanning process. This new design requires three components immersed in the water, including a piezoelectric emitter, a focusing mirror and a point detector. The tissue-mimicking prostate phantom representing the patient being examined can stay stationary.
- **Simulate the DACI design using COMSOL and ZEMAX.** Based on the ray acoustic theory, the propagation of the acoustic wave from the emitter through the prostate phantom to the detector is simulated in ZEMAX and the concept of the acoustic intensity scattering from the focal point is demonstrated to be sufficient to carry the phase information. Next, a finite element model of the prostate phantom was created and evaluated in COMSOL to investigate the behavior of sound transmission in the human body. The phase shift at the material discontinuities and the total phase variations along the propagation path from the source to the detector of the simulation results are studied to explore the correlation with the location of the lesions.
- **Improve the detection of phase variation.** Software defined radio (SDR) technology is applied to build the Ethernet-based universal software radio peripheral (USRP) platform capable of the real-time signal transmission and reception concurrently. The transmitted signal and the received signal can be synchronized to improve the accuracy of the experimental results. Also, the high sampling frequency feature of the USRP is explored to be implemented in the signal generation and data acquisition process of the system. More importantly, two methods to extract the phase measurement from the experimental data are studied based upon the signal representation used in the USRP.

1.4 Thesis Outline

The research described in this thesis is a component of a large-scale project involving the development of an acoustic imaging system for prostate cancer detection. To better anchor the simulation results and data analysis, the thesis will be organized in the following manner:

- Chapter 2 reviews the history of acoustic waves used for medical imaging and the studies that investigated how the acoustic propagation behavior in the soft biological tissues is affected by the alteration of the mechanical properties. The basic physics of the acoustic wave is introduced and the boundary behavior at the interface of material discontinuity is studied.
- Chapter 3 presents the current design layout of DACI and explains the principle behind it. It focuses on how the newly built Ethernet-based USRP platform realizes the real-time control of the acoustic signal transmission and reception simultaneously. The concept of the USRP hardware implementation is described and the frame synchronization technique is explained. Also, the ability to extract both phase and intensity distributions from the received signal is proven. Finally, the principle of the phase detection method applied in this research is presented.
- Chapter 4 presents the simulation models created using ZEMAX and COMSOL to simulate the design of DACI. The concept of the virtual source is demonstrated viable, and the scattered intensity from the virtual source position is sufficient to carry the phase information. The locations of lesions are found via both the amplitude and the phase distributions. The 1-D speed of sound variation is estimated from the phase information and abrupt shifts are found to occur at the locations where material discontinuity interfaces exist.
- Chapter 5 covers the setup of the experimental apparatus. The control over the point receiver rotation stage and the specimen linear translation stage is

explained. The parameters in the USRP N210 are set up according to the theoretical background explained in Chapter 3. The alignment of each component is conducted following the design layout presented in Chapter 3.

- Chapter 6 first explains how the speed of sound in the water aquarium is measured as a reference. The impact of the baseband sampling frequency of the USRP platform is analyzed by taking the measurement of the prostate phantom at a fixed position. Then, the 2D projected image measured through the tissue-mimicking prostate phantom are investigated. Basically, the measured phase data of one projection agrees with the simulation results.
- Chapter 7 summarizes the results of current work. The tasks that have been achieved are discussed, and the future work that can be done are proposed. The future prototype design of DACI for the diagnosis of both the prostate cancer and the ovaries cancer is presented and their applications as routine examination tools are suggested.

Chapter 2 Background Information

The key of disease diagnosis focuses on how to differentiate the healthy tissues with the diseased tissues within or surrounding of the region of interest in human body. The variations in the mechanical properties that different tissues present when being interrogated by the acoustic beam enable the possibility of acoustic imaging as a non-invasive diagnosis tool. Due to the inhomogeneity of biological tissues, the interaction mechanism between sound and tissues is complicated and is still under investigation.

This chapter briefly introduces the development history of acoustic imaging and the basics of acoustic wave, giving an overall view about how acoustic wave can be used as a tool for the diagnosis of prostate cancer. The anatomy and pathohistology of the prostate are discussed for reference purposes. The basic physics of acoustic wave and the way it interacts with the supporting medium are detailed. The boundary behavior of the acoustic beam is also investigated.

2.1 Literature Review

2.1.1 Early History of Acoustic Imaging

Acoustics is known as the science term for sound. While the history of acoustics study can be traced back to the 16th century [8], Issac Newton was the first to present the theory that sound propagates as a wave in Principia 1968. The monument to modern acoustics development is often credited towards the epic masterpiece *The Theory of Sound* [9] by Lord Rayleigh, which systematically articulates the knowledge of previous studies and his own critical contribution.

The Curie brothers discovered piezoelectricity in 1880, a breakthrough that leads to the following emergence of ultrasound technology in various fields [10]. In 1916, Langevin and Chilowsky developed an echo-sounding device using high frequency signal to detect the sinking submarine, known as "hydrophone", which was considered as the foundation of the pulse-echo technique used in the naval

and military industry. In 1935, the first radio detection and ranging (radar) was developed by Watson-Watt to detect the aircraft. Sokolov proposed the idea of using transmission ultrasound and reflective method for flaw detection in solids in the year of 1928. And early in 1940, Firestone [11] applied the pulse-echo technique for metal flaw detection and measurement.

The first attempt to apply ultrasound for diagnostic medical imaging was not realized until 1940s by Dussik brothers with the use of transmission ultrasound wave through brain to locate tumors [12]. During the period between late 1940s and early 1950s, there were a few pioneering progresses in the implementation of ultrasound imaging. In late 1940s, Ludwig was able to apply the A-scan (Amplitude-scan) ultrasonic pulse-echo technique utilized extensively in radar and sonar systems to characterize animal tissues and proposed the possibility of localizing the gallstones in tissues [13]. In his work published in 1950, Ludwig was able to measure the speed of sound through various animal tissues and human living tissues using two different frequencies, 1.25 MHz and 2.5 MHz. The characteristic acoustic impedances of the various tissues were calculated from the measured speed of sound and density [14]. Wild and Neal also worked on an A-scan ultrasonic apparatus in 1951 to measure the breast specimen and found diseased tissues appeared more echogenic [15].

Another ultrasound imaging method, B-scan (brightness-scan), was developed to produce two-dimensional visualization of the biological structures of the tissues. In the year 1952, Wild and Reid developed a B-mode scanning device using echo-ranging technique for breast tumor visualization in 1952 [16, 17] and were able to produce the real-time image of the scanning result at the frequency of 15MHz in 1953 [18]. In 1952, Howry, along with Bliss and Posakony, also developed a linear B-mode imaging device and was able to demonstrate the detection of tissue interfaces and structures by ultrasound echoes [19]. In 1950s and 1960s, Howry and Holmes worked on the electronic hardware development of the B-scan instrument to visualize the internal anatomic structure and pathological lesions in

human body [20-22]. Their great contributions paved the foundation for the current ultrasound imaging devices.

In 1973, George Kossoff *et al.* developed a scanner converter with grey scale signal processing abilities [23]. The different intensities of reflected echoes were able to display the morphological structure of soft tissues. The discovery of this imaging technique propelled the ultrasound technique to achieve outstanding progress since 1970s. Ever since then, non-invasive acoustic imaging using ultrasound waves has obtained extensive application in the medical practice field.

2.1.2 Speed of Sound vs Specific Tissue Components

Over these 40 years, a lot of studies have been conducted to explore the association between alterations in acoustic wave mechanical properties with tissue composition at normal and various diseased states. There are a few remarkable findings that prove the potentiality that acoustic wave carries valuable information regarding tissue characterization during the propagation process.

One of the most common parameters that have been studied for long time is the speed that acoustic wave propagates through tissue medium, known as speed of sound. Common tissue types include epithelial tissue, connective tissue, muscle, nerves. Collagenous fibers, the most abundant type of connective tissue, comprise about one third of proteins and function as essential structural tissue in human body. Its elastic modulus is 1000 times greater than other tissue constituents [24] and hence, the speed of sound in fibers and characteristic impedance mismatch between the collagenous and other tissues are increased. Therefore in the initial report of the study undertaken by Fields and Dunn [25], the amount of collagen concentration was assumed to dominate the elasticity and the acoustic impedance of the soft tissues. And an increase in the collagenous fibrous structure was discovered to enhance the contrast information on the echography due to the increased acoustic impedance mismatch. In 1977, O' Brien derived the relations that describes speed of sound as a function of tissue collagen concentration using

the frequency range of 1-10 MHz [26]. In another study conducted by Pohlhammer and O'Brien in 1980, they further confirmed the attenuation coefficient and the speed of sound of the interrogated wave are essentially the functions of the constituents concentrations, such as water, collagen, protein and fat [27]. Another step forward taken by Goss and O'Brien used scanning laser acoustic microscope (SLAM) at 100 MHz to directly quantify the speed of sound within the mammalian threads. Their measurement demonstrated the accuracy of the relationship function between the speed of sound and the collagen concentration derived by O' Brien [28] and further supported the hypothesis that the collagenous fibrous structure influences the echographic visualization. Goss and Dunn conducted an experiment to study the relationship between the speed of sound and the collagen concentration varying from 0.07 % to 0.7 % with the frequency of 8.87 MHz at the temperature 10 ℃ and 20 ℃, and discovered the speed exhibit higher linear dependence of the collagen concentration compared to globular protein [29]. All these researches showed that collagen is a key tissue constituent affecting the acoustic wave propagation behavior in soft biological tissues.

2.1.3 Current Techniques to Measure Speed of Sound

Bamber reviewed several techniques used to measure the speed of sound in biological tissues and categorized them into absolute and relative method [30]. Absolute methods refer to those that can directly output the measurement value without any other media as references. On the other hand, relative methods are those techniques measured with respect to a surrounding medium. Along with the development of acoustic imaging application, the speed of sound measurement methods correspondingly evolved with more accurate results by the scanning acoustic microscope and in vivo measurement in human organs such as female breasts. In essence, these methods are variations based on either time-of-flight or interferometer method. The travel distance of a pulsed acoustic wave, the time interval between transmission and reception and the geometry of transducer configuration are the important factors for calculation in time-of-flight methods.

Greenleaf *et al.* developed the time-of-flight transmission tomography method to measure the spatial distribution of the speed of sound within transverse section using algebraic reconstruction technique (ART) [31]. The reconstructed image, produced by Greenleaf and Bahn, suggested that the solid lesions and the carcinoma were associated with the increased speed of sound regions [32]. Due to the difference in mechanical properties, fat and collagen forms a relatively good contrast mechanism for tissue characterization. In fact, computed tomography (CT) ultrasound has become a standard diagnose routine in breast imaging. Speed of sound carries information about tissue constituents and alterations in pathological states. So far, speed of sound is demonstrated to be a useful parameter for diagnosing diseases.

But in terms of prostate cancer diagnosis, ultrasound imaging currently plays more of an aiding role rather than a deterministic tool. For example, TRUS can give the volume size information of the prostate gland as well as a guide for targeted biopsy. But due to the insufficient spatial resolution of grey-scale imaging, current ultrasound technology cannot recognize those inhomogeneous soft tissues with small size lesions. And this limited acoustic wave from taking up a more important role in the field of prostate cancer diagnosis.

2.2 Anatomy and Histopathology of Prostate

Prostate gland, located below the bladder and above the external urethra sphincter, is often divided into 4 regions: peripheral zone, central zone, transition zone and anterior fibromuscular stroma. Prostate gland tissues are not morphologically homogeneous. The gland is composed of epithelium tissues and the fibromuscular stroma is composed of connective tissues and smooth muscles. The glandular epithelium tissue is surrounded by the fibromuscular stroma. The pathological process of prostate can be summarized into four types: inflammation, atrophy, benign prostatic hyperplasia (BPH) and carcinoma. The peripheral zone comprises around 70% of the gross volume, and 70% of the prostate cancer

occurred within the peripheral zone and this is where palpation is targeted. The central zone, on the other hand, comprises about one fourth of the total volume, and only 10% of carcinoma arise from this zone [33, 34]. The transitional zone is sliced by the urethra and about 20% of the cancers are from this zone.

Collagenous fibers are the principal component of connective tissue and are presented with various morphologies in the three zones. The peripheral zone is comprised of fine collagenous fibers whereas the central zone is composed of coarser fibers. From the scanning electron microscope (SEM) images of the connective tissue of prostate at different pathological states captured by a Ireland group [35], it was found that the collagen fibers in the normal prostate are smooth and well differentiated. In the case of BPH, the proliferation of both the glandular epithelium and the connective tissues was detected. And the stroma at BPH state was found to be comprised of denser and thicker connective tissues. In prostatic carcinoma, the glandular tissue and the stroma were often hard to be differentiated due to the non-uniform distribution, swollen and destruction of collagen fibers. The proliferation of tumor cells can also result in larger nucleoli and the formation of metastasis, accompanied with the degradation of supporting collagen fibers. Histopathological studies of the prostate cancer reveal that the nuclei of tumor cells are more prominent compared to normal cells and the nuclei density increases with the tumor growth. The underlying histopathological progression is revealed by the morphological variation in the tissue structure, leading to the presence of alterations in the mechanical properties of prostate tissues. This forms the basis of a viable diagnosis method for prostate cancer by non-invasive characterization of the tissue compositions at normal and diseased states.

2.3 Basics of Sound Wave

To better serve the characterization purpose, the following brief introduction will cover the interaction mechanism between the acoustic wave and various media including the soft biological tissues.

2.3.1 Basic Physics of Sound

Sound is created by an oscillating source that disturbs some particles in the medium and then causes the adjacent particles to be displaced from the equilibrium state. The consecutive interactions of the particles in the medium carry the disturbance and transport the energy from the source location to another location. Sound wave is the disturbance that propagates through the medium, and is considered as a mechanical wave.

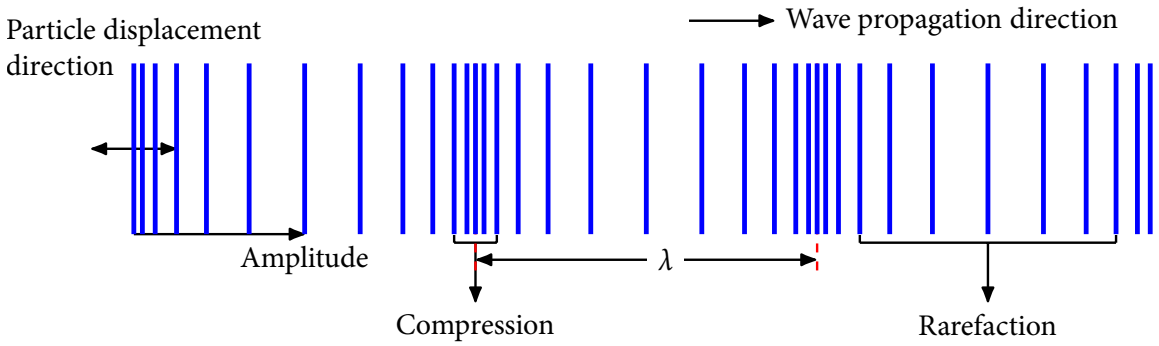

Figure 2.1 Longitudinal wave

The propagation of acoustic wave is often described in two typical forms, longitudinal and shear wave. The longitudinal, also known as compression wave, moves particles of a medium in the direction parallel to that the wave travels (see Figure 2.1), whereas the shear wave or transverse wave occurs when the particle displacement is perpendicular to the direction of wave propagation (see Figure 2.2). Longitudinal wave can propagate in all kinds of materials while shear wave cannot travel through fluid material since there is no enough shear strength to drive the perpendicular particle motion. The compression and the rarefaction regions shown in Figure 2.1 are caused by the back and forth motion of the displaced particles in the medium. And crest and trough regions shown in Figure 2.2 are where the particle displacement reaches positive and negative maximum.

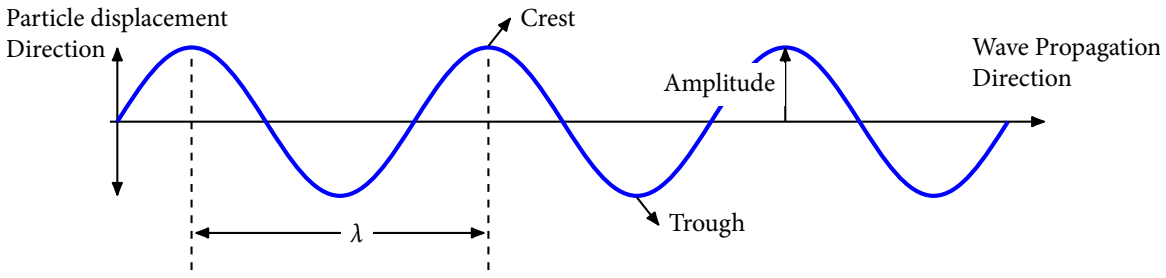

Figure 2.2 Transverse wave

No matter which type one wave is, there are a few common parameters to characterize the wave as following:

- Amplitude is the displacement measured from the equilibrium position to the maximum displacement position.
- Wavelength λ is the distance between repeating pattern to occur. For instance, the distance between the first and the second compression zone in longitudinal wave is one wavelength.
- Frequency f describes how fast that each particle is able to complete one cycle. It can be measured by the number of cycles that pass a fixed point within a certain time. The SI unit of frequency is hertz (Hz), and $1\ \text{Hz} = 1$ cycle/second. The frequency range within human hearing ability lies in between $20\ Hz$ to $20\ kHz$. An acoustic wave with the frequency over $20\ kHz$ is considered as ultrasound.
- Period T is the amount of time that the particle needs to finish the vibration of a whole cycle.

2.4 Speed of Sound in Various Media

The speed that a longitudinal acoustic wave propagates through the medium, referred as speed of sound in the remainder of this thesis, can be impacted by various factors, such as pressure and temperature. However, the main contributing factor taken into account in this project would be the constituent of the medium. This enables the possibility to track the change in the medium by measuring the speed of sound.

2.4.1 Fluid

Speed of sound, a scalar quantity, describes how fast the acoustic energy can be transmitted along the propagation direction. The speed of sound in a liquid or gas c_l is given by

$$c_l = \sqrt{\frac{1}{\rho_l \kappa_l}} = \sqrt{\frac{K_l}{\rho_l}} \tag{2.1}$$

where ρ_l is the density of the liquid, κ_l refers to the compressibility of the liquid. The bulk modulus K_l is the inverse of compressibility κ_l.

2.4.2 Solid

The speed of sound in a solid material is usually characterized by the shear modulus G, the Young's modulus E and the Poisson's ratio ν. The bulk modulus K and the shear modulus G can be expressed as follows [24]:

$$K = \frac{E}{(1+\nu)(1-2\nu)} \tag{2.2}$$

$$G = \frac{E}{2(1+\nu)} \tag{2.3}$$

where E is the longitudinal Young's modulus that describes the ratio of the longitudinal stress to the strain, and ν is the Poisson's ratio defined as the negative ratio of the lateral strain to the longitudinal strain.

Then the speed of sound that travels in a solid material is given by

$$c_s = \sqrt{\frac{K_s + \frac{4}{3}G}{\rho_s}} = \sqrt{\frac{E(1-\nu)}{\rho_s(1-2\nu)(1+\nu)}} \tag{2.4}$$

where K_s is the bulk modulus of the solid, G refers to the shear modulus of the solid medium which is the ratio of the shear stress to the shear strain, ρ_s refers to the density of a solid medium.

On the other hand, the transverse wave propagation speed is described as [7]

$$c_T = \sqrt{\frac{G}{\rho_s}} = \sqrt{\frac{E}{2\rho_s(1+\nu)}} \tag{2.5}$$

2.4.3 Soft Biological Tissues

In recent biomechanics study, soft biological tissues are often considered as viscoelastic solid material mainly because of the similarities in their mechanical properties [8, 24]. Since the shear modulus G of soft tissues is five orders smaller than the bulk modulus K, the Poisson's ratio ν can be approximated by

$$\frac{G}{K} = \frac{(1+\nu)(1-2\nu)}{2(1+\nu)} \approx 0 \rightarrow \nu \approx 0.5. \tag{2.6}$$

$$\frac{c_s}{c_T} = \sqrt{\frac{1-\nu}{0.5-\nu}} \approx \infty \tag{2.7}$$

In fact, a material with the Poisson's ratio of $\nu = 0.5$ is considered to be incompressible. Under this circumstance, the ratio of c_s to c_T can be found in Equation (2.7) by plugging the Poisson's ratio value 0.5. As a result, the longitudinal wave speed c_s is far greater the shear wave speed c_T in an incompressible material.

This research follows the assumption that the soft biological tissues are nearly incompressible with a Poisson's ratio $\nu = 0.495$ [24, 36]. In this case, the longitudinal wave speed is ten times greater than propagation speed of the shear wave.

Both propagation forms have obtained sophisticated research and application in medical imaging field. As one of the most well-known application example of longitudinal wave, ultrasound has been widely accepted as a routine exam to diagnose diseases since 1970s. In the frequencies range employed in ultrasound

imaging, usually in the order of MHz, the propagation process of shear wave can be neglected in soft tissues due to the acoustic absorptions. Elastography, using shear acoustic wave, has demonstrated its potentiality in medical diagnosis since 1990s. The main concern in our study is to characterize the mechanical properties tissues by measuring the speed of sound, which refers to the speed that the longitudinal wave propagates through the medium.

Measurements conducted through different soft tissue types have proved that the speed of sound varies with the composition. Duck reviewed the speed of sound through human tissues at different pathological states [37]. From the reported measurement summary, the speed of sound of human soft tissues varies in the range of $1412 - 1647$ m/s, and the density varies from 916 kg/m^3 (Fatty and adipose) to 1190 kg/m^3 (Skins). The published speed of sound measurement data of soft biological tissues is in the range of 1540 m/s. The average density of prostate gland is 1045 kg/m^3 [37], and 1040 kg/m^3 for urinary bladder. The speed of sound and density of several typical soft tissues are listed in Table 2.1 for reference purpose.

2.5 Wave Propagation

2.5.1 Wave Equation

Wave equation is a mathematical expression describes the phenomena how the wave passes through one medium to another, forming the basis of grasping the interaction mechanism between the wave and the medium. An example of a sinusoidal wave $p(x)$ at time instant t is shown in Figure 2.3.

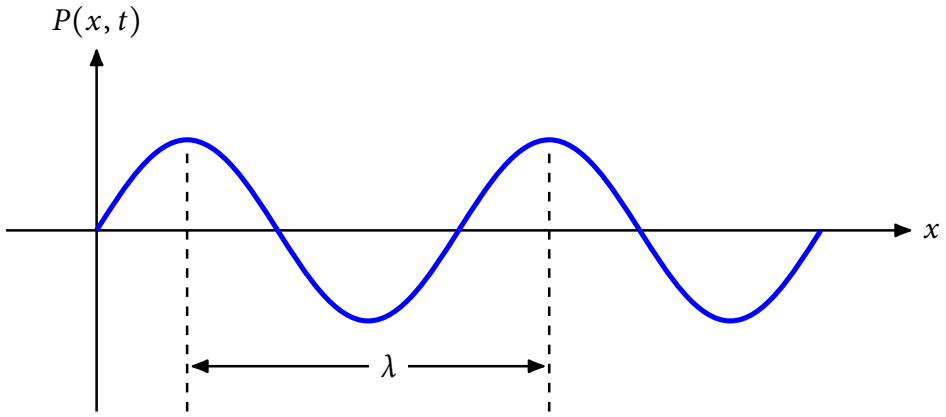

Figure 2.3 Harmonic wave propagating in x-direction at time instant t

The derivation of the wave equation requires the understanding of the equation of motion, the continuity equation and the constitutive equation. In a homogeneous lossless medium where the density ρ and the compressibility κ stay at the equilibrium state, the acoustic wave equation in the 3D Cartesian coordinates is given as [7]

$$\nabla^2 p - \frac{1}{c^2}\frac{\partial^2 p}{\partial t^2} = 0, \tag{2.8}$$

where ∇[1] is the gradient operator, and p is the acoustic pressure.

The solution to the wave equation is expressed as the superposition of sinusoidal waves as follows:

$$p(\boldsymbol{r}, t) = p e^{i(\boldsymbol{k}\cdot\boldsymbol{r} - \omega t)}, \tag{2.9}$$

where $\boldsymbol{r} = x\boldsymbol{i} + y\boldsymbol{j} + z\boldsymbol{k}$ is the position vector starting from the origin of the Cartesian coordinates, k is the wavenumber and ω is the angular frequency.

For a sinusoidal wave, the wavelength λ is the distance over which the peak repeats, shown in Figure 2.3. And the period T is the time for the peak to repeat. Then we have

$$\lambda = cT, \tag{2.10}$$

[1] In Cartesian coordinates, $\nabla \boldsymbol{p} = \frac{\partial p_x}{\partial x}\boldsymbol{i} + \frac{\partial p_y}{\partial y}\boldsymbol{j} + \frac{\partial p_z}{\partial z}\boldsymbol{k}$, where $\boldsymbol{i}, \boldsymbol{j}, \boldsymbol{k}$ are the unit vectors along x-, y- and z-directions.

where c is the speed that the sound wave propagates along a certain direction. And the acoustic frequency f equals $1/T$, we have:

$$c = f\lambda \tag{2.11}$$

The relationship between the wave number k and the angular frequency ω is expressed by

$$k = \frac{2\pi}{\lambda} \tag{2.12}$$

$$\omega = \frac{2\pi}{T} = k\frac{\lambda}{T} = kc \tag{2.13}$$

2.5.2 Phase

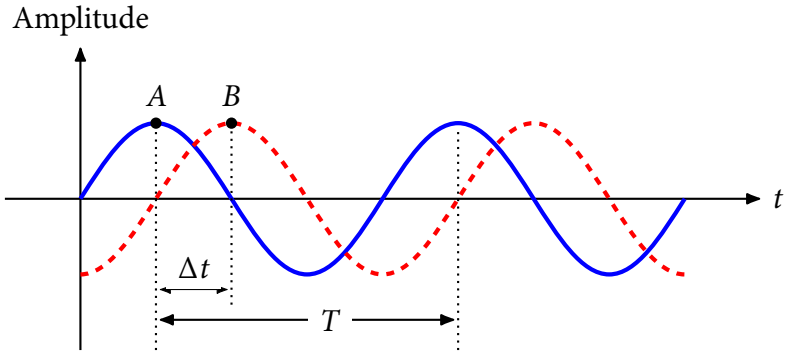

Figure 2.4 Difference of the same sinusoidal wave at two different time instants

Phase is another important parameter defining a sinusoidal wave. The amplitude tells how far the particle can reach out, the frequency tells how fast the particle along the wave can complete one cycle. Phase φ gives the information about the position of the particle at a certain time, measured in the unit of radian or degree. During the process while an acoustic wave completes a whole cycle, i.e., the distance a particle in the medium travels is one wavelength, the change in phase angle varies linearly from 0 to 2π. It can be inferred that the phase angle is related to the distance the wave propagates through the medium.

Phase shift, as the term implies, is the difference between the phase angle of two points of interest. The phase difference of the particle at the same position in a sinusoidal wave at different time is shown in Figure 2.4. The sinusoidal wave

represented by the solid line leads the other wave graphed in dashed line by time difference Δt. The phase shift is determined by the product of $2\pi\ radian$ and the ratio of time difference Δt over the whole period of the wave T, i.e.,

$$\Delta\varphi = 2\pi\frac{\Delta t}{T}. \tag{2.14}$$

If the total path length that the acoustic wave travels through the medium is L, then total phase variation φ_{tot} along the propagation process can be given as

$$\varphi_{tot} = \omega t = 2\pi\frac{L}{\lambda} = 2\pi f\frac{L}{c} \tag{2.15}$$

From Equation (2.15), the phase variation along the propagation path is found to be accumulated with the travel distance. If only one wave frequency is used, the total phase variation is linearly correlated with the ratio L/c. Therefore, the acoustic phase during propagation process carries important information about the speed of sound. Development of an imaging modality with the ability to detect both phase and amplitude information is the core task in this project. Phase measurement in details is elaborated in the next chapter.

2.5.3 Acoustic Impedance

If there is a material discontinuity in the medium during the wave propagation process, the trajectory of the original transmission path will be altered according to the differences between the two media. The interface where discontinuity occurs is termed as boundary in this thesis. In order to characterize the mechanical properties of the media on both sides of the boundary, the characteristic acoustic impedance Z is introduced. It is defined as $Z = \rho c$, expressed in the unit of $1\ Rayl = 1kg/s \cdot m^2$.

A list of characteristic impedance for soft biological tissues and other materials can be found in [38]. The acoustic impedance value of several typical soft tissues is listed Table 2.1. It can be found that connective tissue has relatively higher acoustic impedance due to higher density and speed of sound, whereas fat has the lowest value because of the adipose tissues.

Table 2.1 Acoustic impedance of typical human tissues [37]

Tissue Type	Speed of Sound (m/s)	Density (kg/m^3)	Acoustic Impedance $(MRayls)$
Kidney	1560	1050	1.638
Liver	1595	1060	1.690
Breast	1510	1020	1.540
Fat	1478	950	1.404
Connective	1613	1120	1.807
Muscle	1547	1050	1.624

2.5.4 Acoustic Intensity and Sound Pressure Level

The instantaneous acoustic intensity I in the unit W/m^2 is defined as the product of acoustic pressure p and the particle velocity u. It is found to be related to the acoustic pressure, the density and the speed of sound in the medium, shown in (2.16)

$$I = pu = \frac{p^2}{\rho c} \tag{2.16}$$

An alternative terminology used to describe the pressure level of an acoustic wave is the sound pressure level L_p in dB, a logarithmic measurement of the original pressure value.

$$L_p = 20 \log_{10}\left(\frac{p}{p_0}\right) \tag{2.17}$$

where $p_0 = 2{\times}10^{-5}\ Pa$ is the reference acoustic pressure.

2.5.5 Acoustic Attenuation

The acoustic attenuation describes the loss of acoustic energy over the travel distance L due to the acoustic absorption and scattering during the propagation process. The current acoustic intensity I with respect to the initial intensity I_0 can be expressed as follows [37]:

$$I = I_0 e^{-2\alpha L} \tag{2.18}$$

where α in the unit of neper per meter $[Np/m]$ is the amplitude attenuation coefficient, depending upon the acoustic frequency, pressure and temperature. The attenuation coefficient in decibel scale becomes

$$\alpha_{dB} = 20log_{10}(e) \cdot \alpha \approx 8.686\alpha \; [dB/m] \tag{2.19}$$

Its dependency of the acoustic frequency in the distilled water can be found via the following expression:

$$\alpha = a \cdot f^2 \tag{2.20}$$

where $a = 25 \times 10^{-15}$ $[Np/(m \cdot Hz^2)]$ in the distilled water at the temperature 20℃ [39].

2.6 Boundary Behavior

At the boundary between two media with different mechanical properties, the propagation of the acoustic wave diffusively scatters in all directions. Reflection and refractions are known as two special cases of diffuse scattering. Part of the energy will be transmitted into the other medium, while another part of the energy will be bounced off the interface.

2.6.1 Transmission and Reflection

An example that an acoustic beam encounters the interface between the water and the prostate phantom is illustrated in Figure 2.5, where η_1 and η_2 refer to these two distinct materials, and θ_i, θ_r and θ_t denote the angles that the incident, reflected and transmitted rays make with the normal line, respectively.

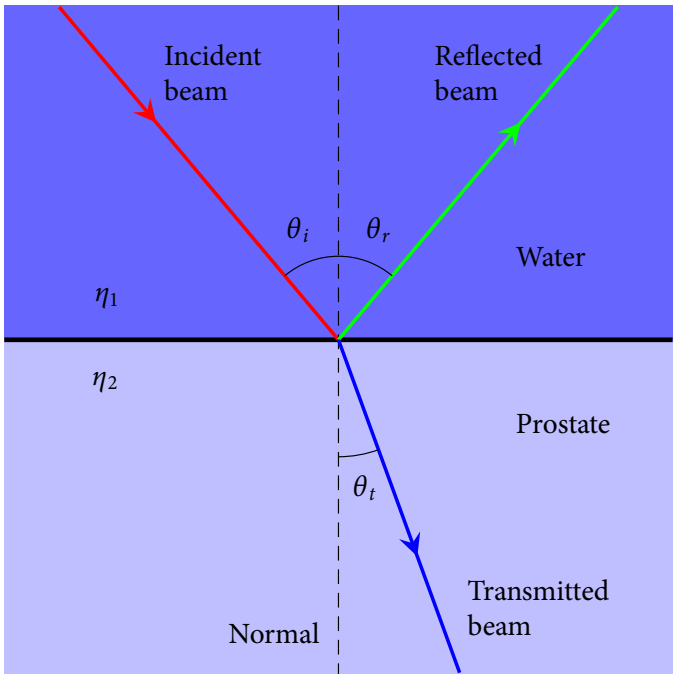

Figure 2.5 Transmission and reflection at material boundary

From the law of reflection, it can be found that $\theta_i = \theta_r$. As for the refraction, Snell's law is applied to find the angle of transmission θ_t.

$$\frac{\sin\theta_i}{\sin\theta_t} = \frac{c_1}{c_2} \tag{2.21}$$

The ratio of the transmitted energy to the reflected energy can be described by the reflection and transmission coefficient. The deduction of these two values requires a prerequisite of two boundary conditions applied: 1) pressure should be continuous along the boundary, $p_i + p_r = p_t$, and 2) the particle velocity component normal to the interface should be continuous, $|u_i|\cos\theta_i - |u_r|\cos\theta_r = |u_t|\cos\theta_t$. Then the pressure reflection coefficient R can be found as below

$$R = \frac{p_r}{p_i} = \frac{Z_2\cos\theta_i - Z_1\cos\theta_t}{Z_2\cos\theta_i + Z_1\cos\theta_t} \tag{2.22}$$

And the intensity reflection coefficient α_R becomes

$$\alpha_R = \frac{I_r}{I_i} = R^2 = \left(\frac{Z_2\cos\theta_i - Z_1\cos\theta_t}{Z_2\cos\theta_i + Z_1\cos\theta_t}\right)^2 \tag{2.23}$$

Snell's Law is being applied to further derive the intensity reflection coefficient as a function of angle of incidence θ_i, and

$$\alpha_R = \left(\frac{\frac{\rho_2}{\rho_1}\cos\theta_i - \sqrt{\left(\frac{c_1}{c_2}\right)^2 - \sin^2\theta_i}}{\frac{\rho_2}{\rho_1}\cos\theta_i + \sqrt{\left(\frac{c_1}{c_2}\right)^2 - \sin^2\theta_i}} \right)^2 \tag{2.24}$$

Since the intensity at the boundary should be conserved, the relationship between the intensity transmission and reflection coefficient α_T and α_R satisfies the following equation

$$\alpha_T + \alpha_R = 1 \tag{2.25}$$

2.6.2 Critical Angle

When the speed of sound in the original medium is smaller than the speed in the medium on the other side, i.e., $c_1 < c_2$, total reflection phenomenon occurs when the angle of incidence is greater than a certain angle. This angle is known as the critical angle, which leads to the angle of transmission to be 90°. Therefore, no acoustic energy will be transmitted into the other medium. By solving the equation $\alpha_R = 1$, the critical angle is found to be

$$\theta_{crit} = \sin^{-1}\left(\frac{c_1}{c_2}\right) \tag{2.26}$$

Any acoustic ray that enters the boundary at an angle greater than θ_{crit} is reflected back into the original medium. For instance, the reflection and transmission coefficient at the boundary of the water and the prostate phantom is plotted in Figure 2.6. The incident angle for total reflection at the boundary between the water and the phantom interface is 73°.

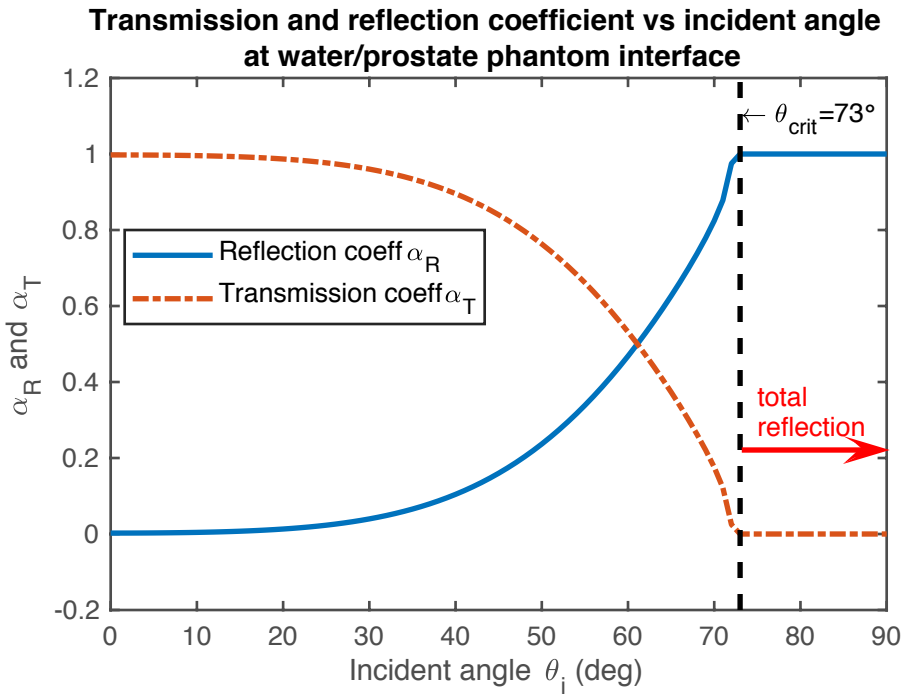

Figure 2.6 Transmission and reflection coefficient vs incident angle at the interface between water and prostate phantom

2.6.3 Phase Shift at the Material Discontinuity Interface

When the angle of incident is greater than the calculated critical angle, i.e., $\theta_i > \theta_{crit}$, the total reflection still occurs but the acoustic beam experiences a phase shift $\Delta\varphi$ at the boundary. This is due to the fact that the condition $\theta_i > \theta_{crit}$ causes an imaginary component when solving Equation (2.24), and the pressure reflection coefficient R in this case becomes

$$R = \frac{\frac{\rho_2}{\rho_1}\cos\theta_i - j\sqrt{\sin^2\theta_i - \left(\frac{c_1}{c_2}\right)^2}}{\frac{\rho_2}{\rho_1}\cos\theta_i + j\sqrt{\sin^2\theta_i - \left(\frac{c_1}{c_2}\right)^2}} \tag{2.27}$$

And the phase shift $\Delta\varphi$ is found to be [40]

$$\Delta\varphi = \arg(R) = -2\tan^{-1}\frac{\rho_1\sqrt{\sin^2\theta_i - \left(\frac{c_1}{c_2}\right)^2}}{\rho_2\cos\theta_i} \tag{2.28}$$

Equation (2.28) shows that the phase shift occurs at the material discontinuity interface is a function of the angle of incidence, the density and the speed of sound

of the media on both sides of the boundary. Figure 2.7 presents the phase shift $\Delta\varphi$ at the boundary between the water and the prostate with incident angle of the acoustic beam varying from 0° to 90°.

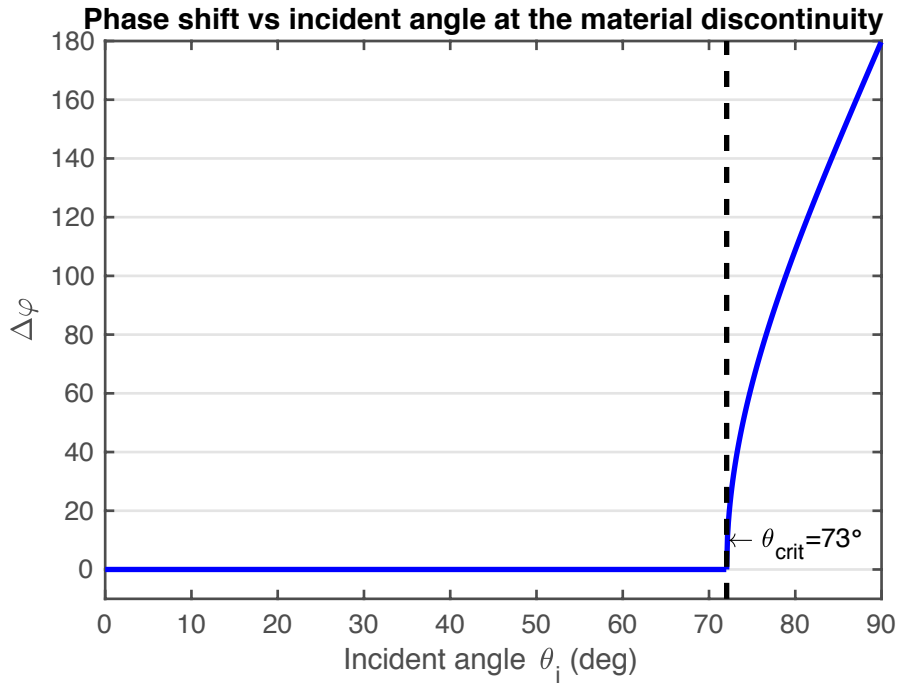

Figure 2.7 Phase shift $\Delta\varphi$ at the material discontinuity between water and prostate

2.6.4 Angle of Intromission

Another special scenario can occur at the boundary is called total transmission, which means no acoustic energy is reflected back into the original medium. This leaves the intensity reflection coefficient $\alpha_R = 0$. By solving Equation (2.24), one can find the angle of incidence in this case, also termed as angle of intromission, as following

$$\theta_{intro} = \cos^{-1}\sqrt{\frac{1-\left(\frac{c_1}{c_2}\right)^2}{1-\left(\frac{\rho_2}{\rho_1}\right)^2}} \tag{2.29}$$

2.7 Unique Features of DACI

Conventional ultrasound is a well-known medical imaging method. It is based on the amplitude measurement of the reflected and transmitted acoustic signal, and is not typically used to provide quantitative information. In this work, DACI presents a scanning configuration that measures both the phase and the amplitude information from the acoustic signal scattered from the virtual source in order to characterize the alterations in the tissue's mechanical properties.

2.7.1 Diffusive Scattering

In conventional ultrasound imaging research, the scattered signal is often filtered due to the large amount of noise it contributes to the detected signal. One of the few discussions regarding the importance of diffusive scattering is done by Shung [38]. Diffusive scattering is a common phenomenon occurring where the tissue structure is smaller than the wavelength of the signal, which is in the order of a millimeter. In our case, the scattered signal has the greatest potentiality that it can infer important information regarding tissue characterization.

2.7.2 Convergent Beam and Virtual Source

The geometry and the layout of the specimen and instrument plays a vital role in determining the feasibility of the new method. Unlike ultrasound transducer that are often equipped with loads of tiny piezoelectric elements to emit the phonons at the same time, only one single detector is used in this design. The key factor makes this possible is that we use a focusing mirror to bring the collimated beam from the source to a focus probe position within the specimen. The probe focus position acts as a virtual source that sufficient acoustic intensity is scattered *in situ*. This design sets DACI different from ultrasound due to the fact that the beam direction of the ultrasound transducer is divergent and multi-element.

2.7.3 Confocal Microscopy

Confocal microscopy is a technique extensively used in optic imaging to increase the spatial resolution of received signal by filtering out those out-of-focus

rays. Dr. Rodney Herring developed the confocal scanning holography microscope [41] and his group was able to apply this technology to measure the 3D refractive index [42], the 3D temperature and 3D composition [43]. DACI uses the similar concept for reference in order to enhance the resolution of the received signal. The point receiver is able to filter out the out-of-focus rays and avoids cross-talk. With all these features, DACI uses a non-invasive acoustic wave and employs a unique diffuse scattering design to entail the data collection of both phase and intensity information.

Chapter 3 Experimental Methodology

This chapter presents the current layout design of DACI and its three components. The concept of virtual source was introduced and the requirement of its location was specified. It describes how to build an ethernet-based USRP platform to realize the real-time extraction of phase shift between the received signal and the transmitted signal. Two phase shift detection methods are elaborated. The details of the USRP hardware implementation and software implementation are articulated as well.

3.1 Current Design of DACI

3.1.1 Geometry

The current design of DACI presented in Figure 3.1 is based on the earlier work by Atalick [44] and McCaugherty [45], and is modified to be more practical for clinical use. It features three components: the acoustic emitter, the focusing mirror and the point receiver, all immersed in the water aquarium. Due to the fairly large acoustic impedance mismatch between air and solid, water can function as a liquid couplant to ensure the transmission of the acoustic intensity. Additionally, in this project, it also works as a medium identical to the environment in the human body. The tilted focusing mirror with a parabolic surface brings the collimated acoustic beam output from the emitter into a focused probe position. The focused probe position needs to be located at the near surface of the prostate or within the bladder, which is filled with fluid. This provides an acoustic impedance matching environment for the acoustic rays to diffusively scatter into all directions at the focused probe position. Therefore, the focused probe position is considered as a virtual source. The point receiver, which sits around the perimeter of the prostate, needs to be rotated around the virtual source to capture the continuous acoustic signal passing through the specimen at each scanning position. The experimental setup following this scanning configuration is elaborated in Chapter 5.

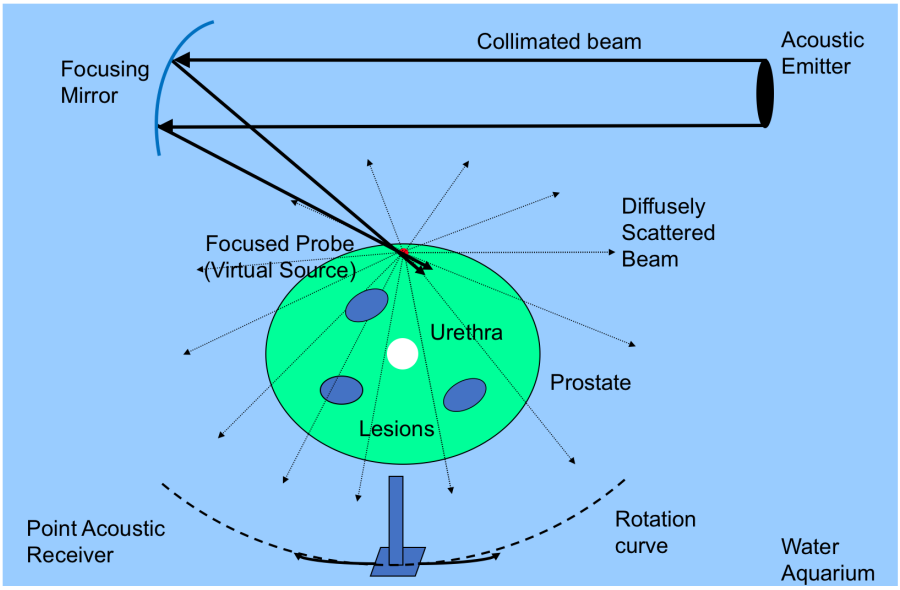

Figure 3.1 Current design layout of DACI

3.1.2 Emitter and Receiver

The emitter and the receiver used in the design are both immersion transducers. Piezo material, the main active component inside the transducer, converts the electric energy to its mechanical form. The model VP 5072PR from Valpey Fisher was chosen as the emitter. The selection principle of the emitter was elaborated in the earlier work [44]. The receiver used in the experiment is VP 1.5R from Valpey Fisher. The specifications of the emitter and the receiver are listed below in Table 3.1. The nominal frequency labeled by the manufacturer refers to the center frequency of the piezo material being used in the transducer. The DACI's experiments and simulations are performed using a continuous acoustic wave with the frequency 1.5 MHz.

Table 3.1 Specification of the emitter VP 5072PR and the receiver VP 1.5R

Parameter	Emitter	Detector
Nominal Frequency	2.25 MHz	1.5 MHz
Element Diameter	1.5 inch (38.1mm)	2.0 mm

Focus Type	Flat	Flat
Damping	500Ω	500Ω

There are two regions in the acoustic beam, near field and far field. Compared to a focused transducer, the flat focus type does not have a curved hourglass shape in the focal range. Its beam shape is determined by the nature of the wavefront propagation and remains relatively constant in the near field range. The near field distance of flat immersion transducer F, also known as the Fresnel zone, can be found in Equation (3.1) [46]. The speed of sound value, 1465 m/s, used for approximation was measured in the aquarium and the measurement procedure is explained in Section 6.1. The result shows that in the range of 37.13 cm from the surface of the emitter, the beam width of acoustic ray Ω only changes about 1.5°.

$$F = \frac{D^2}{4\lambda}\left[1 - \left(\frac{\lambda}{D}\right)^2\right] \approx 37.13\ cm \tag{3.1}$$

$$\sin\frac{\Omega}{2} = \frac{0.514c}{fD} \approx 0.013 \xrightarrow{yields} \Omega = 1.5° \tag{3.2}$$

where D is the diameter of the emitter. The wavelength $\lambda = 977\ \mu m$ is determined by the frequency value of 1.5 MHz.

The small corresponding beam divergence angle Ω found using Equation (3.2) [46] further explains why the output acoustic rays from the emitter are considered as collimated.

3.1.3 Attenuation Considerations

The dimensions of the water aquarium used in the lab are $90\ cm \times 45\ cm \times 35\ cm$. The total travel distance of the acoustic beam involved in the current scanning configuration includes three segments: from the emitter to the mirror, from the mirror surface to the virtual source and from the virtual source to the detector. Thus, the approximate total distance is 46 cm. Plugging the acoustic frequency 1.5 MHz used for the experiments into Equation (2.20), the attenuation coefficient in decibel scale α_{dB} is found to be 0.489 dB/m via Equation (2.19). This

leads to a decay in the acoustic intensity by 0.22 dB, which corresponds to a decrease in the intensity of 5%. Therefore, the acoustic signal output from the emitter is sufficient to be detected by the point receiver.

3.1.4 Focusing Mirror

The other component is the focusing mirror with a parabolic surface, which brings the collimated acoustic rays from the emitter into a focused probe position. This mirror was simulated and designed in the earlier work [44].

3.1.5 Phantom

The sample for the experimental measurement is a tissue equivalent ultrasound prostate phantom from Computerized Imaging Reference Systems (CIRS), Inc. This company owns a patent on the ultrasonic calibration materials that feature similar ultrasonic characteristic properties of human soft tissues. It is made of a solid elastic material [47] which is able to sustain the physical properties during temperature change. Nowadays, there are several solutions in the field of tissue mimicking material research to suit different applications. The solid elastic material of model 053L uses a water based gel matrix, mixing with other liquid and solid particles to finely tune the properties of material. For instance, the speed of sound range of this material can be adjusted between 1420 m/s and 1650 m/s. This feature is crucial for DACI since this research focuses on the measurement of the speed of sound value of the sample. When imaged with diagnostic tools, it displays an identical texture pattern and scattering properties to the prostate gland.

This model is originally placed in an acrylic container (see Figure 3.2(a)), with the urethra of 7 mm diameter going through its center. The prostate volume is about 55 cc, and its dimensions are given as 5 cm×4.5 cm×4 cm [48], similar to the walnut size of a healthy prostate in a man's body. 053L is the model with three lesions placed inside the prostate. Figure 3.2(b) shows the ultrasound image of the

phantom model 053L used in DACI, the lesions appear hypoechoic and only two of them can be found in the image.

Figure 3.2 CIRS phantom model 053L: (a) phantom in the container, (b) The conventional ultrasound image of the phantom [48].

3.2 Phase Detection Method

As indicated in the previous chapter, phase is a parameter that contains information regarding the change in speed of sound. In order to enable the transmission and reception of signals and measure the phase difference between them, a new experimental system is established based upon a USRP platform to enable the synchronization of the data flow in both directions and to improve the measurement accuracy with high sampling frequency.

There are several different ways to measure the phase shift between two signals. Conventionally, a reference acoustic beam is taken across the background while the object acoustic beam is manipulated through the specimen. The phase difference can be measured spatially by comparing the difference of angles of arrival between the reference beam and the object beam. However, the system to extract the phase information presented in this thesis does not require a 'real' reference signal. The following introduction of the SDR technology and the USRP platform provides a basic understanding of how DACI measures the phase and amplitude information in the experiment.

3.3 SDR and USRP

3.3.1 Introduction to SDR Technology

Acoustics is considered to be the ideal and primary modality to enable underwater digital communication system design. Another task in this project is to develop a reliable signal generation and data acquisition platform that can work in the acoustic frequency range of $1\sim2\ MHz$. It is the flexibility of SDR technology that provides the possibility to build the data acquisition device for DACI with a USRP MATLAB support package.

Typical components involved in radio communication systems, such as mixers, filters and modulators, are usually defined in the hardware level. The emergence of the SDR system provides an alternative method to configure these components by software modification. One of the most important characteristics of SDR is its multifunctionality which can be realized by employing field programmable gate array (FPGA)-based implementation [49]. Multiple types of radio functions such as different modulation schemes can be supported on the same platform at different time.

3.3.2 USRP Hardware Architecture

USRP is a well-known powerful SDR platform designed for the radio frequency (RF) applications from DC ($0\ Hz$) to $6\ GHz$, first developed by the Ettus Research LLC™. The USRP platform design in this project is done by the USRP® support package from MATLAB. The Ettus Research™ USRP™ N210 is used for enabling the design and implementation of the communication system for the DACI's experiment. FPGA is a key component inside the hardware architecture. It is a very compact powerful gate array with low voltage that enables multi-functions, such as parallel processing. It is programmable allowing to put in some coding and digital signal processing (DSP) function. It is a kind of technology advancing rapidly due to its hardware engineering control ability. It can process data at high intensity memory consumption and realizes multiple logical controls [50]. The FPGA

installed in the USRP N210 is Spartan® 3A-DSP 3400 [51], it includes two digital down converters (DDC) chains on the receiver path and one digital up converter (DUC) on the transmitter path [52]. The dual 14-bit analog-to-digital converters (ADCs) on the receiver path and 16-bit dual digital-to-analog converter (DACs) on the transmitter path, also included on the FPGA board, allow the data to be sampled up to 100 MS/s in both directions and translate the signal between analog intermediate frequency (IF) signal and digital IF signal.

In order to enable the successful signal communication system, appropriate daughterboards are vital to be installed in the USRP device so that the signal can be easily tuned. The front end on the daughterboards works as an interface to enable the analog signal flow into or out from the USRP. In this experiment, the LFTX and LFRX daughterboards from Ettus Research LLC™ were chosen to suit DACI's high frequency range communication application and be used on the transmission and reception path respectively. The main purpose of LFTX/RX daughterboards is to amplify the input signal, and there is no local oscillator (LO) involved.

3.3.3 I/Q Signal Notation

The in-phase and quadrature (I/Q) signal notation or representation is a vital concept used in the SDR technology. There are two ways to represent a complex number in Cartesian coordinates and polar coordinates. In Cartesian coordinates, the real axis component and the imaginary axis component are rotated apart by 90 degrees. In polar coordinates, the complex number is denoted by the amplitude and the angle. Euler's formula describes a complex exponential function using the trigonometric functions.

$$e^{ix} = \cos x + i \sin x \tag{3.3}$$

where the real part $\cos x$ refers to the in-phase component, and the imaginary component $\sin x$ refers to the quadrature component. And, they are 90 degrees out

of phase. Figure 3.3 shows an example of a complex exponential function and its decomposed real and imaginary components.

A complex signal $s(t)$ can follow the manner of Euler's formula and be represented by its in-phase component $s_I(t)$ and quadrature components $s_Q(t)$ using the following equations (3.4) and (3.5), where the complex data can be understood as being translated from polar coordinate to a Cartesian coordinate system [53]. And $\phi(t)$ refers to the phase between the I/Q components.

$$s_I(t) = s(t)\cos\phi(t) \tag{3.4}$$

$$s_Q(t) = s(t)\sin\phi(t) \tag{3.5}$$

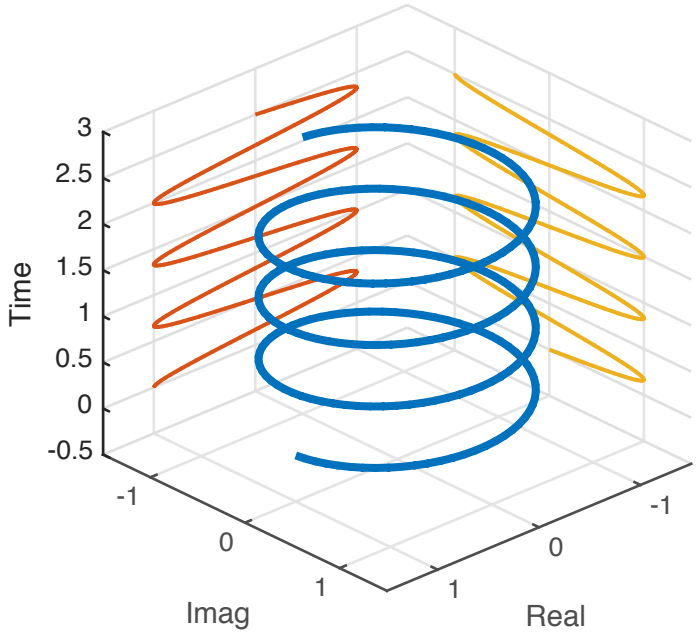

Figure 3.3 Exponential signal and its real and imaginary components

The I/Q signal notation in Cartesian coordinate system is shown in Figure 3.4:

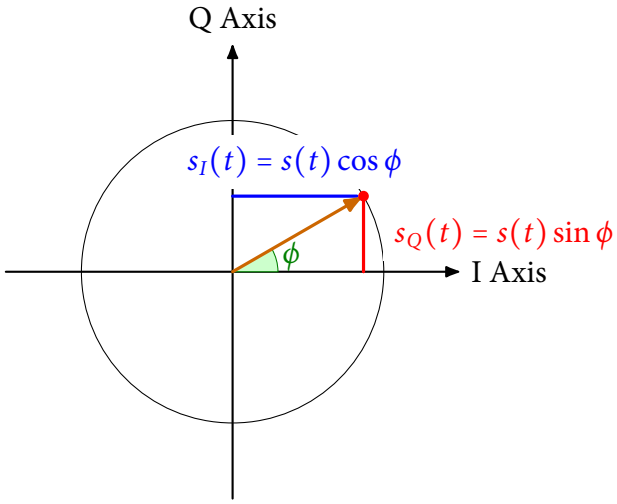

Figure 3.4 I/Q signal representation

In a RF communication system, the baseband frequency is usually not in the same band as the channel assigned. The process of changing the baseband frequency to fit in the channel bandwidth is known as modulation. And this is realized by using a mixer to multiply the input signal with the carrier frequency f_c, generated by an electric component called oscillator, to convert the signal into desired frequency range. The oscillator used in the USRP N210 is called numerically control oscillator (NCO) because it can generate two carrier signals with the same frequency but has a 90 degrees phase shift between each other, i.e., $\cos 2\pi f_c t$ and $\sin 2\pi f_c t$. They are actually the in phase and quadrature components of a complex exponential signal $e^{j2\pi f_c t}$. The reason that I/Q representation is commonly used in communication system is that it is more suitable for hardware implementation in USRP platform [53]. This representation enables the control of amplitude, frequency and the phase of I and Q input components of the carrier wave instead of directly varying the phase of an RF carrier wave. Most importantly, it helps to preserve both the magnitude and the phase of the signal [54]. Even though the signal transmission in the DACI does not have such strict channel bandwidth requirement, it is still able to benefit from the feature of the SDR technology that the phase can be interpreted by the I/Q signal representation.

3.3.4 Data Flow on the Receiver and the Transmitter Paths

A typical USRP device includes the RF front end, mixers, filters, oscillators and amplifiers to translate a signal between the RF band and the baseband [55]. The diagram shown in Figure 3.5 illustrates how data flows from the RF front ends on the USRP into the host computer:

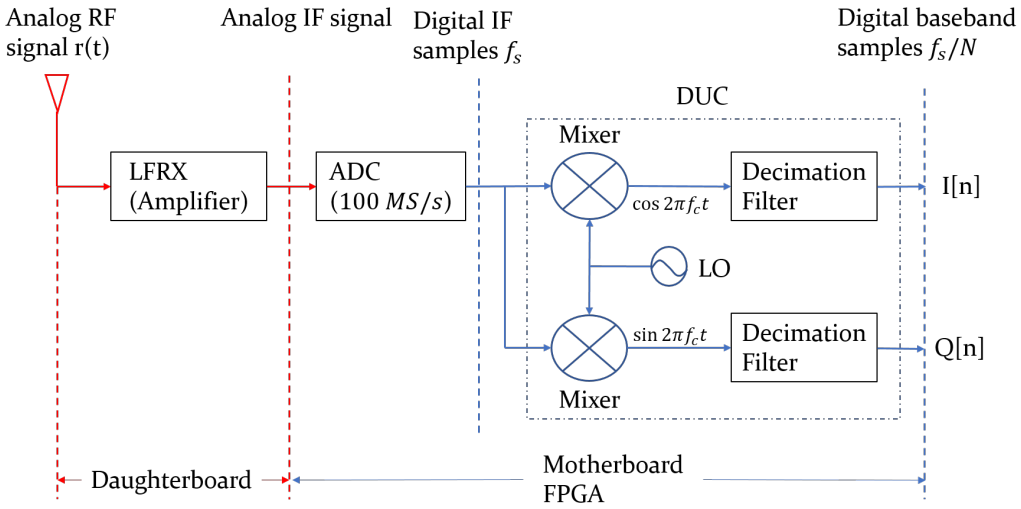

Figure 3.5 USRP N210 + LFRX receiver block diagram

On the receiver path, the received analog signal $r(t)$ is sent to the USRP through the RF front end on the daughterboard LFRX from the detector. The high-speed differential amplifier on the LFRX streams the signal into the single ADC in the USRP N210 [56]. Then the ADC samples the analog signal at the rate $f_s = 100\ MS/s$ (Mega Sample per second) and converts it into the digitized samples and clocks them into the FPGA. Then the digital samples enter the DDC, the most key component of the receiver path on the FPGA. Firstly, two mixers are used with an oscillator that can generate two carrier waves with a 90° phase shift in order to decompose the signal into its in-phase and quadrature components and shift the frequency to the desired baseband. Then the decimation filter, the second stage in DDC, reduces the sampling frequency f_s by a factor of N to fit the processing rate of Gigabyte Ethernet interface with the host computer. Eventually the samples are further filtered to remove unwanted frequency components and sent back to the host PC.

Since only one antenna port is enabled on the LFRX daughterboard, the front end receives real signal. Suppose we receive an analog signal $s(t) = \cos(2\pi f_{RF} t + \phi(t))$, where $\phi(t)$ is the initial phase at time instant time t. After amplified by the LFRX daughterboard and digitized by the single ADC, the digital signal is fed into the two out of phase mixers in DDC to extract the carrier frequency f_c. The process of modulating the n_{th} sample fed into the DDC can be described as following:

$$\begin{aligned}
&\cos(2\pi f_{RF} n + \phi[n])\, e^{-j2\pi f_c n} \\
&= \cos[2\pi f_{RF} n + \phi[n]](\cos 2\pi f_c n - j \sin 2\pi f_c n) \\
&= \frac{1}{2}\{\cos[2\pi(f_{RF} - f_c)n + \phi[n]] + \cos[2\pi(f_{RF} + f_c)n + \phi[n]]\} \\
&+ \frac{j}{2}\{\sin[2\pi(f_{RF} - f_c)n + \phi[n]] + \sin[2\pi(f_{RF} + f_c)n + \phi[n]]\}
\end{aligned} \tag{3.6}$$

The resulted frequency component $f_{RF} + f_c$ will be removed by the low pass filter later in the DDC. And the difference between the two signals $f_{RF} - f_c$ gives the desired baseband frequency f_b. This step leads to the result to become:

$$\begin{aligned}
&\cos(2\pi f_{RF} n + \phi[n])\, e^{-j2\pi f_c n} \\
&= \cos[2\pi f_{RF} n + \phi[n]](\cos 2\pi f_c n - j \sin 2\pi f_c n) \\
&= \frac{1}{2}\{\cos[2\pi(f_{RF} - f_c)n + \phi[n]]\} + \frac{j}{2}\{\sin[2\pi(f_{RF} - f_c)n + \phi[n]]\} \\
&= \frac{1}{2}\cos(2\pi f_b n + \phi[n]) + \frac{j}{2}\sin(2\pi f_b n + \phi[n])
\end{aligned} \tag{3.7}$$

The above equation articulates how the input signal into the DDC is processed into two paths, in-phase and quadrature, respectively. This explains how the phase information $\phi[n]$ is preserved during the process of data transmission in the USRP. At the end of DDC, the output is in the quadrature form and streamed into PC as a series of complex digital signal.

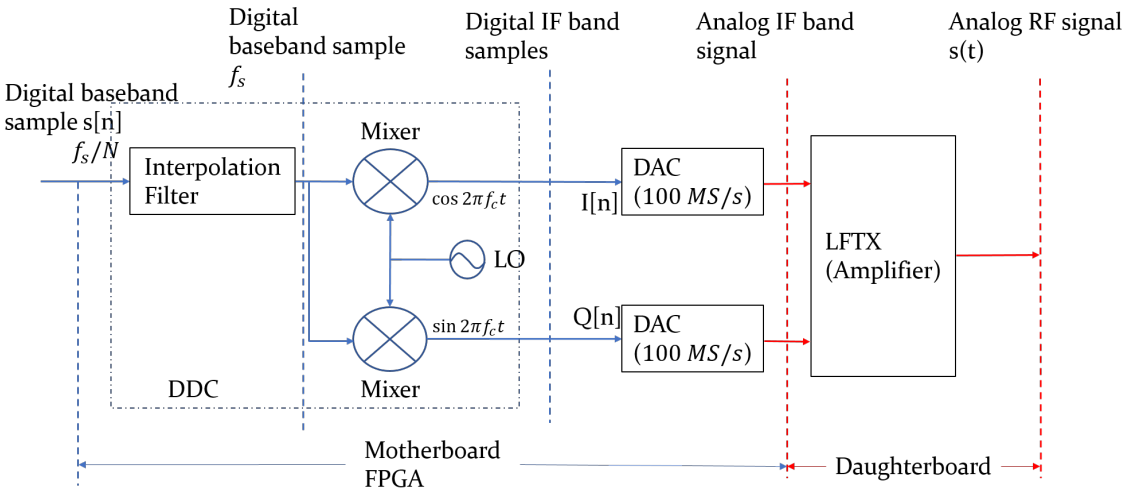

Figure 3.6 USRP N210 + LFTX transmitter block diagram

On the transmission path, the PC host sends the digital baseband I/Q sample $s[n]$ over to the USRP device through the Gigabyte Ethernet cable. The I/Q pair will be fed into the DUC to be up-converted to the IF band via two stages: 1. The interpolation filter with a factor N to increase the baseband sampling frequency f_s/N to f_s, the same as the master clock rate 100 MS/s. And then the I/Q signal streams into the two mixers with carrier frequency generated by the NCO. And DAC converts the IF band digital samples to the analog IF signal. Then the analog IF signal is sent to the LFTX daughterboard to be amplified. Finally, the signal is sent from the RF front end on the LFTX into the acoustic emitter. The procedures described above can be found in the block diagram presented in Figure 3.6.

3.3.5 Sample Rate

Before getting into choosing the proper sampling frequency in the experiment, it is necessary to investigate the bandwidth compatible with all the stages in the USRP. When communicating with the USRP N210, the Gigabyte Ethernet cable from the host PC can stream up to 25 MS/s when transmitting 16-bit I/Q samples. Both the LFTX and the LFRX daughterboard have two antennae ports A and B. They can be used individually as A or B in the real-mode, or used in combination as AB or BA in the complex form [57]. In the DACI system, the front ends on both

sides are operated in real mode, hence the daughterboard analog bandwidth is 30 MHz. As for the FPGA motherboard, the processing bandwidth depends upon the sample rate f_s of ADC and DAC, which is 100 MS/s. Considering the host bandwidth, the daughterboard analog bandwidth and the FPGA processing bandwidth together, the lowest value among them limits the useful bandwidth of the USRP N210 system with LFTX/LFRX to about 20 MHz [55].

One of the major benefits using the USRP platform is that it can provide very high sampling frequency. The conversion rate between the analog signal and the digital samples is 100 MS/s, and the signal processing in the IF band is also sampled at $f_s = 100\ MS/s$. When it comes to the baseband signal sampling, the decimation filter and interpolation filter in the DDC and the DUC both have a lower sampling frequency, f_s/N. This is because the lower but still sufficient sampling frequency can speed up the processing speed of the signal in the system. The choice of decimation factor and interpolation factor has certain guidelines as well. First of all, the factor should at least be an integer. In the case it is greater than 128, it should be an integer of 2, and an integer of 4 if greater than 256 [49].

The Nyquist-Shannon sampling theorem states that the minimum sampling frequency to reconstruct a signal in the digital domain should be no less than double the baseband. Otherwise, it can cause the sampled signal to be distorted, also known as aliasing. In order for a faithful reconstruction of the signal that is confined to a maximum frequency f_m, the signal should be sampled at a sampling frequency f_s that is greater than or equal to twice the maximum frequency of the signal, i.e., $f_s \geq 2f_m$. In the USRP systems, the baseband sampling frequency f_s/N should be equal to or greater than twice the baseband frequency f_b.

3.3.6 Frame-based Sampling vs Sample-based Sampling

Conventionally, the digital baseband samples are streamed from the host PC as a series of digital samples at the given sampling rate. In between each sample, there is a time interval called interrupt service routine (ISR) that is used to fetch

data from the hardware. The MATLAB USRP support package provides another way commonly used in the real-time communication system. This method is called frame based sampling [58]. In essence, multiple samples can be buffered into a block and then sent to the USRP device at once. In this method, ISR only occurs in between each frame so that the overall processing time can be reduced to increase the communication efficiency. For instance, the overall data streaming time duration assigned by the host computer is T_{sto}, the interpolation factor and the decimation factor is N and the frame length is FL. The interval between each sample is the inverse of the baseband sampling frequency N/f_s. It means that the time to sample one frame is $FL \times \frac{N}{f_s}$, and the number of frames sent from and received into the host computer can be found by taking the ceiling of $\left\lceil \frac{T_{sto} \times f_s}{FL \times N} \right\rceil$.

The default frame size in the transmitter and receiver block in the USRP support package is 362. This value is set to optimize the underlying Ethernet payloads for a standard 1500-byte maximum transmission unit (MTU).

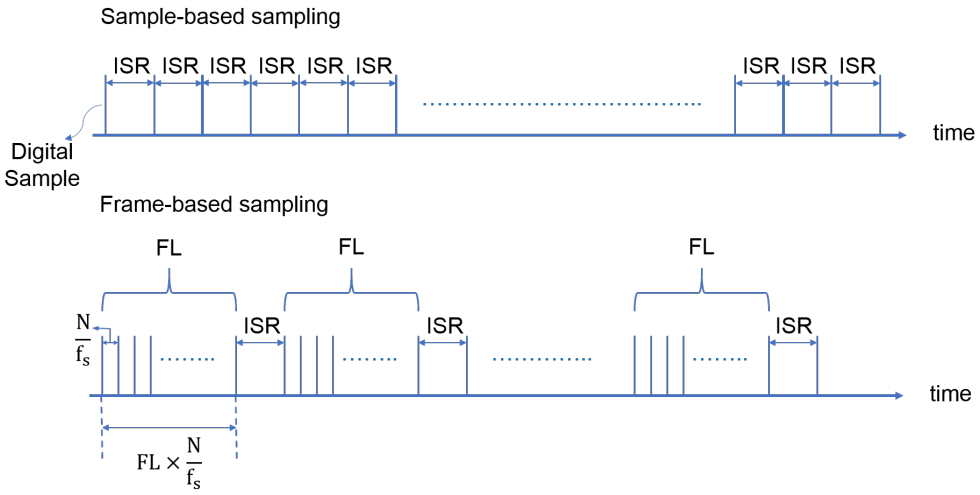

Figure 3.7 Sample-based sampling and frame-based sampling

3.3.7 Barker Code for Frame Synchronization

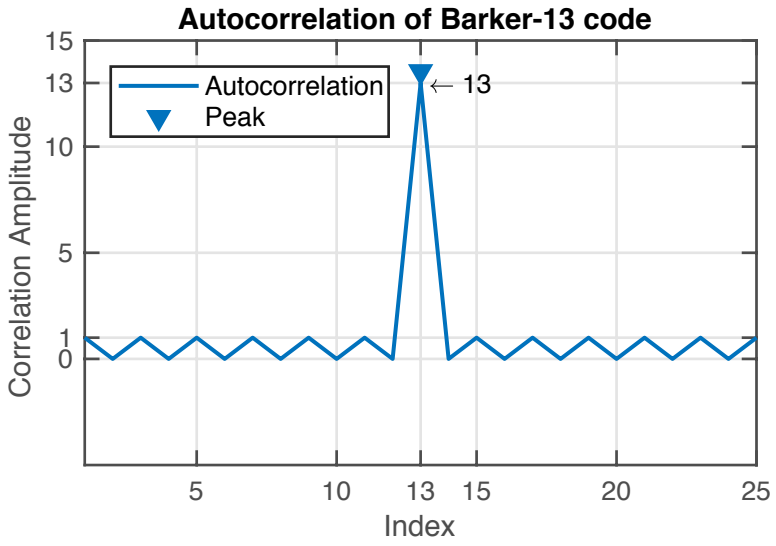

Figure 3.8 Auto correlation properties of a 13-bit Barker code

Barker code is a very common pseudo-noise (PN) sequence used for frame synchronization between the transmission and reception path [49]. Due to the unique sequence of value ± 1, the barker code exhibits strong auto correlation properties shown in Figure 3.8. In the example of 13-bit Barker code sequence, the magnitude of the correlation sidelobes is only $1/13$ of the peak of the correlation. This property makes the Barker code an ideal choice to be added to the beginning of a frame of samples. Upon receiving, the start of reception signal can be differentiated by performing correlation computation.

3.3.8 Phase Unwrapping

The detected phase is related to the path length of the acoustic signal within the prostate phantom. If the phase exceeds the range $[-\pi, \pi]$, the inverse trigonometry function will give a wrapped phase variation with phase jumps. Therefore, the phase unwrapping technique is employed to reconstruct the continuous phase image. An example of the unwrapping phase process is shown in Figure 3.9. The original phase shown in the left figure varies between $-5.026\,rad$ to $5.026\,rad$, and the curve presents a parabola shape. The wrapped phase plot shown in the middle confined the phase range in the $[-\pi, \pi]$ and there are several sharp turning points. With the phase unwrapping technique, the reconstructed phase shown on

the right side varies from $-1.257\ rad$ to $-11.31\ rad$ and has a similar parabola shape to the original phase. Even though the start and the end point are different from the original phase plot, the variation range in the reconstructed phase image equals to the original one, which is about $10.05\ rad$.

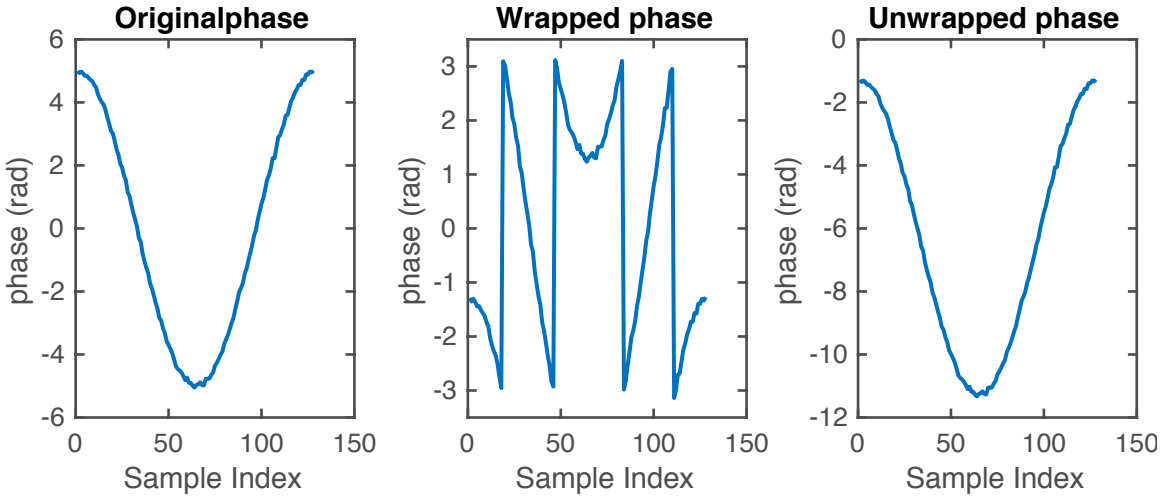

Figure 3.9 Example of applying the phase unwrapping technique

The unwrapped phase technique is useful when interpreting the total phase variation φ_{tot} due to the fact it contains information about the travel distance and the propagation speed of the acoustic beam.

3.4 Fourier Transform based Method

3.4.1 Frequency Domain and Time Domain

Most of the time, people are naturally more used to the time domain representation of a signal because the characteristics are more intuitional. However, the signal in the real word can become very complicated so that its presentation in the time domain does not convey direct valuable information. Frequency, an important characteristic of a wave or a signal, describes the change rate of the instantaneous phase. Fourier transform is the method to transform the time domain signal into the frequency domain and provides another way to investigate the signal. For instance, a square wave is in fact a linear combination of several sine waves at various frequencies and amplitude.

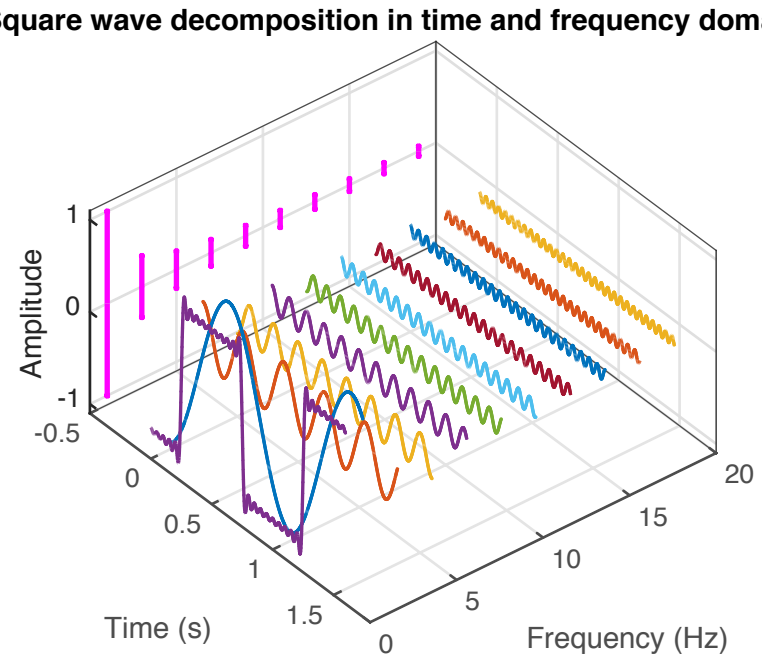

Figure 3.10 Decomposition of square wave in time and frequency domains

Figure 3.10 illustrate how the sum of ten sine waves at different frequencies and amplitudes forms a resultant periodic signal similar to a square wave. Each frequency component is displayed in the stem graph in the amplitude-frequency plane. The amplitude of each component determines its weight contribution towards the square wave. This is just a simple example that explains how the frequency domain can provide valuable information for signal processing.

The Fourier transform of the signal x(t) is denoted by $X(\omega)$ as below [59]:

$$X(\omega) = \mathcal{F}\{x(t)\} = \int_{t=-\infty}^{\infty} x(t)e^{-i\omega t}dt \tag{3.8}$$

And the inverse Fourier transform gives the original signal x(t) as

$$x(t) = \mathcal{F}^{-1}\{X(\omega)\} = \frac{1}{2\pi}\int_{\omega=-\infty}^{\infty} \mathcal{F}(\omega)e^{i\omega t}d\omega \tag{3.9}$$

where $\mathcal{F}\{\cdot\}$ refers to the operator of the Fourier transform, and $\mathcal{F}^{-1}\{\cdot\}$ is the operator of the inverse Fourier transform (IFT). The ω on the exponential refers to the angular frequency.

The discrete Fourier transform (DFT) of a digital signal x[n] is given as

$$X[k] = \sum_{n=0}^{N-1} x[n]\, e^{-\frac{i2\pi k}{N}n}, \tag{3.10}$$

where n refers to the sample index and N is the length of the digital signal. Similar to the inverse Fourier transform, the inverse discrete Fourier transform (IDFT) is given by

$$x[n] = \frac{1}{N}\sum_{n=0}^{N-1} X[k]\, e^{\frac{i2\pi k}{N}n}. \tag{3.11}$$

One of the important properties of Fourier transform is the shift theorem described by equation (3.12). The shift in the time domain leads to a complex exponential term added to the original Fourier transform. The magnitude of this term is equal to one. As a matter of fact, this delay in the time domain is essentially a phase shift in the frequency domain without changing the amplitude of the spectrum. The phase delay, in the time domain, can be found as the ratio of time lag to the period of the signal multiplied by 2π. As indicated in Equation (3.12), the delay in temporal sample index M causes a phase shift $\Delta\varphi = -\frac{2\pi k}{N}M$.

$$\sum_{n=0}^{N-1} x[n-M]e^{-\frac{i2\pi k}{N}(n-M)} = X[k]e^{-\frac{i2\pi k}{N}M} \tag{3.12}$$

The Fast Fourier transform (FFT) is a fast and optimized algorithm to implement DFT. It significantly reduces the complexity of the DFT from $O(N^2)$ to $O(NlogN)$. According to the shift theorem, the FFT result outputs the maximum value at the dominant frequency index and the phase information can be found by using the exact same index. This is how the FFT can work as a valid method to interpret the phase shift in the received signal.

3.4.2 Spectral Leakage and Windowing

When performing a FFT, the length of the sample is an integer value of the power of 2, which may not be the integer number of periods. This has the possibility of giving rise to a truncated waveform instead of reconstructing the

original signal. Consequently, the frequency spectrum is smeared at discontinuities. The spectrum energy may leak into another frequency, known as spectral leakage.

In order to avoid this phenomenon of aliasing, a technique called windowing can be applied. The main purpose of windowing is to lower the amplitude where the discontinuities occurs so the signal is smooth at the transition region. In most cases, the Hanning window is a good choice since it has a sinusoidal shape with a wide peak and diminishes to zero at the window edges [60]. Hence, it helps to reduce the noise among received signal in DACI's experiment.

Chapter 4 Simulations

This chapter presents the simulation models created using ZEMAX and COMSOL. Both the amplitude and the phase distribution were investigated, and the results are able to demonstrate the principle behind DACI. In COMSOL simulation models, the model representing the diseased prostate phantom was compared with the model with healthy tissues and the model without urethra. This comparison further proves the scattered intensity from the virtual source can deliver valuable information regarding the alterations in mechanical properties in the specimens.

4.1 ZEMAX Simulation

4.1.1 Introduction of ZEMAX

ZEMAX® OpticStudio is an exclusive optical design software that has industry leading power to design and analyze optical imaging and illumination systems based on complex physics. Even though it is not specifically designed to simulate acoustic waves, the similarity in wave theory still can promise the rationality of model design as long as the relative parameters are assigned to proper values. ZEMAX has been proven to be able to simulate the design of acoustic imaging system with appropriate parameters [43]. Its ray tracing feature enabled us to investigate the acoustic behaviour at the focus probe position and at the boundary of material discontinuity. This feature also helped to demonstrate the validity of the concept that virtual source has the sufficient acoustic intensity to carry the phase information.

4.1.2 Parameters Setup and Design Layout

The simulation model was created in the Non-Sequential mode in ZEMAX. In this mode, an acoustic ray can travel through the same object several times and multiple objects in random order. More importantly, the detector ray-tracing

feature can produce the spatial intensity and the phase image using incoherent or coherent beams [61].

The system properties applied to set the water background includes the frequency f = 1.5 MHz and c = 1465 m/s (measured speed of sound in the aquarium). This sets the acoustic wavelength in the environment to be $\lambda = 976.67\ \mu m$.

Following the proposed DACI design, the model consists of an acoustic emitter, a focusing mirror, a phantom with three lesions and a point receiver. In the ZEMAX simulation, appropriate object types are used to mimic the purpose of each component. In order to capture all the needed data at once, a 2D flat surface detector is used to replace the effect of moving the point detector to complete the simulation. The geometric dimensions of each component were assigned by using absolute positioning in the Cartesian coordinate system or by the relative position to the reference object.

The material discontinuities setup was realized by defining the wavelength, refractive index and transmission index in each medium [62]. This step resembles the process of setting the mechanical properties of different media. The acoustic behavior at these material discontinuity boundaries was simulated by enabling the option of the surface scattering function in the software. This function has fairly strong flexibility to characterize the scattering method and even the desired object if a certain scattering analysis is required. In general, more acoustic rays are recommended to produce a more accurate result [63]. The simulation layout is presented in Figure 4.1 below. With the filter correctly set up, the detector and the layout were chosen to display the data only from the rays that have interacted with the phantom [64].

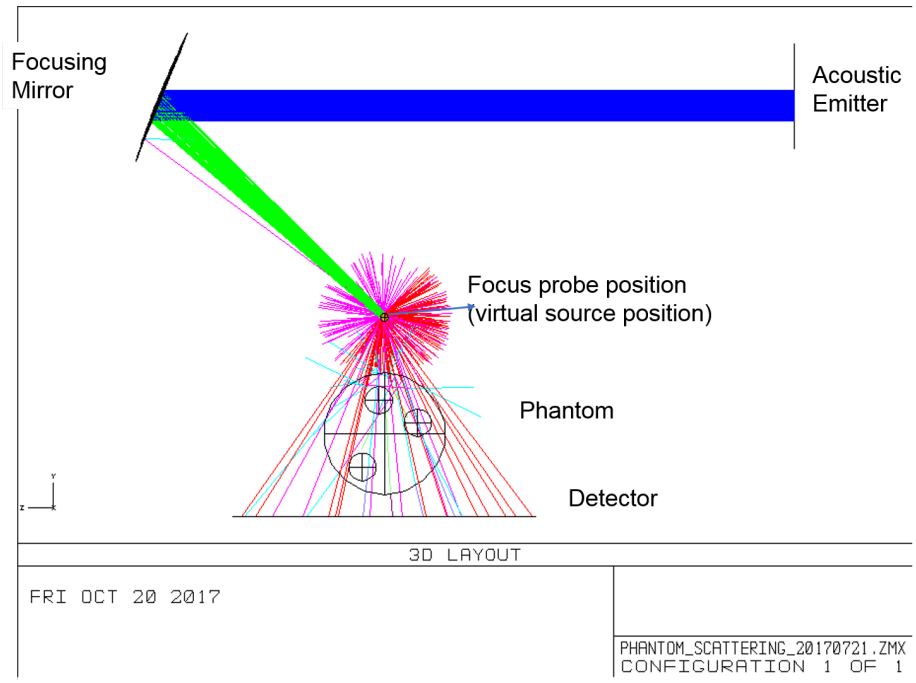

Figure 4.1 Layout of DACI design in ZEMAX simulation

4.1.3 Intensity and Phase Obtained from ZEMAX Simulation

The detector pixel size is set as 512×512 to increase the resolution of the output images to avoid aliasing.

1. Intensity:

The source power set in the simulation model is $1\,Watt$. From the detected intensity distribution of the design, the intensity level of the acoustic rays around the outer edge of the object shows the highest value. A large portion of the analysis rays are reflected and do not make it to hit the detector. This is due to the incident angle of the beam at the boundary and the material discontinuities at the boundary between the water background and the phantom. This leads to the lower intensity level within the phantom region (see Figure 4.2). But still, the outline of the prostate phantom can be easily distinguished, shown as the contour of the large circle. The mismatch between the healthy phantom and three spherical lesions inside cause the directional change of the rays that interacts with the lesions. Consequently, the distorted shape of the sphere appears as a more

shadowed region in the distribution image. The further the sphere is located away from the center position, the more the corresponding shape of the lesion is distorted.

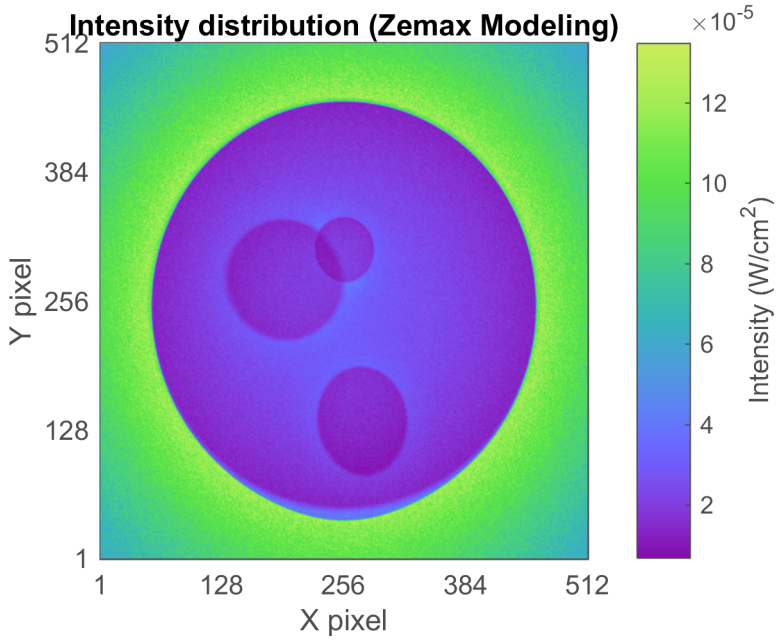

Figure 4.2 Intensity distribution of ZEMAX simulation model

2. Phase:

The whole 2D wrapped phase distribution shown in Figure 4.3 discloses similar promising results as well. And, a zoomed version of the phase image is shown in Figure 4.4. It presents the abrupt phase shifts at the location where the lesions exist. The phase periodically varies between $\pm\pi$ in a circular pattern. With the presence of spherical lesions, the original phases are shifted along the directions of the lesions.

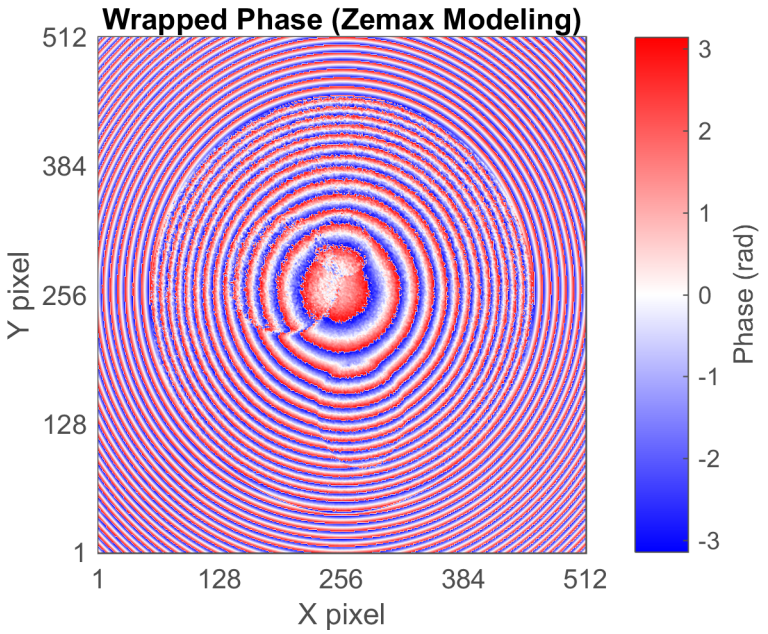

Figure 4.3 Wrapped phase distribution of ZEMAX simulation model

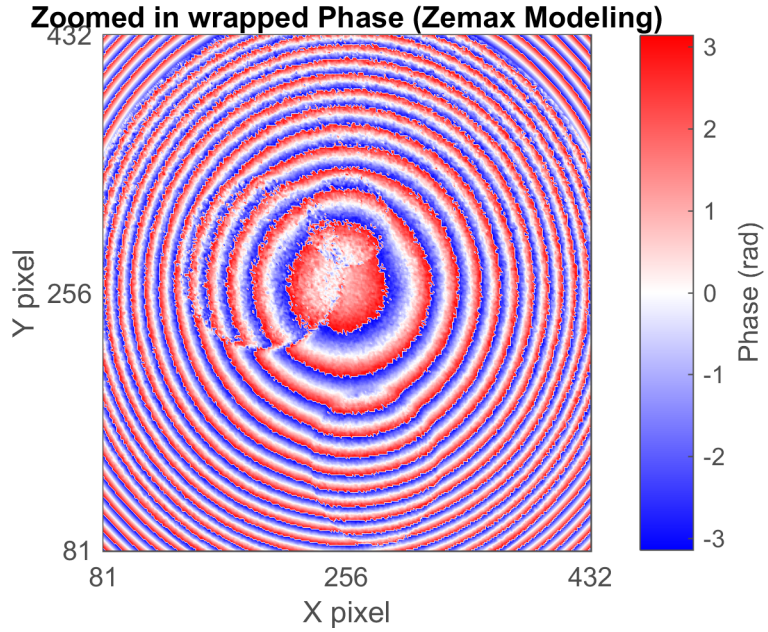

Figure 4.4 Wrapped phase distribution of ZEMAX simulation model (Zoomed in)

In order to better understand the phase distribution image, a row of data points can be taken from where $Y\ pixel = 300$ to produce a 1-D unwrapped phase plot to see where the phase jumps occur. From Figure 4.5, it can be found that the unwrapped phase produces a parabolic shape curve and varies with the spatial

position. This is due to the fact that beam hits the edge of the detector travels the longest distance, whereas the beam hits the center of the detector travels the shortest distance. The relationship between the total phase variation and the beam travel distance is given in Equation (2.15). As shown in the plot, the phase experiences a relatively large shift at the proximity around $X\ pixel = 190$, which are zoomed in so that smaller oscillations in the phase shift can be detected. Instead of following a perfect parabolic shape, the unwrapped phase curve is found to experience a sudden phase increase by 4.67 radian around the location $X\ pixel = 154$ and another sharp decrease by 6.4 radian around the location $X\ pixel = 231$. A small phase shift around 1.1 $radian$ occurred at the boundary between the water background and the prostate can also be detected at two symmetrical locations $X\ pixel = 61$ and $X\ pixel = 452$.

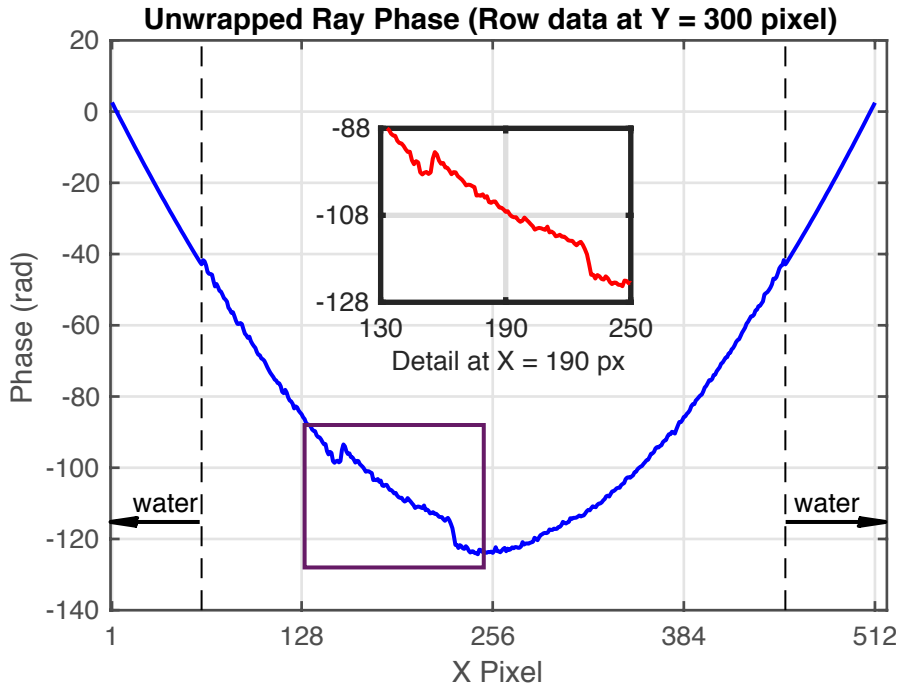

Figure 4.5 1-D unwrapped phase along $Y = 300\ pixel$ (ZEMAX)

The speed of sound variation along $Y\ pixel = 300$ was estimated using the relationship between the total phase variation and the speed of sound indicated in Equation (2.15), and the calculated result is presented in Figure 4.6. The abrupt increase in the speed of sound can be found around the location $X\ pixel = 61$ and

$X\ pixel\ =\ 452$, which corresponds to the location of the boundary between the water and the prostate. A sudden shift in the speed of sound can also be seen in the area from $X\ pixel = 154$ to $X\ pixel = 231$, where phase shifts occur at the interface between the healthy tissues and the lesions. As presented, the estimated speed of sound varies between 1450 m/s to 1670 m/s, which is in the range of speed of sound in the water and the prostatic tissues. A proper reconstruction technique is needed to recovery a more accurate speed of sound variation from the phase image.

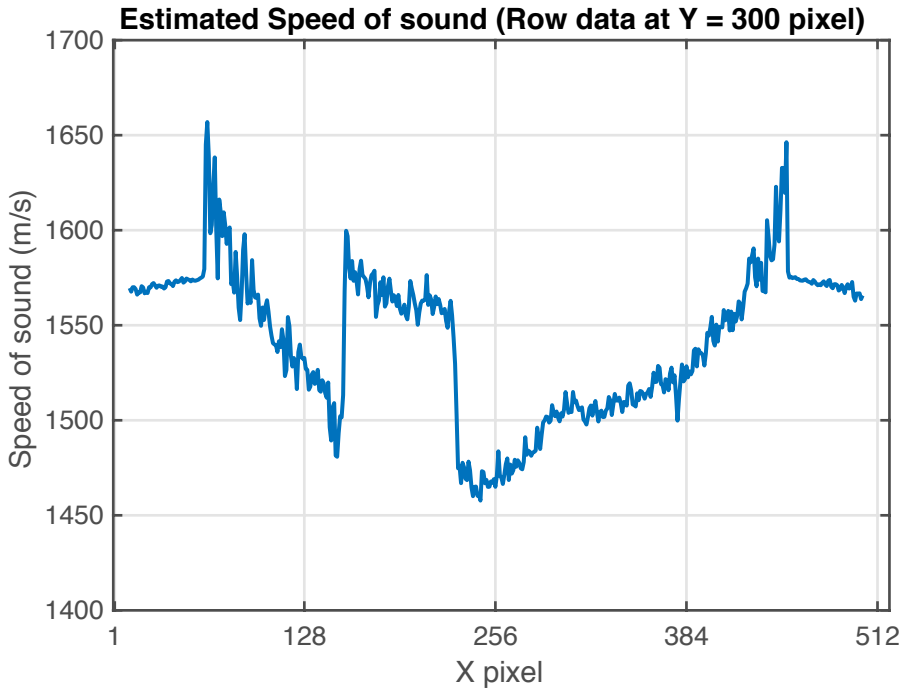

Figure 4.6 Estimated speed of sound along $Y\ =\ 300\ pixel$ (ZEMAX)

4.2 COMSOL Simulation

4.2.1 Introduction of COMSOL Multiphysics® and Acoustic Module Interface

COMSOL Multiphysics® is a powerful platform for inter-discipline physics-based simulations based on advanced numerical analysis methods [65]. It provides an interactive environment for finite element analysis modeling in various applications. The Acoustic Module is one of the add-ons designed to realize the simulation of system design using acoustic waves in the area such as noise

cancellation, microphones and sonar devices [66]. Users own high level control over the object geometries, mesh size, material properties and many more detailed settings regarding the model design.

With the interest in studying how the acoustic wave interacts with the media of different mechanical properties, the acoustic phenomenon such as scattering, transmission and reflection are tasked to be investigated. The Ray Acoustics from Geometrical Acoustics, one of the interfaces included in the Acoustic Module, is a great tool studying the trajectory, phase and intensity of acoustic waves [67]. It is implemented under the condition that the acoustic wavelength is much smaller than the geometric features in the physics design [68]. The basic physics behind the Acoustics Module has been elaborated in Chapter 2 of this thesis. The Ray Acoustics interface follows the principle of the acoustic behavior at boundary discontinuities between two mediums, detailed in Section 2.5.5.

4.2.2 Parameters Setup

In general, the parameters setup in COMSOL modelling include the medium properties, boundary condition and ray properties.

First of all, the mechanical properties of the water, healthy prostate tissues, lesions and the urethra were defined via the speed of sound and the density in the simulation model. The frequency of the investigated acoustic wave used for the simulation was at 1.5 MHz.

Table 4.1 Mechanical properties used for simulation

Medium	**Speed of sound**	**Density**
Water	1465 m/s	1000 kg/m^3
Healthy prostate tissues	1540 m/s	1050 kg/m^3
Lesions	1620 m/s	1050 kg/m^3
Urethra	1670 m/s	1050 kg/m^3

The boundary condition is mainly used to define the way the acoustic waves behave when impinging on the boundary. In this simulation of the DACI design, both transducer surface and aquarium were set to freeze the incoming rays. This is due to the fact that this option can compute the phase and intensity at the moment of capture [67].

More detailed physics parameters regarding the ray properties was required to be set up in order to complete the computation of the trajectory, phase and intensity of acoustic rays. For example, the virtual source position was defined by giving the coordinates in three dimensions. The acoustic rays at the source position was set to radiate in all directions with the initial phase set to zero. The source power was set to $1\,W$. The material discontinuities of the interior boundaries were set up where the interface between two different media exists. This enables the ray tracing algorithm in the Ray Acoustics interface to calculate the direction of the refracted acoustics rays according to the acoustic behavior at the boundary elaborated in Section 2.5.5.

Last, but not the least, the mesh size is a crucial factor determining the performance of the simulation. As mentioned before, this Ray Acoustics interface is run under the prerequisite that the geometric characteristics need to be far greater than the acoustic wavelength. The finer the mesh size, the more accurate the result one can obtain from the design. The mesh shape chosen in the model was the free tetrahedral shape and the maximum size was set to be 1/6 of the acoustic wavelength in the water, the healthy tissues and the lesions, respectively [69].

4.2.3 COMSOL Simulation Results Analysis

1. 2D modelling with flat surface detector

The detailed design starts from the 2D sketch shown in Figure 4.7. It follows the design layout of the DACI, where the focus probe position is set to be right beneath the surface of the phantom. The large ellipse within the semi-diameter of

2.5 cm and 2 cm in two directions represents the prostate phantom used in the experiment. The three circles with the radius of 0.5 cm inside the ellipse refers to the lesions inside the phantom. And the thin rectangular plate refers to the transducer placed 0.15 cm below the phantom. The colormap on the right side refers to the sound pressure level in dB.

There are four material discontinuities in the simulation design: from the water background to the healthy tissues in the phantom, from the healthy tissues to the lesions in the phantom, and their reverse process. When the trajectories of the acoustic waves make contact with each boundary, the direction of some of the refracted rays can be found to bend. The angle of reflection and transmission at the material discontinuity are found according to the law of reflection and Snell's Law. The mathematical interpretation is articulated in Equation (2.21).

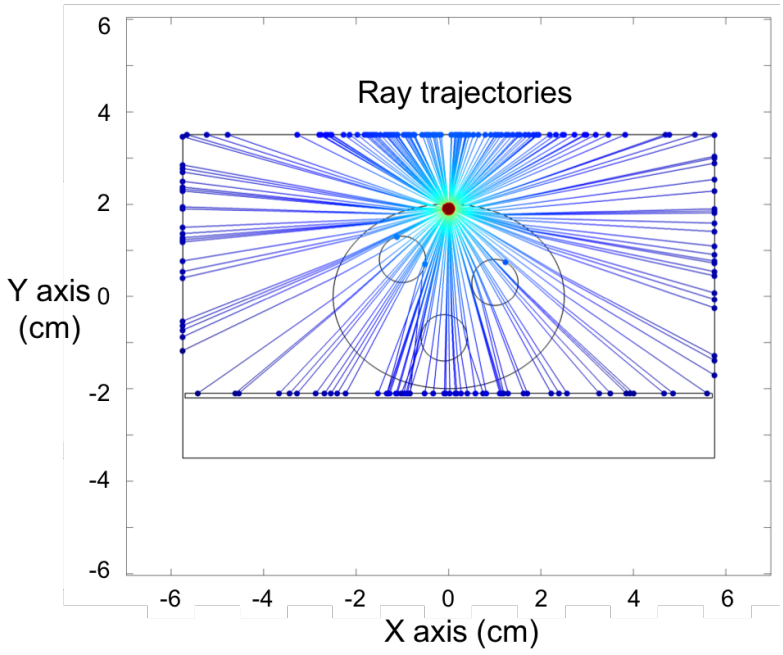

Figure 4.7 Ray trajectories in a 2-D COMSOL model using flat surface detector

In order to further understand the output results of the amplitude and the phase of the 2D model, a phantom without any lesions was also included for comparison. Presented in Figure 4.8, the dashed line refers to the sound pressure level (SPL) detected from the acoustic rays propagating through the healthy

phantom, while the solid line refers to the SPL of the rays passing through the diseased phantom. The smooth dashed curve appears as a dome shape where the peak occurs at the center axis position and slowly decreases with the increasing horizontal distance from the center. This is due to the fact that the transducer used in the simulation model has a flat surface so that the travel path length of acoustic rays varies along the transducer surface. The same fact applies to the solid curve. But the main differences between these two curves are the fluctuations located approximately between $-2\ cm$ to $2\ cm$ and beyond $4\ cm$.

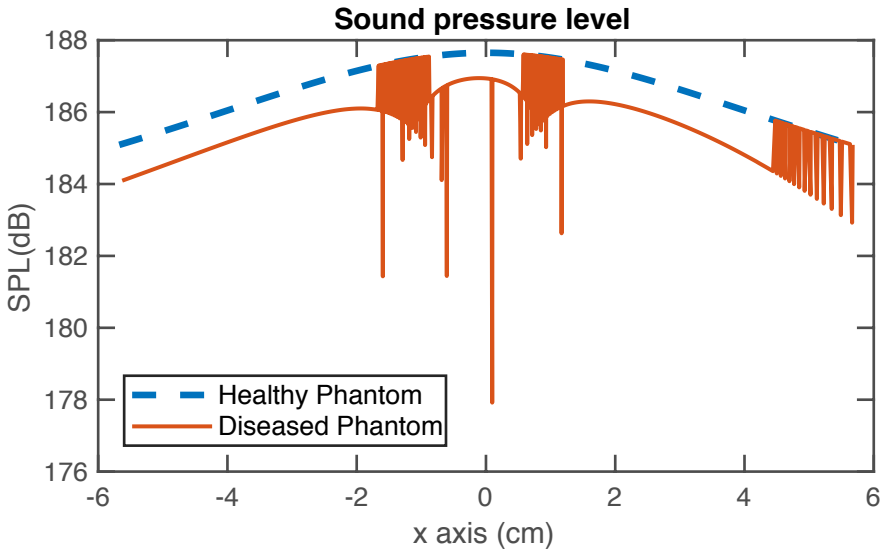

Figure 4.8 1D SPL detected by flat transducer from phantoms with and without lesions

The same phenomenon can be found in the unwrapped phase plot of the detected acoustic rays travelling through the two models (Figure 4.9). The dashed curve representing the phase obtained from healthy phantom exhibits a perfect parabolic shape where the phase difference between the center position and the edges on the transducer surface are approximately 155 $radians$. This relative large phase variation depends upon the acoustic wave frequency, travel path length and speed of sound in the medium, where the detailed relationships are explained in Equation (2.15). Illustrated in Figure 4.9, a closer investigation taken along the x-axis position from $-2\ cm$ to $2\ cm$ shows the detailed phase oscillations in the

zoomed in plot. The details beyond $x = 4\ cm$ are shown in Figure 4.10, where smaller variations caused by the trajectories change from the rays passing the right-hand side of the right lesion can be seen. Both the SPL and the phase plot presents oscillation features within the same region in the x-axis. Associated with the ray trajectories illustrated in Figure 4.7, the fluctuations in the data arise from the locations where the trajectories of the acoustic rays are altered when impinging on the boundary. More specifically, the directional change of the acoustic rays that make contact with the surface of the bottom lesion is quite visible, so as the rays contact with the right edge of the left lesion and the left edge of the right lesion. For instance, a phase shift of 6 radian is found around the location $x = 0.5\ cm$. In general, the refracted rays concentrated in the region around $-2\ cm$ to $2\ cm$ and beyond $4\ cm$ in x-axis can be detected in the corresponding oscillation area in the one-dimensional SPL and the phase plots.

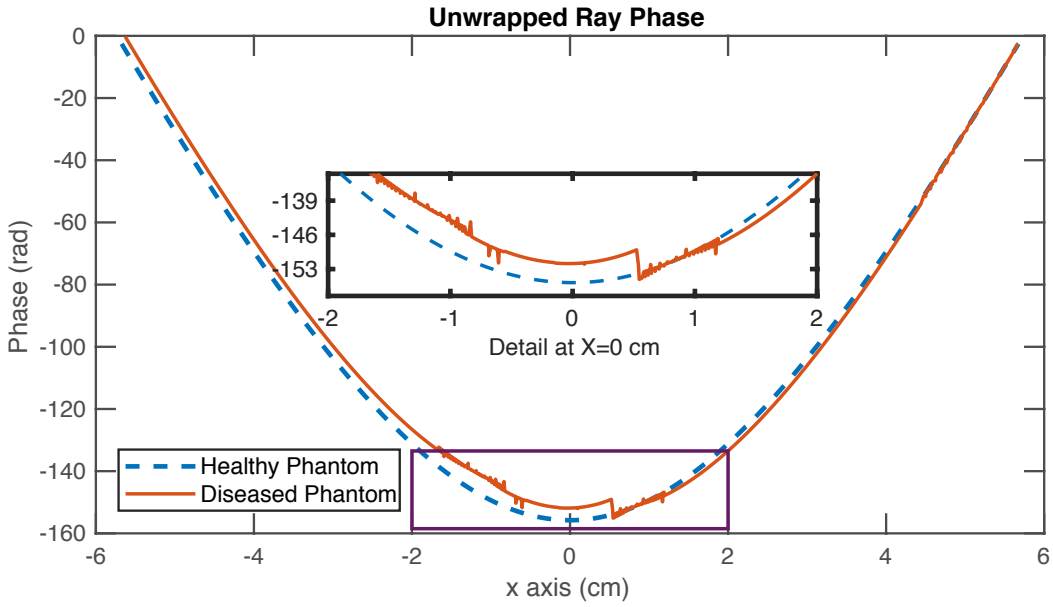

Figure 4.9 1D unwrapped phase detected by flat transducer from phantoms with and without lesions

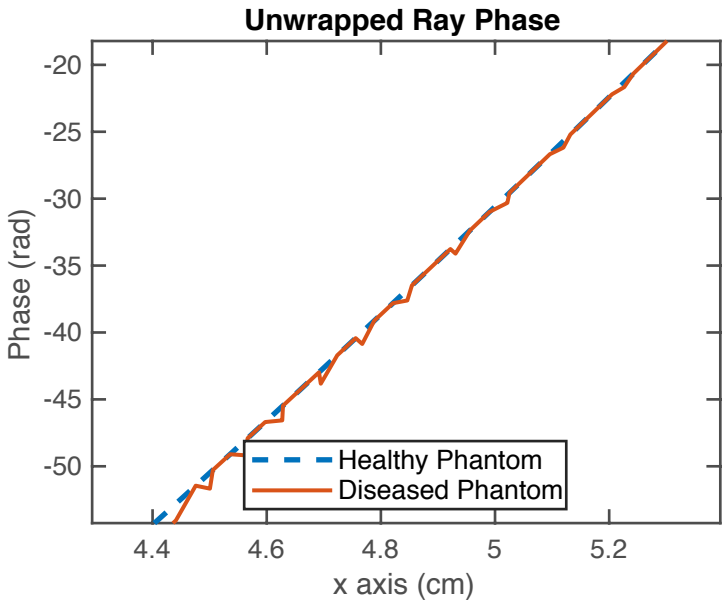

Figure 4.10 Zoomed in Figure 4.9 from x = 4 cm to 5.5 cm

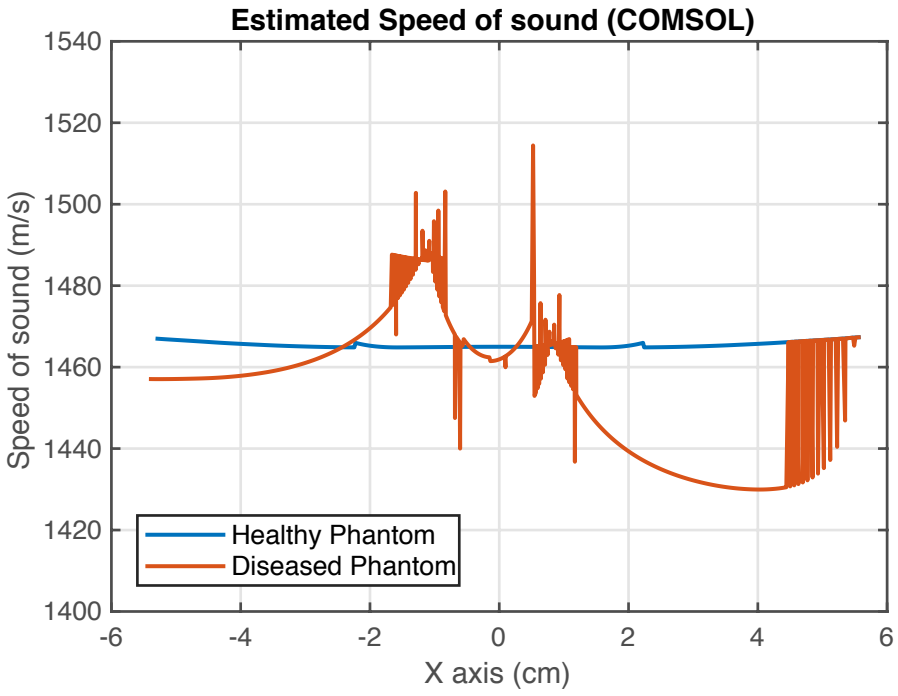

Figure 4.11 Estimated speed of sound along the flat detector (COMSOL)

The speed of sound variation along the 1D flat detector surface is presented in Figure 4.11. The acoustic rays passing through the healthy phantom has a nearly constant speed of sound around $1465\ m/s$, slight variations are found at the location where the rays hit the boundary between the water and the healthy

prostate phantom. Similar to the locations where phase shifts occur in Figure 4.9, the fluctuations in the speed of sound variation also occur at the locations corresponding to where the material discontinuities interfaces exist .

2. 2D modelling with curved surface detector

Next, a segment of arc representing a detector with curved surface was created to mimic the rotation motion of the point receiver in the DACI. Three simulations models were included in the comparison analysis, illustrated in Figure 4.12. The left model has an ellipsoid gland with three lesions and one urethra at the center, the middle model simulates a healthy gland with only one urethra, and the right model shows a gland without urethra and lesions, i.e., uniform material distribution. The angular distance to detect the rays hit on the curved transducer is from $-57.6°$ to $57.6°$. The distance from the scattering source to the detector is $6\ cm$, which is exactly the setup in the experiment. Another thing to note here is that the virtual source is being elevated outside the boundary of the gland so that more area inside the phantom can be reached by the acoustic rays.

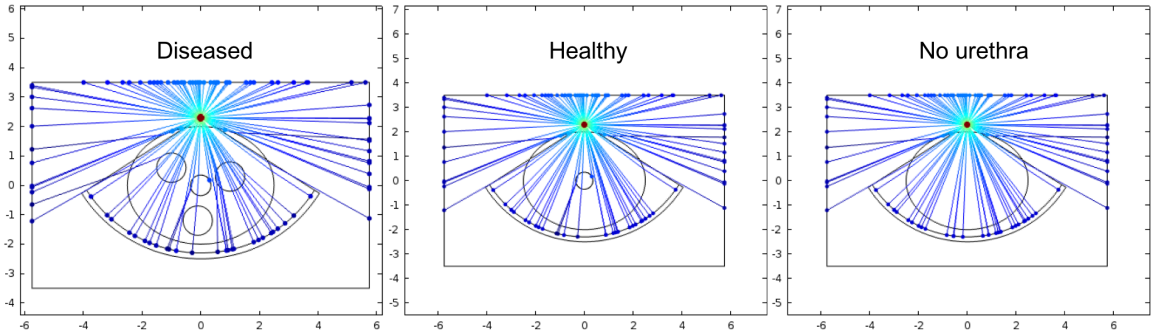

Figure 4.12 Ray trajectories in 2-D COMSOL models using curved surface detector

The SPL variation graphed in Figure 4.13 shows that the acoustic energy oscillates greatly around the edge of the urethra and the edge of the tumors. Compared to the SPL variation detected by the flat surface detector in Figure 4.8, the simulation result detected by the curved surface detector presents a smaller variation range mainly due to the smaller path length difference between the rays hit the edge and the center of the detector surface. In fact, the SPL variation of the uniform gland presents a slight curved shape, and it is due to the difference of the

acoustic ray path length in the gland material. The SPL variation obtained from the healthy gland follows the slightly curved shape most of the time, except the center region where the urethra (center circle) is placed. The significant jump occurs where the rays were bent at the edge of the urethra. And more oscillated regions can be found in the SPL variation obtained from the diseased prostate model. The jumps correspond to the locations of the lesions and the urethra.

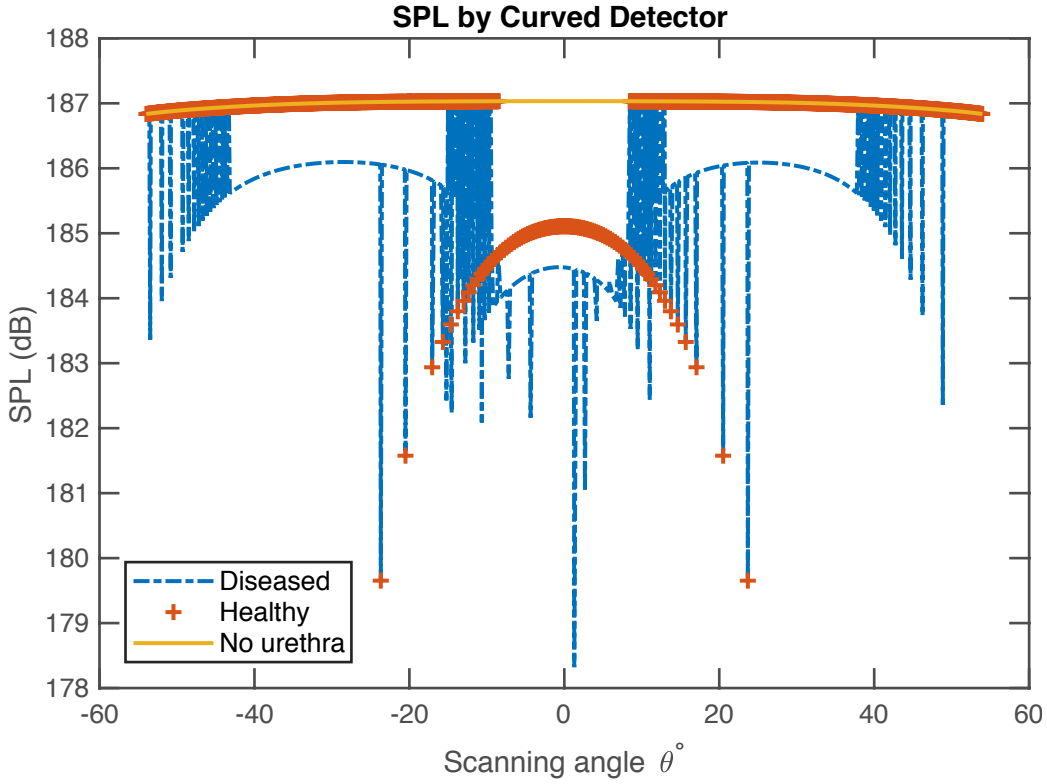

Figure 4.13 1D SPL detected by curved surface detector from diseased phantom, healthy phantom and uniform phantom

The unwrapped phase distribution displayed in Figure 4.14 further demonstrates the phase shift occurs where material discontinuities exist. The solid line refers to the phase curve of the phantom without urethra or any lesions. The relative smaller total phase variation, again, is due to the smaller path length difference compared to the results detected by a flat transducer. The unwrapped phase plot of the healthy phantom presents two symmetrical fuzzy regions at the locations corresponding to the edge of the urethra, and a bowl shape at the center

corresponding to the location of the urethra. The diseased phantom, graphed in dashed line, shows the phase shifts occur where material discontinuities exist. Due to the positions of the urethra and lesions, the trajectories of some acoustic beams hit the material discontinuity boundary are altered and lead to abrupt jumps in the unwrapped phase plot.

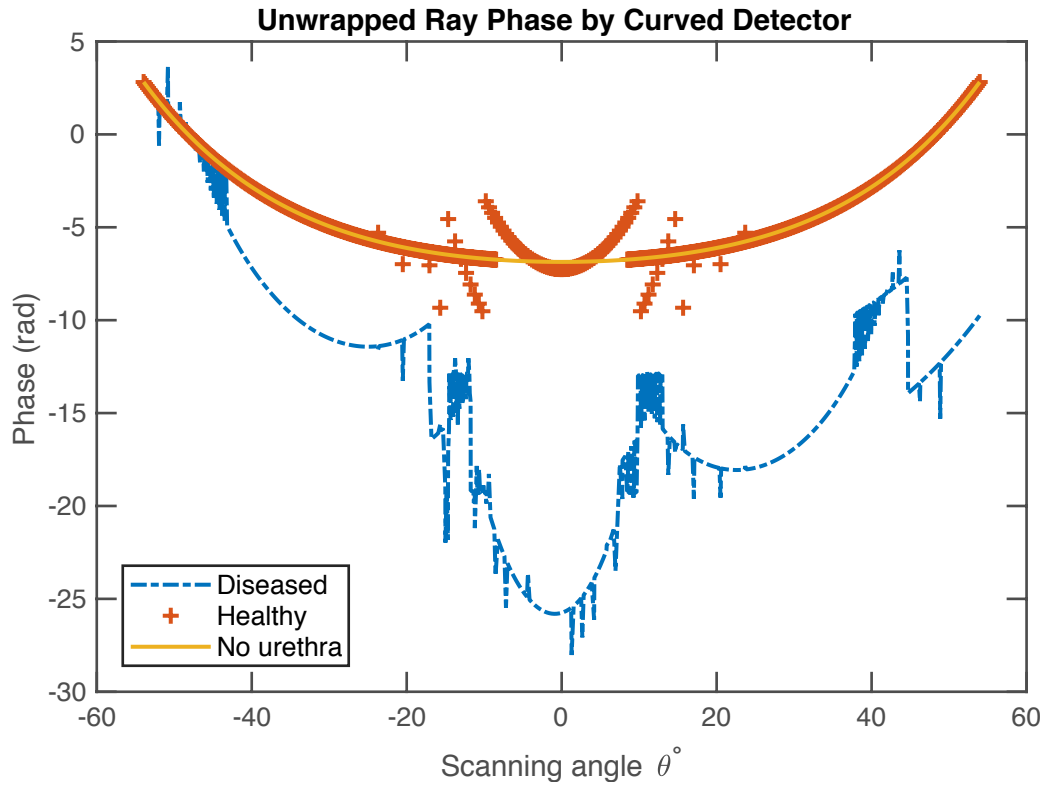

Figure 4.14 1D unwrapped phase detected by curved surface detector from diseased phantom, healthy phantom and uniform phantom

3. 3D modelling

The 3D model created in COMSOL inherited the same geometric layout and material properties as the 2D model, but added another dimension to the output making it a more realistic and straightforward presentation of the DACI design. The dimensions of the flat transducer are 11.3 cm × 8.8 cm × 1 cm. Figure 4.15 shows the virtual source scattering the acoustic intensity at all directions in 360 degrees. Some of the rays do not hit the flat transducer placed below the phantom since they are reflected back to the original medium rather than transmitted into

the next medium. It also corresponds to the absence of intensity on the sound pressure level image illustrated in Figure 4.16. The distortion in the shape is basically the projection of the spherical lesion onto the flat transducer surface.

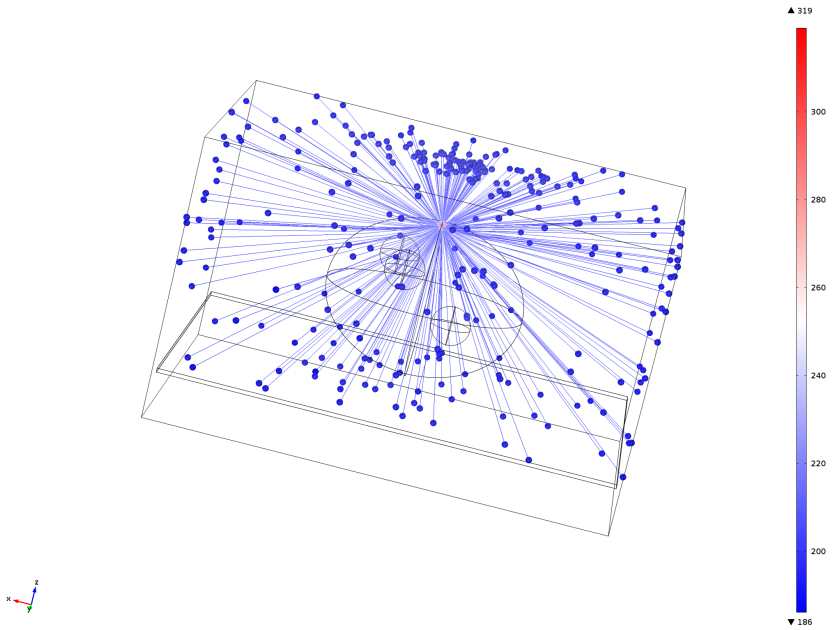

Figure 4.15 The ray trajectories in 3D COMSOL simulation design of DACI

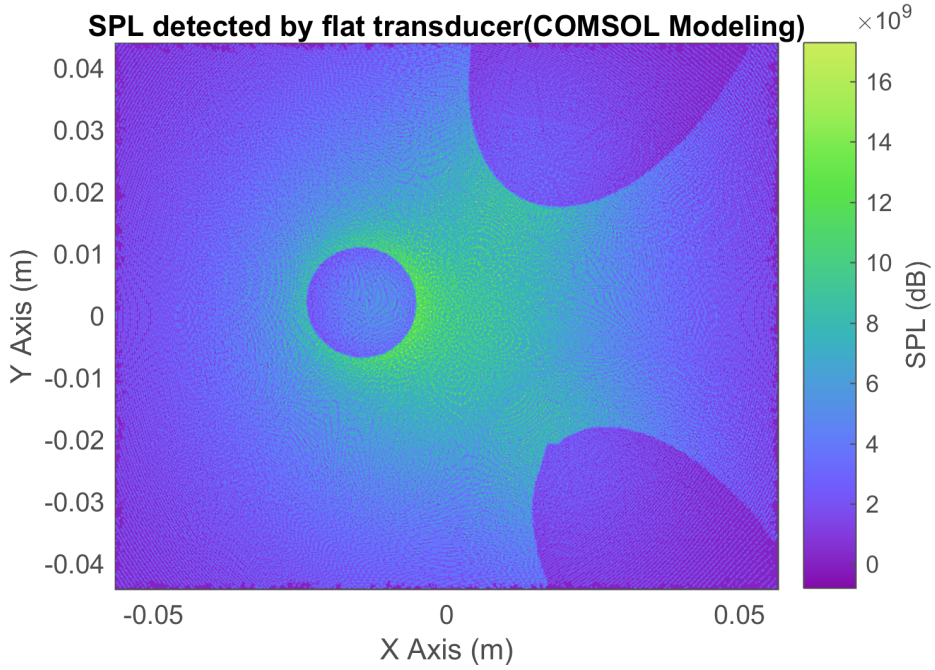

Figure 4.16 2D SPL detected by flat transducer from phantoms with and without lesions

The 2D wrapped phase image in Figure 4.17 exhibits a beautiful ring pattern that varies in the range between $-\pi$ and π. However, the periodic variation is distorted in three directions in which the spherical lesions exist.

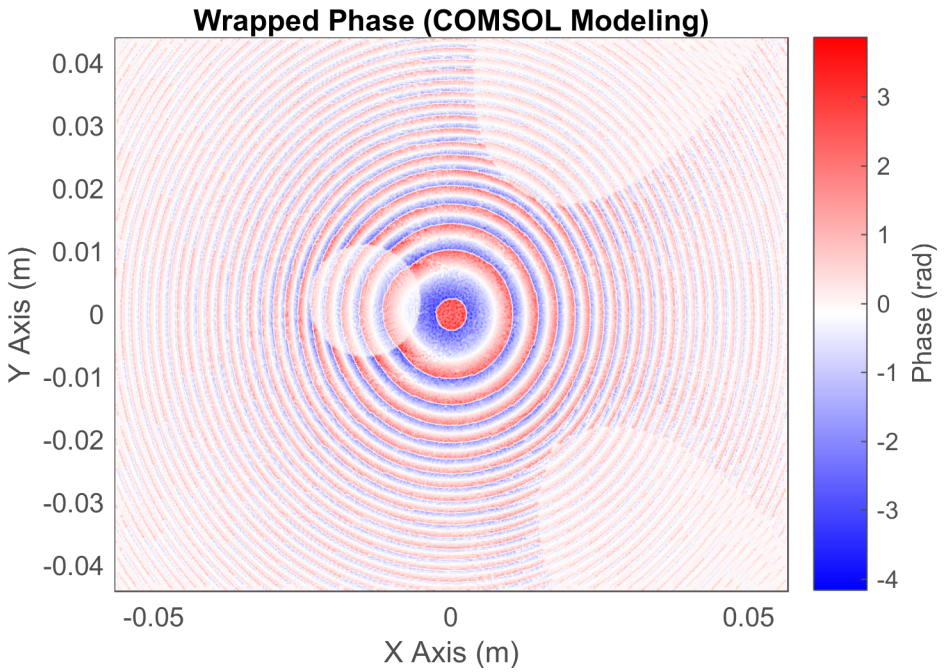

Figure 4.17 2D wrapped phase detected by flat transducer from phantoms with and without lesions

The simulation data generated from COMSOL and ZEMAX display similar results of both the intensity and phase distributions of the investigated acoustic rays on a transducer placed below the phantom. In ZEMAX model, the collimated beam from the emitter was brought to a focal point by the focusing mirror. And this focus probe position is proven to act as a virtual source with the intensity scattering in 360 degrees, making the detection of the phase possible. Both ZEMAX and COMSOL model demonstrates that the scattered intensity from the virtual source position can provide valuable information about where the lesions are located. Currently the simulation is performed for fixed source. To render the 3-D reconstruction of the phantom with lesions, the virtual source needs to be translated so that enough image slices for reconstruction are produced. Both the

projection path and suitable image reconstruction methods need to be investigated in the future work.

Chapter 5 Experiment Apparatus

This chapter details the design of the stepper motor control stage to rotate the point receiver and the linear translation stage to move the specimen. The configurations for the host computer and the USRP N210 are explained, and the signal acquisition module is established to measure both the phase and the intensity from the received signal. Also, the alignment between the emitter and the receiver is also performed since the geometrical layout is important regarding the design of DACI.

5.1 Motion Control Mechanism

5.1.1 Motor Control Stage

During the experiment, the rotation of the point receiver was required. As indicated previously in the design layout presented in Chapter 3, the point receiver from Valpey Fisher rotates around the prostate phantom and collects signals at multiple points along the path with a fixed time interval. The travel is a curve around the center axis of the motor shaft, having a radius of 6 cm. The motor rotation stage controls the motion of the phantom remaining relatively stable during this time.

A stepper motor from LIN Engineering was chosen to rotate and then rest its motion. It runs by stepping its rotor by 1.8 degree and then a holding torque is produced to pause its motion. Furthermore, the stepping angular distance and the direction were controlled by digital pulses sent to the driver. A bipolar stepper motor is suited for this application since it can provide a higher torque compared to a unipolar motor. This torque is needed to drive the shaft, which the point receiver is attached. Considering all the above factors, a high torque bipolar motor 4218L-01-11 with the step resolution of 1.8° and a National Electrical Manufacturers Association (NEMA) size 17 was purchased from LIN ENGINEERING[70]. The specifications are listed in Table 5.1.

Table 5.1 Specifications of motor 4218L-01-11 from LIN ENGINEERING [70]

Parameter	**Detector**
Dimension “A” Max	1.86 inch (47.2 mm)
Dimension “B” Max	1.67 inch (42.4 mm)
Amps/Phase	2.00 A
Torque	75.00 oz·in (0.53 N·m)
Resistance (Ohm/Phase)	1.2 Ω
Inductance (mH/Phase)	2.6 mH
Inertia	0.37 oz·in2
Weight	0.70 Lbs
Number of Leads	4

In order to enhance the step resolution to finer than 1° and the stability while turning, a microstepping driver was used with the stepper motor collect data without too much disturbance. The microstepping driver M542 was powered by an external power supply of 12 V having the corresponding interface ports to connect with the NEMA size 17 2-phase stepper. In the experiment, the stepping resolution was set to divide one full step into 2 microsteps. This enables smooth tuning with low vibrations good for the sensitive phase measurements.

After deciding on the stepper motor and the microstepping driver, the question became how to control the stepper motor work with the microstepping drive with a digital signal. Arduino is an open source platform that provides flexible control over all kinds of programming projects [71]. Arduino Uno, equipped with the 8-bit AVR microcontroller ATmega328P [72], is very inexpensive, easy-to-use and capable of the serial communication between the host computer and the Arduino board. The programming language is based on the AVR C library and a user-friendly integrated development environment (IDE) can be downloaded for free.

More conveniently, MATLAB has the hardware support for Arduino in terms of the connection to and the control of the Arduino input and output [73]. In the experiment, the digital signal was sent through the serial port by MATLAB to the Arduino Uno board. The board was connected to the host computer via a USB cable. Then the Arduino sent the corresponding commands to the mircostepping driver. The stepper motor was interfaced with the microstepping driver and converted the digital signal to the mechanical motion as commanded. The turning direction, the angular distance and the time interval between each step were all programmed into the code burnt on the board.

This low cost and uncomplicated rotational stage consists of one bipolar stepper motor, one microstepping driver and one microcontroller driver implemented in the experiment of DACI with the aid of the MATLAB support package. The following figure illustrates the connection between each component included in the stage control.

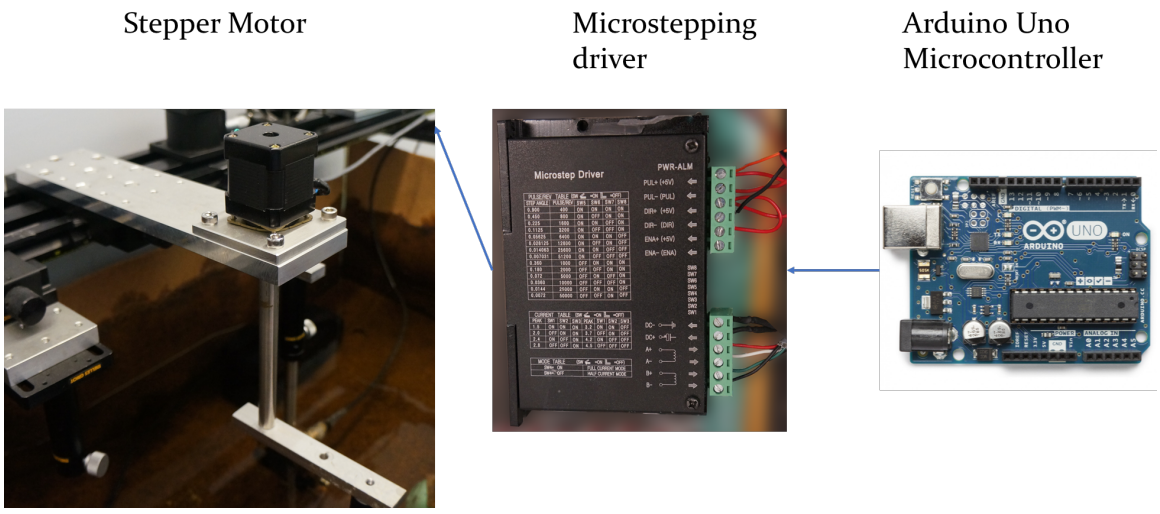

Figure 5.1 Stepper motor rotation control stage

5.1.2 Linear Translation Stages

Another moving component involved the experiment was the prostate phantom. At the time of the experiment, its position was adjusted along the three axes in the Cartesian coordinate system. The inward and outward translation is the

first dimension, x. The horizontal translation is the second dimension, y. And, the translation along the vertical direction is the third one, z.

The high-speed actuator, LTA-HS from Newport, was used to improve the precision control of the stage translation with a load capacity of 40 N. The travel range is 50 mm and the maximum travel velocity is up to 5 mm/s. The minimum incremental motion is 5 μm achieved by the DC servo motor [74].

The motions of these motorized actuators are driven by the ESP300 (Enhanced System Performance) motion controller driver from Newport Corporation [75]. Its main feature beneficial to DACI is that it provides digital signal processing architecture and real-time high-speed command processing ability. Each of the three linear actuators was connected to the ESP300 on the rear panel with three 25-pin D-sub connectors. The RS 232-C interface also on the rear panel connected to the host computer to receive digital signal commands regarding the travel velocity and distance. The 3 axes translation motion can also be manipulated manually through the jog buttons on the front panel. The display window on the front panel shows the current positions of the three actuators, which is a bonus for real-time monitoring purposes. The front panel of the ESP300 motion controller in the lab is shown in Figure 5.2.

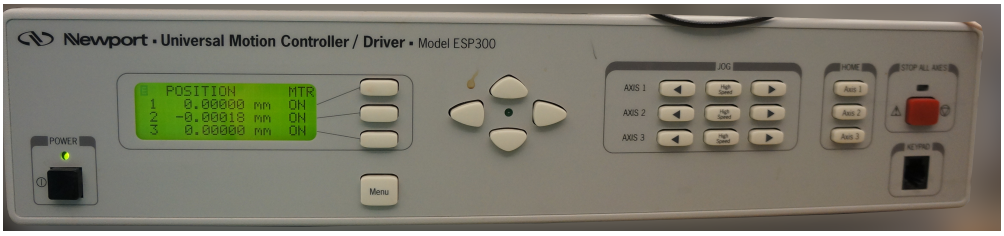

Figure 5.2 Front panel of ESP300 motion controller

5.2 Signal Acquisition Device Setup

The introduction of the SDR technology and the hardware implementation of the USRP platform were described in detail in Chapter 3. In this section, an explanation of how to setup the connection between the host computer and the USRP device is given.

5.2.1 USRP Connection Test

In order to use the Communication System Toolbox support package for the USRP in MATLAB, several setup procedures are necessary to follow after connecting the host computer with the USRP N210 device via Ethernet cable directly. First, the USB driver needs to be installed that ensures the firmware on the host computer and the USRP match with each other. Second, the host computer is configured for a valid Ethernet connection [76]. Essentially, a Network Interface Card (NIC) is required to communicate specifically with the USRP N210 device. There are different commands to verify the successful communication between the host computer and the USRP N210. The complete information regarding the USRP N210 FPGA and the daughterboards can be found in Appendix A: Verify MATLAB Connection to USRP Radio.

5.2.2 Radio Transmitter and Receiver Setup

In Section 3.3.4, the data flow between the host computer and the radio were clarified. The flexibility of the USRP platform reflects on how a user defines the parameters involved in the radio characteristics design, what type of baseband digital signal one chooses to stream, etc. Here, the concrete solution regarding the configuration of the transmitter and receiver block is articulated. Fundamentally, the premise of the design considerations is to obtain the phase shift measurement from the point receiver located in the aquarium.

1. Determine the baseband digital signal sent to the USRP from the host.

First of all, the digital baseband signal sent to the USRP N210 from the host computer was the starting point of the data flow during the experiment. Eventually, the analog signal coming out from the RF front end on the radio was expected to be a sinusoidal wave with a single frequency and zero initial phase. Following this guideline, the simplest way to generate a sinusoidal signal at the front end was to feed a frame of baseband digital samples having an amplitude of 1, a frequency of zero and an initial phase of zero. After processing through the FPGA

and the LFTX daughterboard, the frequency of the output analog signal should be the same value as the center frequency of the carrier wave used in the mixer of the DDC component. The amplitude does not affect the phase shift measurement, but its existence is necessary to carry the phase. In addition, the Barker code sequence, introduced in the section 3.3.7, was attached to the beginning of the digital for the synchronization purpose. A frame of the digital sample fed from the host computer into the radio is plotted in Figure 5.3.

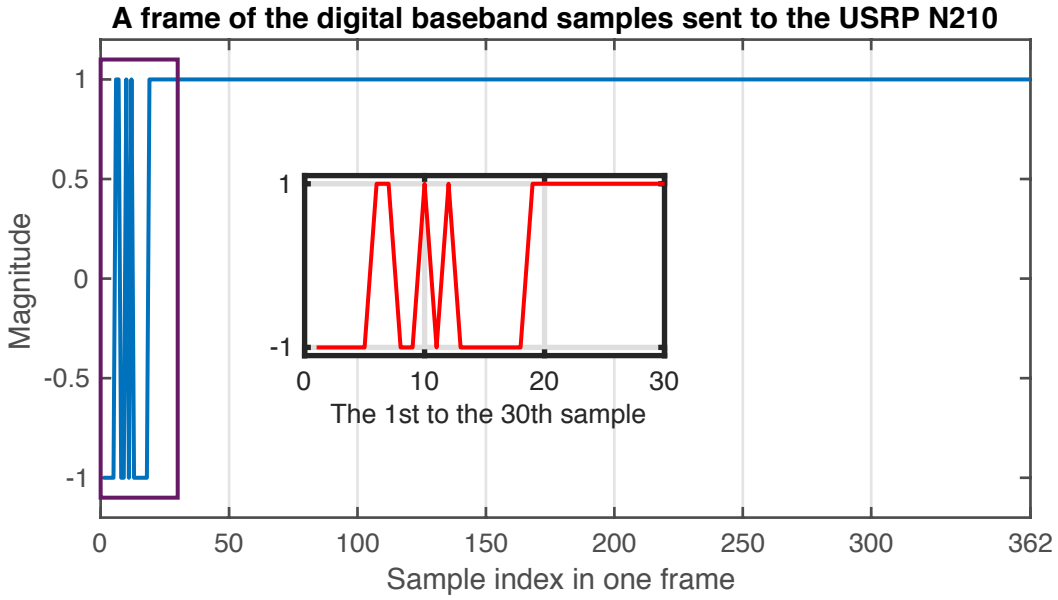

Figure 5.3 Example of the digital sample sent to the USRP N210

2. Setup the parameters on the transmitter side.

Next, the parameters setup on the transmission path of the USRP N210 were taken care of. The center frequency f_c, in this work, is the same as the desired frequency of the RF analog signal at the front end of the LFTX daughterboard because of the DC input from the host computer. Since only a single frequency is needed, it is also the carrier frequency generated from the local oscillator to mix with the input signal.

Another vital operation involved in the USRP radio is the sampling of the signal at different stages in the data transmission path. The master clock rate in the USRP N210, $f_s = 100\, MS/s$, is used to sample the IF digital signal, which has

already been up converted from the baseband input. Then the IF digital samples are sent to the DAC to be converted into the IF analog signal at the same rate. With the interpolation factor N, the digital samples sent from the host computer is sampled at the rate of f_s/N. In the experiment, the interpolation factor was an integer of 4. The baseband frequency sample rate can be a much lower value compared to the master clock rate to keep a high system processing and response speed.

The gain on the LFTX daughterboard is not programmable. The frame length, also known as the frame size, is the number of digital samples streamed to the USRP hardware in one burst. As discussed previously, it is recommended to take the value of 362 based on the maximum transmission unit of the 1 Gigabyte Ethernet cable connection. However, in a lot other applications in RF communication system design, it can be set to any value below 4000.

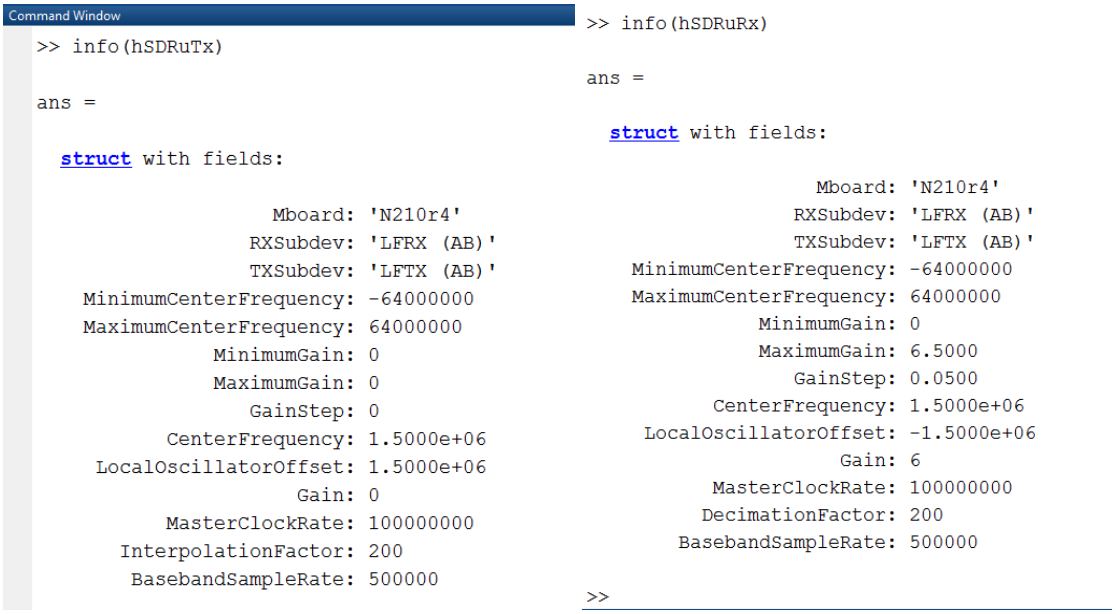

Figure 5.4 USRP transmitter and receiver parameters setup by MATLAB

3. Setup on the receiver end.

Most of the parameters had the same setting since a balanced transmitter and receiver is easier to interpret the data. The gain on the LFRX daughterboard is

tunable from 0~6 dB with the increment of 0.5 dB. The main use is to amplify the signal with a scale factor, and does not affect the intrinsic properties of the signal. Figure 5.4 presents an example of the parameters setup for both of the transmitter and receiver.

4. Determine the scanning time at each scanning position.

When the motor was commanded to turn to the next scanning position, the communication between the host computer and the radio was initiated as well. The total scanning time at one position T_{sto} was assigned to determine the amount of time that the USRP N210 keeps communicating with the host computer. During this period of time, the USRP receives one frame of samples after another and counts towards the end of the scanning time.

5. Interpret the signal and produce the phase and amplitude information.

As mathematically explained in Equation (3.7), the received signal on the host computer is complex digital baseband samples. The phase angle of the signal from the receiver can be preserved by the unique I/Q notation method in the USRP. In the I/Q method, the phase shift is directly interpreted by taking the inverse tangent between imaginary and real parts. The second way, also covered in chapter 3, is the Fast Fourier transform method. The number of FFT depends upon the frame size and needs to be a power of 2. Each frame of the received samples at the RF front end of LFRX daughterboard was performed with the FFT and the Hanning window.

5.3 Graphical User Interfaces control

The graphical user interfaces (GUI) built in MATLAB is the core of the real-time control of the DACI system. It enables a user to run the application simply by using operations like point and click without learning the programming language. It integrates the control power of the motor rotation stage, 3-axis actuators translation stage and USRP signal acquisition platform onto one interface. The GUI was first created by McCaugherty [45]. Then the research engineer, Peter

Jacqueman, who also contributed greatly to the function modification in order to better suit DACI's application. When the USRP N210 and Arduino Uno were implemented, the development of the GUI came to the current phase where the serial communication of these two separate platforms were integrated into the interface.

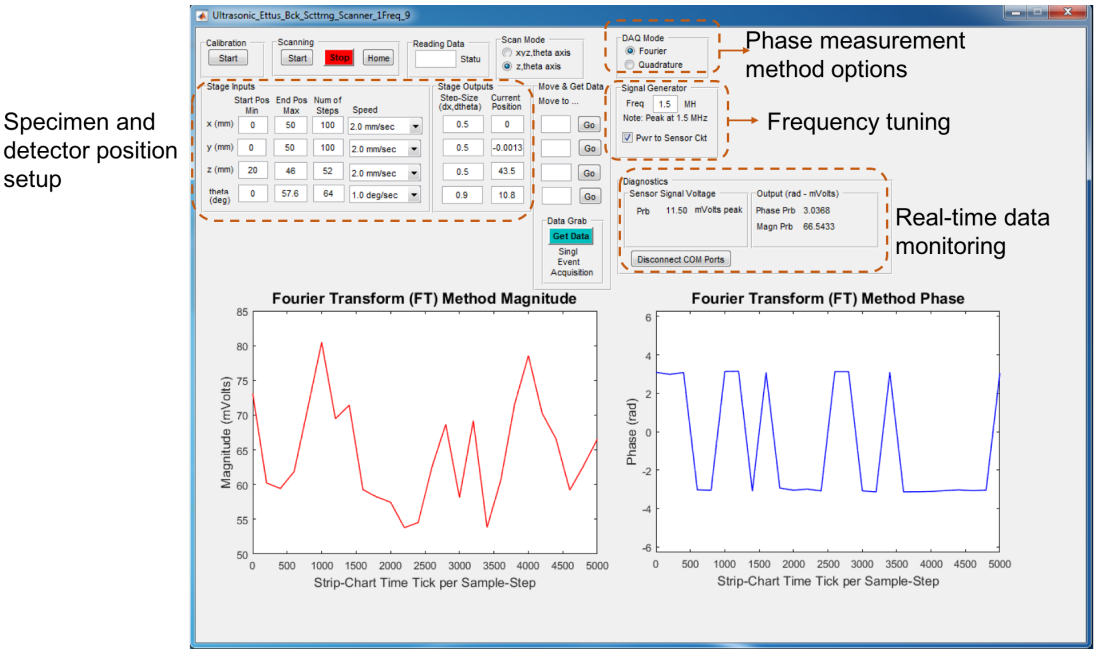

Figure 5.5 GUI control of DACI application

As illustrated in Figure 5.5, the main functions included in this interface are detailed as following:

1. Center frequency tuning

The "Signal Generator" enables the user to tune the frequency value of the desired RF analog signal sent to the emitter, ideally between 1-2 MHz according to its resonant frequency measured by Atalick [44].

2. Scanning geometry setup

First, the "Scan Mode" specifies the option "z, theta axis" to move the relative geometry of the phantom and the receiver. The current design only requires the point receiver to rotate and the phantom to move upwards and downwards. Since the focus probe position was determined by aligning the emitter and mirror, the

phantom position in the x and y directions were fixed in the experiment. This is why only the vertical translation was operated rather than all three axes. The travel range, the initial and ending position of the phantom and the receiver can be adjusted in the “Stage Inputs” section. The number of steps denotes how many points of data the receiver is going to collect. The “Stage Outputs” indicates the size of each step and the current position of the prostate and the receiver. During the experiment, when the receiver finished rotating the angular distance in one direction, the phantom would receive a command to move to the next required position. And then the receiver would start to turn in the opposite direction and so forth.

3. Data acquisition method

The “DAQ Mode” offers the options to display the real-time measurement either from the I/Q method or the FFT method, whereas the “Reading Data” section tells the current output phase measurement depending on the method.

4. Monitoring the experiment

Eventually, the real-time measured phase and amplitude are displayed in the “Diagnostics” sections, where the plots are presented in the two relatively large windows located at the bottom of the GUI.

5. Other miscellaneous functions

Directly from the press buttons, one can infer the use of the “Scanning” module is to manipulate the serial communication with the Arduino Uno. Once the “start” button is pressed, the host computer sends the digital signal to inform the microcontroller board of the stepper motor that the motor shaft can start. The “Stop” button is to cease the scanning so all the components will be halted and the radio transmitter and receiver block will be released from the designated IP address. “Data Grab” is another way to investigate the measurement data at a single point or position.

5.4 Apparatus Alignment

The alignment between the mirror and the emitter was conducted on an optical table with the aid of a red helium-neon laser product, JDS Uniphase 1125/P [77]. A beam expander was placed in front of the laser to resemble the acoustic beam characteristics of the emitter used in DACI. The optical rail which holds the emitter and the receiver was placed in the laser propagation path. With the acoustic emitter removed from its holder, the parallel laser rays from the beam expander made contact with the focusing mirror. The height of the mirror was adjusted to ensure the beam was centered on the mirror surface. The tilt angle of the mirror with respect to the optical rail was found to be around 23° according to the critical incident angle at the boundary between the water the aluminum mirror (see Equation (2.26)). This angle ensures most of the acoustic beam in the aquarium impinged onto the mirror was reflected. The angle was tuned slightly during the alignment operation to let the collimated laser beam appear less distorted on the mirror. Then the focus probe position was found by adjusting a white board along the path of the reflected beam from the mirror until the sharpest focus point was detected. The relative position of the focus probe position was measured in two directions. The horizontal position is the distance with respect to the focusing mirror, whereas the vertical position is the distance away from the edge of the optical rail.

5.5 Apparatus Setup

Following the layout design presented in Section 3.1.1, the experiment focused on where to place the emitter, the phantom and the receiver so that they fit into the aquarium. More specifically, deliberate considerations were given to where the rotation stage should be placed and how the point receiver can rotate around the center of the motor axis. It was solved by using a stainless-steel shaft attached to the center of the stepper motor. And then a thin aluminum plate was screwed onto the bottom the shaft on one end. The other end of the plate was screwed with the shaft of the holder of the receiver. The distance between the two holes determined

how far the point receiver should be away from the motor shaft. Due to the geometrical limitations, the current angular travel range of the motor rotation stage was set from 0 to 57.6° instead of a whole revolution. With the microstepping driver, the step size between each angular position was set to be 0.9°.

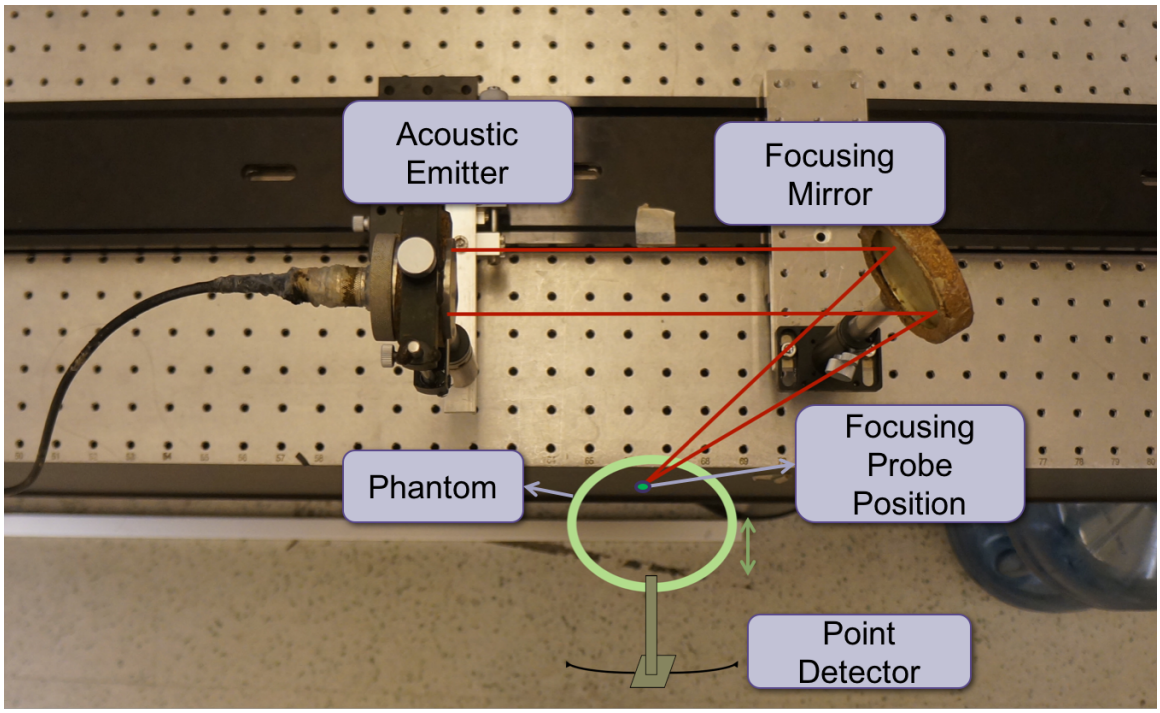

Figure 5.6 Alignment between the emitter and mirror

The holders for both the emitter and mirror were attached to the aluminum plates, which were screwed on to the optical rail carriers. The carriers enabled the two components to be held by the optical rail from the Melles Griot. The centers of the emitter and the mirror were in line with each other having a distance of 23 cm apart. The prostate phantom was maneuvered by the object arm of the linear translation stage, which is controlled by the motorized actuators. A thin aluminum bracket was designed to hold the phantom in a position where its boundary was close to the focus probe position. In the current experiment scanning geometry, the maximum travel range of the actuators was from 0 to 32 mm, with an incremental step of 0.5 mm. In Figure 5.6, the scanning geometry and the layout of

the components in the DACI's experiment is presented. When running the experiment in the aquarium, the optical rail was flipped facing downwards in order to immerse every component into the aquarium.

Chapter 6 Experiment Results

This chapter presents the phase information collected from the signals measured by the point receiver. First, the speed of sound in the water was measured using the time-of-flight method. Second, the importance of proper parameters used in the USRP platform was validated by comparing the phase measurement at a single position with different baseband sampling frequency and frame length. Then, the two-dimensional phase measurement of the prostate phantom was investigated and compared to the simulation results.

6.1 Speed of Sound in the Water Aquarium

The speed of sound in the water c_{water} was measured at the early stage of the experiment of DACI using the time-of-flight method to provide a reference for the simulations and the analysis of the experimental results. There is latency time between the transmission and reception, the time delay between the first frame of the received samples and the corresponding transmitted frame is not strictly the travel time of an acoustic ray emitted from the surface of the emitter to the point receiver. Therefore, in order to diminish the effect of the latency time, the time of arrival was collected multiple times with the various separation distances between the emitter and the receiver. During the measurement process, the point receiver was placed face to face with the acoustic emitter so that the distance between them can be easily manipulated. Suppose the latency between the transmission and reception front end is t_0, and the separation distance between the two components is S, the time of arrival, TOA, can be found in Equation (6.1).

$$TOA = t_0 + \frac{S}{c_{water}} \tag{6.1}$$

By varying the separation distance from $14.605\,cm$ to $33.655\,cm$ with an increment of $1.27\,cm$, the corresponding time of arrival (TOA) for each distance was recorded. Later, the relationship between the TOA and the separation distance was found using the polynomial curve fitting approach. The polynomial

coefficients used to construct the curve to fit the measured data were calculated based on the least square method where the sum of the squared residuals needs to be minimized. The residual refers to the difference between the measured data and the corresponding fitted value. Presented in Figure 6.1, the measured TOA is denoted by the dots, whereas the solid line refers to the fitted curve of the measured data and is extended to find the intercept with the time axis. The linear curve agrees with the relationship between the TOA and the separation distance between the emitter and the receiver, as described in Equation (6.1). As a result, the measured speed of sound of the water in the aquarium is 1465 m/s, which is the inverse of the slope of the fitted curve. The intercept of the curve with the time axis gives the latency time between the two front ends on the USRP platform, which is about $127\mu s$.

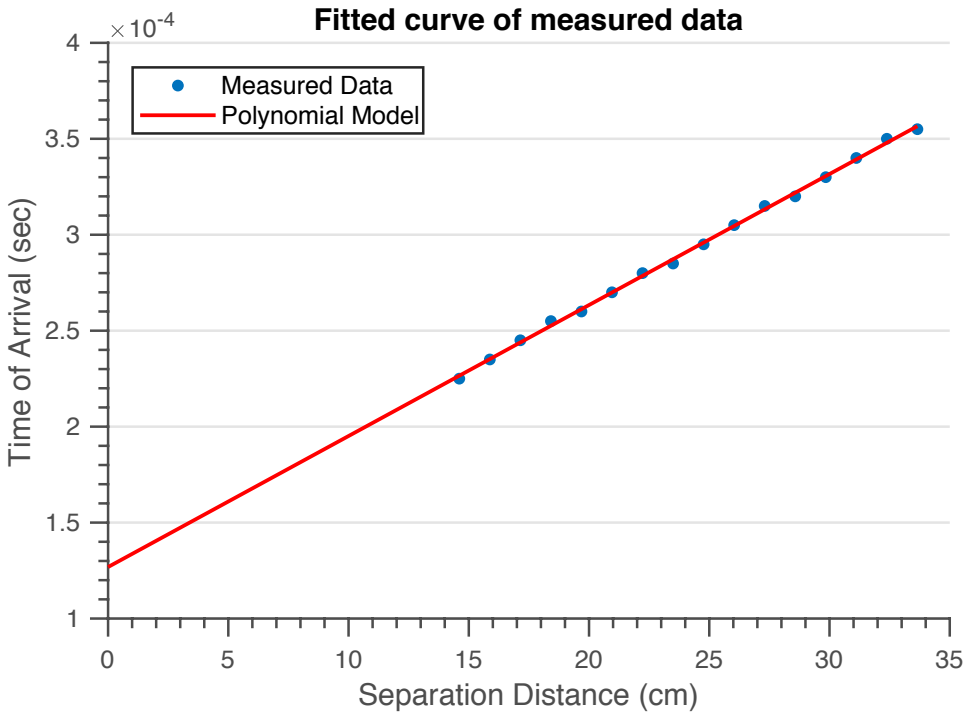

Figure 6.1 Fitted curve of the TOA and the separation distance

6.2 Phase Information

In chapter 3, the principle of USRP platform explained how the phase shift of the acoustic beam detected by the point receiver is preserved during the process of

sending the received analog signal into the host computer. In chapter 5, the parameters configurations of the transmitter and receiver blocks of the USRP indicated what matters in terms of phase measurement. How the detected phase was measured at a fixed position using I/Q method and FFT method is explained as following.

6.2.1 The Effect of Baseband Sampling Frequency

When the receiver stays stationary at a fixed position, the dwelling time depends the period of time the host computer commands it to stay. In the experiment, the host computer commanded the data streaming to last for 3 seconds. The MATLAB support package implements the method of frame-based sampling in the USRP design, and the mathematical interpretation was explained in Section 3.3.6. Basically, the digital samples from the host computer are burst in a packet of fixed frame length. In the experiment, each frame has the frame length $FL = 362$, i.e., 362 digital samples. The master clock rate is $f_s = 100\ MS/s$, and the interpolation/decimation factor is $N = 200$, which provides 500 KHz baseband sampling frequency. Thus, the sample interval between each individual sample is $\frac{N}{f_s} = 2\ \mu s$ and the sample time for a frame of 362 samples is $FL \times \frac{N}{f_s} = 724\ \mu s$. Therefore, there will be 4144 frames of data streamed into the host computer in during these 3 seconds.

As introduced in Section 3.3.7, a 13-bit Barker code sequence of 20 was attached to the beginning of each frame for synchronization purpose between transmission and reception. Thus, the corresponding barker sequence head was removed at the receiver end and the missing tail of the received samples was filled with the average of the preceding samples in the frame so that each frame still remains the same size. After each frame was sent back to the host computer, the computer end stores each frame into a two-dimensional matrix, where each row refers to one frame of samples.

Figure 6.2 presents the magnitude calculated for each frame during the entire 3 seconds. When the baseband sampling frequency is 250 kHz, the number of frames is 2072, whereas for 500 kHz baseband sampling frequency, the number of frame is 4144. The magnitude in both plots peaks near 35 mV and the oscillation occurs every few frames after the initialization period. The up and down in the magnitude was considered due to the periodic variation in the magnitude of sinusoidal wave.

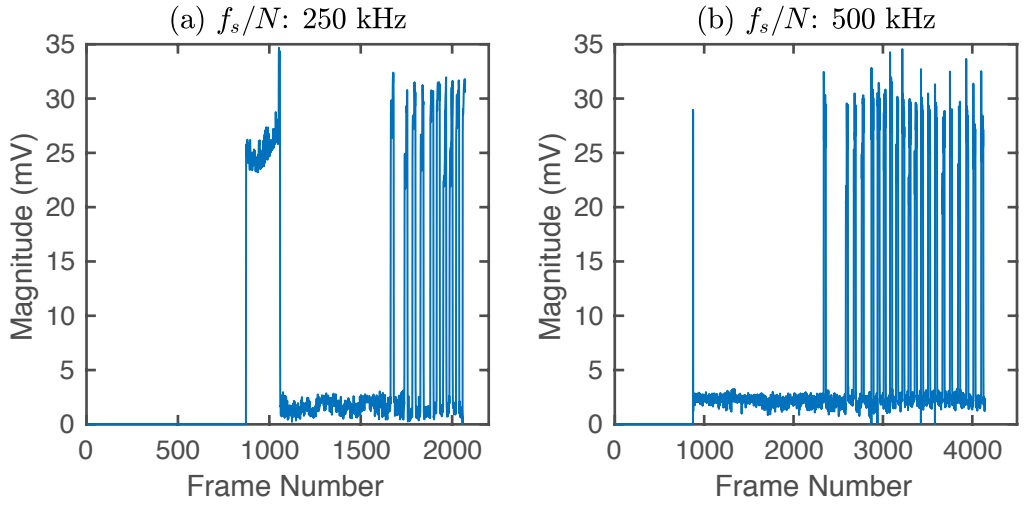

Figure 6.2 The magnitude for each frame of the received samples (frame size =362) using FFT method. (a) 250 kHz baseband sampling frequency (b) 500 kHz baseband sampling frequency

Next, the phase comparison between these two scenarios are illustrated. All the phase measurements at one fixed location after unwrapping processing are displayed in Figure 6.3. In (a) and (b), the phase measurements are taken by each frame using the FFT method, where 250 kHz baseband sampling frequency is used in (a) and 500 kHz is used in (b). As indicated in Equation (2.15), the phase variation along the propagation path is linearly increasing over time. Compared with the lower sampling frequency at 250 kHz, the measurement using 500 kHz baseband sampling frequency gives a smoother linear curve. Another thing to be noted here is that there exists a part of zero region at the beginning, and starting at around the 800th frame the phase starts to jump. This is due to the fact there is

always a latency time between the transmission and reception front end on the USRP. The graphs, (c) and (d), on the other hand, shows the phase unwrapped by each received individual sample during the entire 3 seconds data streaming period. Both scenarios present a much better linear curve. Another way to measure phase using the I/Q method, displayed in (e) and (f), outputs the data by the mean value of each frame instead of each sample. It can be seen that graph (f) using 500 kHz gives a more reliable linear curve compared to graph (e).

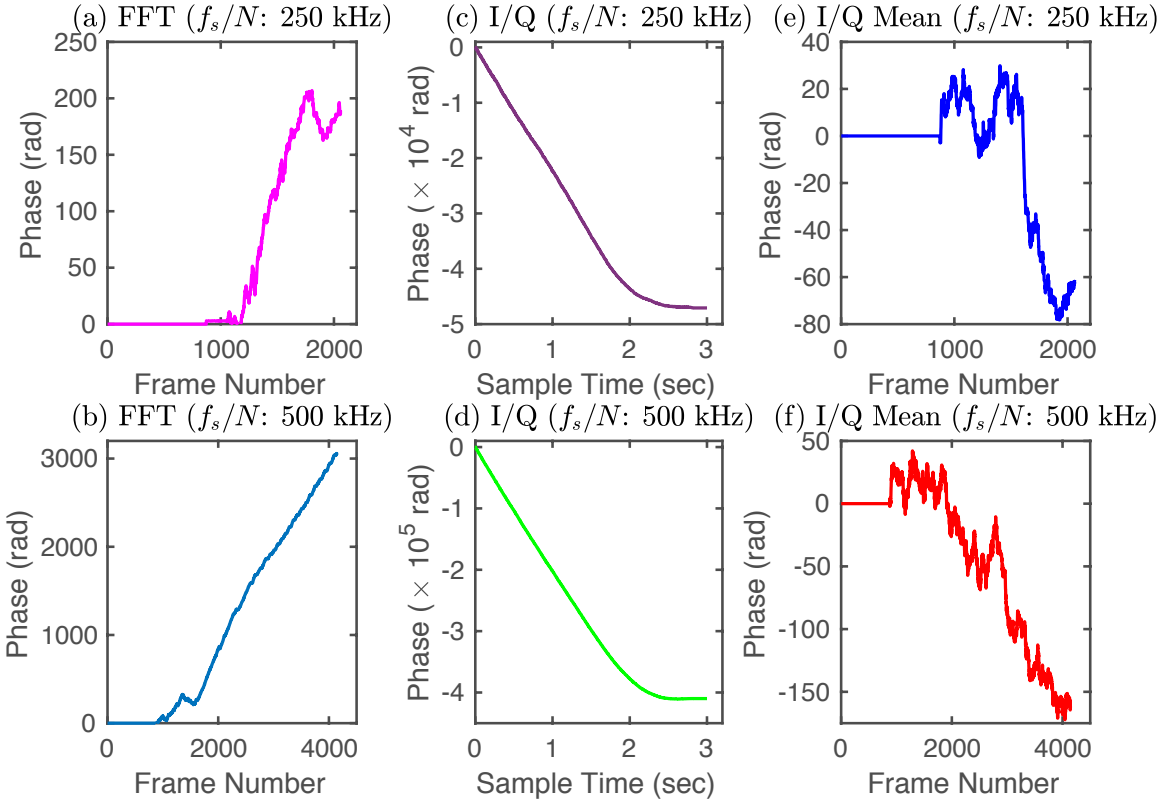

Figure 6.3 Unwrapped phase measurement at fixed position within 3 seconds with different baseband sampling frequency by the FFT and I/Q methods

6.2.2 The Effect of the Frame Length

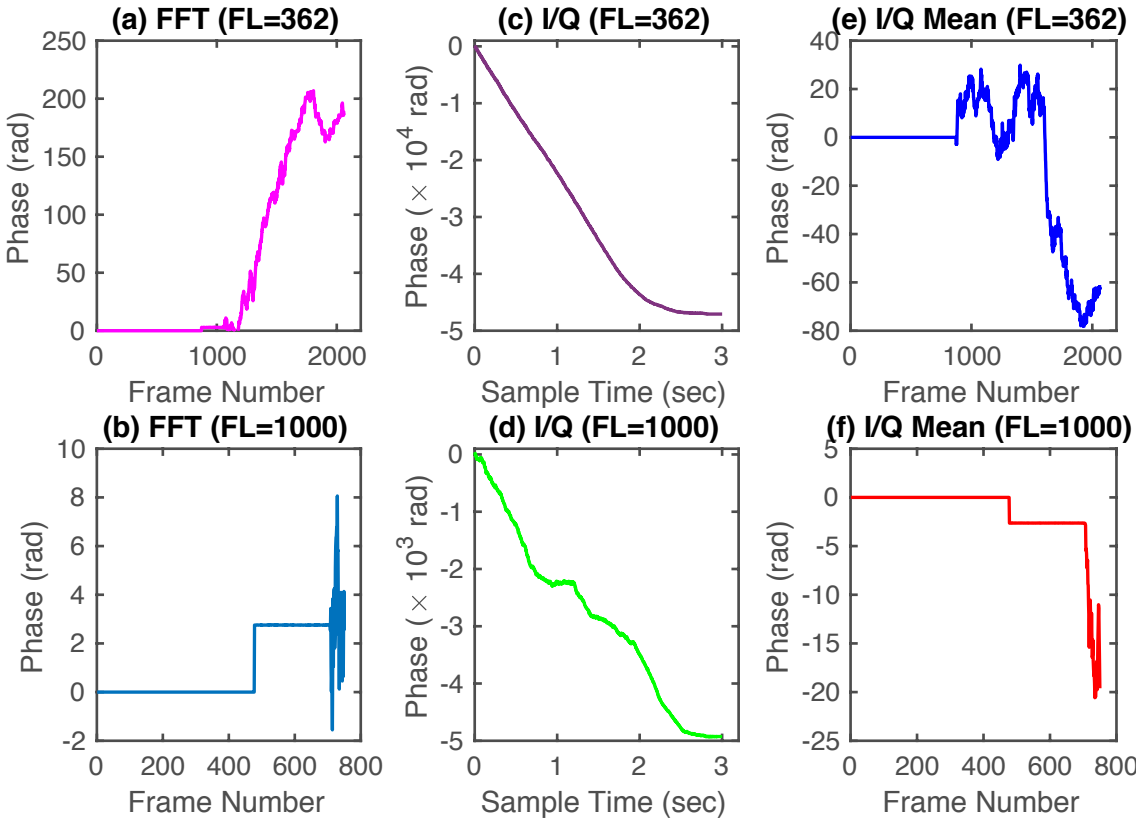

Figure 6.4 Unwrapped phase measurement at fixed position taken at fs/N = 250 kHz with different frame lengths by the FFT and I/Q methods

Apart from the baseband sampling frequency, the frame length of the signal in one burst also affects the received signal. To explore the impact of the frame length, the unwrapped phase measurement showed in Figure 6.4 was done with the baseband sampling frequency of 250 kHz. In Figure 6.4, (a), (c) and (e) present the results of frame length of 362, while Figure 6.4 (b), (d) and (f) display the results for frame length of 1000. In a similar layout to the previous Figure 6.3, Figure 6.4 (a) and (b) compare the phase measurement results for each frame in the received samples using the FFT method. In comparison, Figure 6.4 (a) gives a more rational phase measurement with a roughly linear increasing curve. Both Figure 6.4 (c) and (d) give the measurement by unwrapping the phase of each sample in a sequence of the entire scanning time. Both of them give a fairly good linear curve, but the one in (c) is smoother. In Figure 6.4 (e) and (f), the unwrapped phase is calculated by taking the mean value of the phase found from

each frame by the I/Q method. The one in (e) produces a more desirable linear curve compared to (f). The above discussion explains the reason why the baseband sampling frequency was set to 500 kHz and the frame length of the signal sent to the radio in one burst was 362. Since the measurement at a single point presents a rational linear curve in both the FFT method and the I/Q method, the phase measurement in two dimensions was taken from the last frame of the data streaming process to fulfill the purpose of real-time results output.

6.3 Two-dimensional Measurement

After examining the viability of the setup in the USRP N210 platform at one fixed scanning location, the experiment of DACI was undertaken to measure the phase shift and the amplitude in two dimensions, i.e., in the rotation direction of the receiver and the elevation of the phantom. One complete scanning in the 2D experimental measurement setup typically involved the receiver to be rotated 64 steps with an angular step size of 0.9° at each elevation. The phantom was moved 64 steps with a linear step size of 0.5 mm. Since the distance from the focal point to the surface of the point detector is about 6 cm, it leads to a 0.94 mm step size along the rotation direction. Consequently, this gives the pixel size of the projected image to be 0.5 $mm \times 0.94\ mm$.

6.3.1 Amplitude Measurement

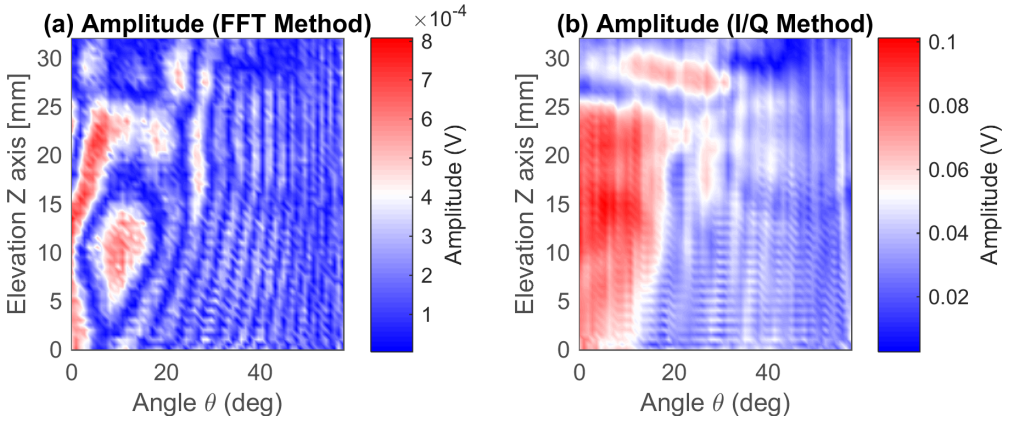

Figure 6.5 2D amplitude measurement using the FFT and I/Q methods

The two-dimensional amplitude measurements using both the FFT and the I/Q method are presented in Figure 6.5. The oscillation between the minimum value and the middle value in the angular range from 20° to 57.6° can be detected. This corresponds to the periodic variation in the amplitude measurement at a fixed position shown in Figure 6.2. The peaks in the amplitude occurs in the angular range from 0° to 20°, where the result output by the I/Q method displays a broader region of peak value compared to the FFT method.

6.3.2 Wrapped Phase

The phase distribution of the measured region in the phantom presents a similar pattern as the simulation results illustrated in Figure 4.3 and Figure 4.17. The wrapped phase in Figure 6.6 (b) typically jumps among $-\pi$, 0 and π. The region in the smaller rotation angle region (0~20°) has a larger and more uniform phase distribution, which is considered to the area where urethra in the phantom exists. On the other hand, the phase deviation in the FFT method shown in Figure 6.5(a) has a similar periodic variation pattern but not exactly the same oscillation range. But still, a larger and smoother phase distribution is detected in the same smaller angle region.

Next, a row vector data was taken across the same elevation $z = 26$ mm to display the unwrapped one-dimensional phase distribution compared to the simulation results. Again, the I/Q method produces a smooth parabolic curve in a similar manner of the simulation results presented in Figure 6.7 and Figure 4.9. On the other hand, the FFT method did not plot a curve as smooth as the I/Q method but it had a similar variation tendency.

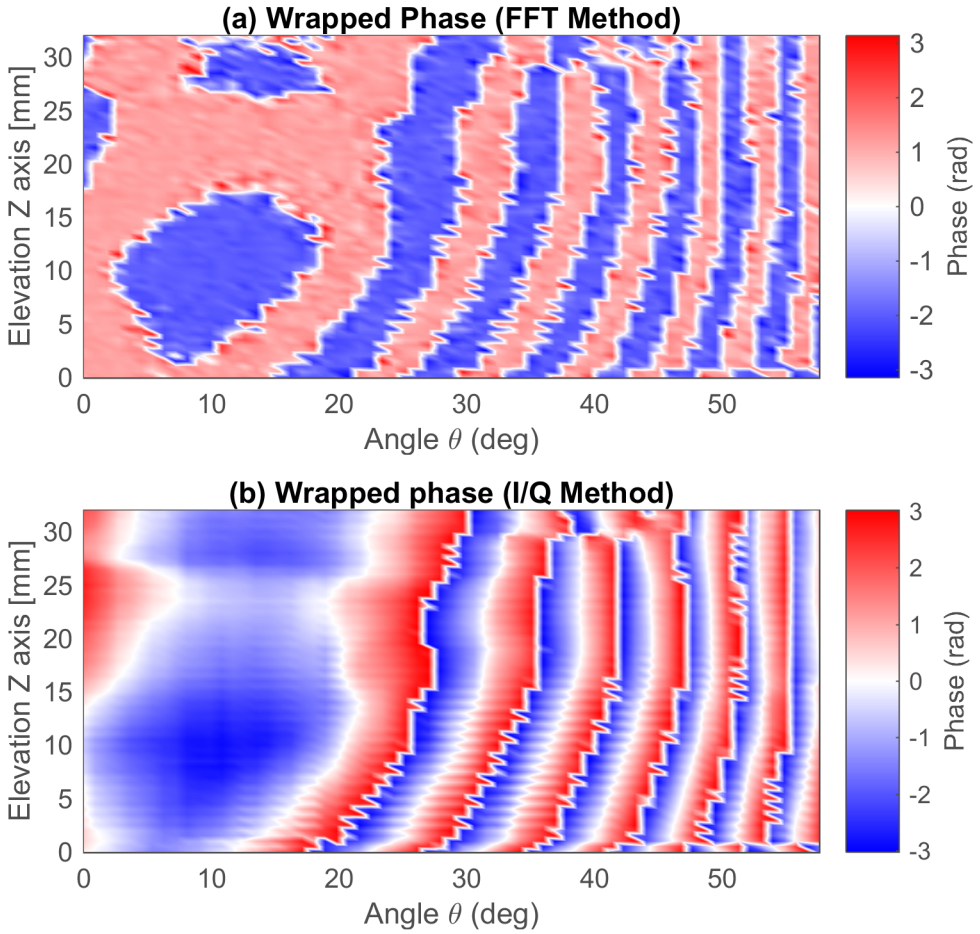

Figure 6.6 2D wrapped phase measurement using the FFT and I/Q methods

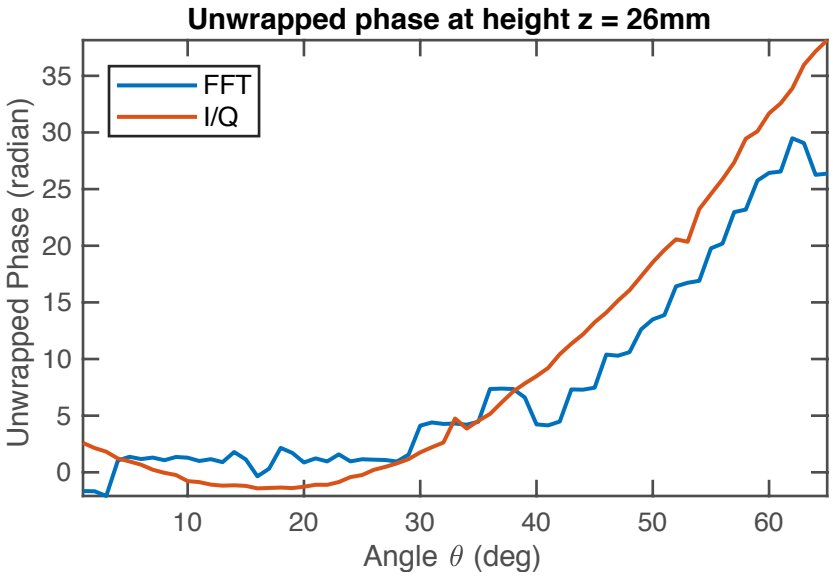

Figure 6.7 Unwrapped phase along the rotation direction at elevation z = 26 mm

6.3.3 Unwrapped Phase

The two dimensional phase unwrapper was downloaded from the General Engineering Research Institute (GERI) at Liverpool John Moores University (LJMU) upon request [78]. The robust phase unwrapper has been widely applied in the area of synthetic radar imaging (SAR), MRI, CT, etc. With many open source options available for 2D phase unwrapping, the 2D-SRNCP algorithm was chosen based on its authority and popularity.

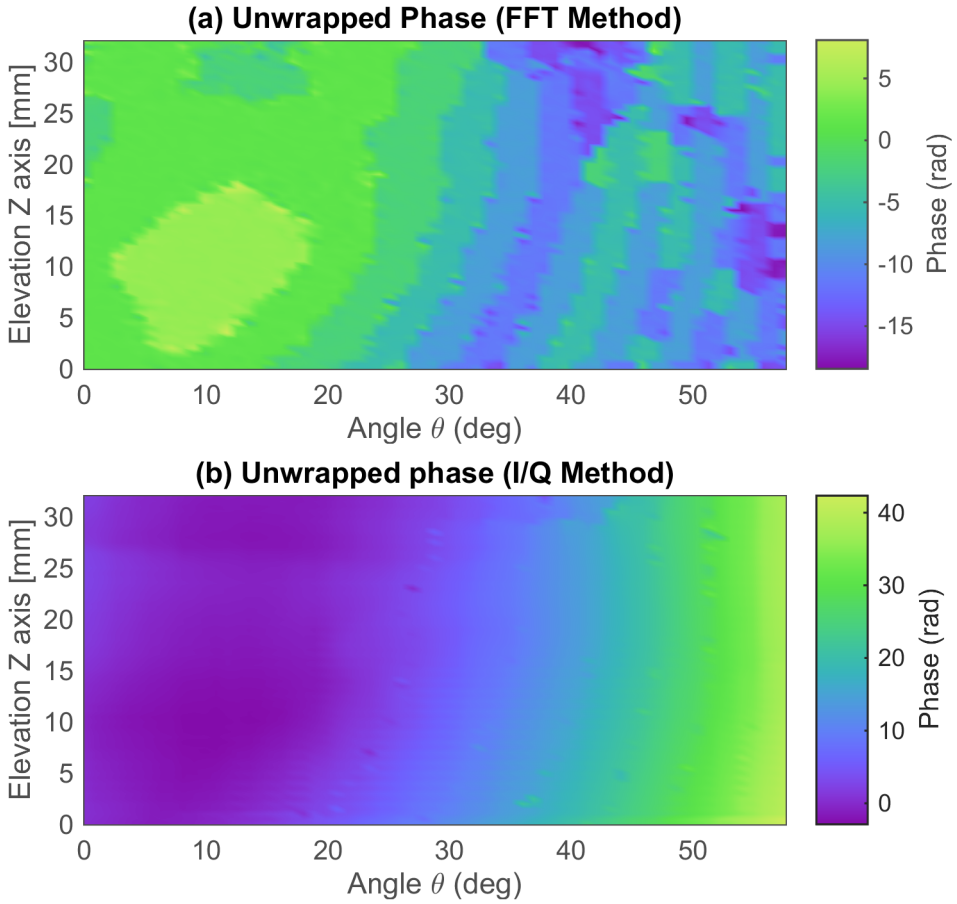

Figure 6.8 2D unwrapped phase measurement

As indicated in Figure 6.7, the unwrapping process of the phase measurement by the I/Q method produces a smooth gradient effect along the rotation direction of the receiver. However, the oscillation of the phase data by FFT method was

more concentrated between $-2\ rad$ to $2\ rad$ rather than $-\pi$ to π. Therefore, the unwrapping results presents a more obvious jump along the rotation direction.

6.3.4 Experiment Results vs Simulation Results

The phase distribution illustrated in Figure 6.6 has some similarity with the simulation results, but not a perfect match. The reason for this is that the simulation results in COMSOL was produced by a much finer mesh size of 163 μm, one sixth of the acoustic wavelength. The spatial resolution of the 2D measurement, $500\ \mu m \times 940\ \mu m$, may not be able to provide a result as good as the simulation. In addition, the deterioration of the prostate phantom may affect the measurement results since its material degraded over time. Therefore, a new phantom will be used for future experiments.

Chapter 7 Results and Discussion

7.1 Discussions

This thesis presents the diffusive acoustic confocal imaging system that measures both the amplitude and the phase information from the diffusively scattered acoustic signal passing through the tissue-mimicking prostate phantom. Following the previous work [44, 45], a new scanning configuration was designed and the concept of the virtual source was introduced. Two simulation software packages were used to design and model the system performance. The USRP device was setup as the signal acquisition device to achieve accurate measurements with improved sampling frequency and its frame synchronization capability. 2D projected images of the amplitude and the phase data of the signal scattered from a fixed virtual source position were measured and found to generally agree with the simulation results.

7.1.1 Presented a New Layout of DACI Suitable for Clinical Use

The current layout of the DACI's proof-of-concept experiment was designed based on earlier work and its geometry was modified to be suitable for the final design for clinical use. It features three components, an acoustic emitter, a focusing mirror and a point receiver. The concept of virtual source was introduced. The virtual source needs to be adjusted to the near surface of the prostate or within the bladder. This enables the acoustic intensity to diffusively scatter in 360° and propagate through the prostate to provide geometrical scanning of the acoustic wave imaging different from the conventional ultrasound. The scattered acoustic rays did not gain much attention in the past in the acoustic imaging field and are usually filtered out. The propagation behavior of these scattered beam through the specimen contains information about the alterations in the media's mechanical properties. This is used in the current work to design the scanning

configuration, which provides a good basis for future practical DACI design enabling the patient to be seated during the exam.

7.1.2 Used ZEMAX and COMSOL to Simulate the System Design and the Performance from a Fixed Virtual Source Position

Two simulation software packages, ZEMAX and COMSOL, were used to model the system design. The amplitude and phase distributions simulated using the two software packages were found to be consistent. In ZEMAX modelling, the parameters to define the media's mechanical properties were set via the wavelength in the water background and the refractive index in different objects. While in COMSOL modelling, the parameters were set directly via the density and the speed of sound in various media. In both simulation packages, the ray tracing algorithm are utilized to study the propagation behaviour of the acoustic beam scattered from the virtual source.

The main results of the system design computer modeling can be summarized as follows. Firstly, the concept of the virtual source was validated since the ray trajectories image show how the acoustic beam scatters into all directions at the virtual source position. The amplitude distribution also proves that scattered intensity is sufficient to carry the phase information. Secondly, the planar locations of lesions are detected on both the amplitude and the phase distribution. In amplitude distribution, the outline of the prostate and the lesions can be distinguished by the intensity level differences. The phase distribution obtained from both ZEMAX and COMSOL presents a similar ring pattern where phase generally varies among $-\pi$, 0 and π. The locations where phase shifts occur are found to correspond to where the material discontinuity interfaces are. Thirdly, the unwrapped phase distribution shows that the total phase variation is accumulated along the travel distance and related to the speed of sound. Therefore, the 1D speed of sound variation was able to be estimated form the 1D

unwrapped phase data. The abrupt shifts detected in the plot corresponds to where the tissues changes are.

In order to achieve a good contrast data in COMSOL modelling, the element size was set to one sixth of the wavelength, which is about 163 μm. In ZEMAX, the number of rays for the simulation was set to the maximum value that the computer is able to process, which is 4×10^9.

7.1.3 Setup the USRP as the Signal Generation and Acquisition Device for DACI

Upon the validation of the concept of the design of the imaging system, the signal generation and acquisition device was set up using the SDR based USRP N210 platform. First of all, SDR technology enables the flexibility of the software implementation and the hardware architecture that benefits the whole system design. With the 100 MS/s master clock rate, the FPGA on the motherboard of the USRP can sample the interpolated signal at a rate 400 times faster than the device used in the previous work, i.e., the National Instruments (NI) PCI-6221 data acquisition board [45]. Secondly, the I/Q signal representation used in the SDR system design enables the phase information to be preserved through the data streaming process. This provides a straightforward interpretation method of the phase difference between the received signal and the transmitted signal. To validate the results, the Fast Fourier transform method was also performed. Thirdly, the frame synchronization with the Barker code was applied to the digital signal to be sent in order to achieve more accurate results. Finally, the frame-based sampling method was used to stream the digital samples from the host computer into the USRP N210.

7.1.4 Conducted 2D Measurements of the Amplitude and the Phase Information of the Acoustic Beam from a Fixed Virtual Source

With the understanding of the hardware structure and the software implementation of the USRP platform, the amplitude and the phase measurement at a stationary point was conducted to explore the effects of the several

combinations of different baseband sampling frequencies and frame lengths. Then the measurement was conducted to obtain the phase and the amplitude information of the probed acoustic beam passing through the specimen from a fixed virtual source along two dimensions, the rotation direction around the virtual source and the elevation direction of moving the phantom up and down. The phase measurement generally agrees with the simulation results, but with some deficiency that is considered to be the deterioration of the phantom material and the lack of finer spatial resolution.

7.2 Future Work

At this phase of the design of DACI, there is still a lot of room for improvement. The direction of the project is definitely geared towards the prototype design of a compact version of DACI.

7.2.1 Upgrade the Rotation Motion Stage

Currently, the rotation stage control over the receiver was realized through the microcontroller board and the microstepping driver. This inexpensive combination functions just fine as commanded. However, a more sophisticated DC servo motor enables a much smoother movement between steps, potentially diminishes the noise triggered by the vibration of the stepper motor when moving the receiver.

7.2.2 Further Improve the USRP's Parameters Setup

In the process of learning how to implement the knowledge to adapt to the data retrieve method, a limitation in the accuracy was considered to be noise in the aquarium that may cause unwanted acoustic beams reflected off the walls and the imaging components to deteriorate the phase information detected. This is due to the fact that there is some minor delay between the transmission and reception ports on the front end of the USRP. Even with the current frame synchronization method, the possibility of the mismatch between the received samples and the

transmitted ones still exist. There is a technique called pulse shaping to limit the noise. At this stage, the complexity of including the related programming code into the GUI is still not satisfying since it greatly increases the processing time between each scanning position that may sacrifice the whole scanning time. Theoretically, it can decrease the bandwidth and decrease the overlap between each sample. However, the necessity of the pulse shaping technique needs further investigation and is definitely a potential part to be included in the signal processing command on the host computer end.

7.2.3 Practical Prototype Design

Solidworks has been used to create the ideal mechanical parts of the future DACI prototype design. Not only the design for the prostate cancer examination and diagnosis, but also one designed for ovaries examination and cancer detection.

Presented in Figure 7.1, the geometry design specifically for prostate examination and disease detection has a flat seating surface upon which a 3-tile array transducer is placed. Ideally, the patient will sit on an acoustic impedance matching medium where the transducer is placed underneath of his backside and each leg will be put on each side of the emitter. A shell holding the emitter and the focusing mirror is placed just above the pelvic bone from which it emits into the bladder creating the virtual source whose intensity passes through the prostate to the detector placed on the backside of the patient. The emitter/mirror assembly is attached to a mechanical handle, which can be extended and shortened by the goniometer according to the shape of the patient. Figure 7.2 illustrates the placement of DACI as a future routine examination tool for prostate disease diagnosis.

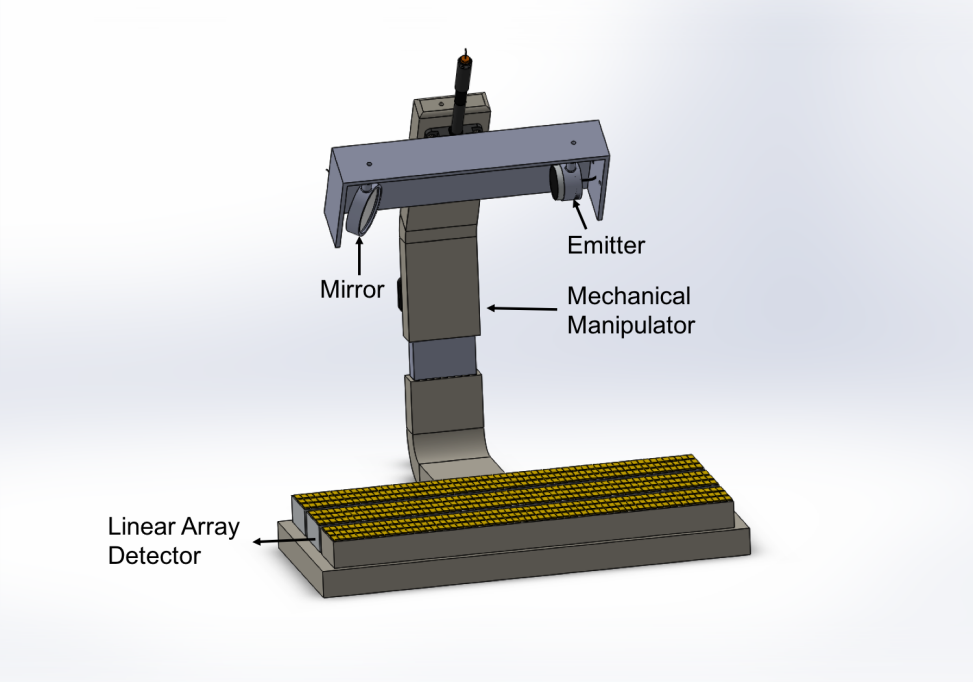

Figure 7.1 DACI geometry design for prostate cancer

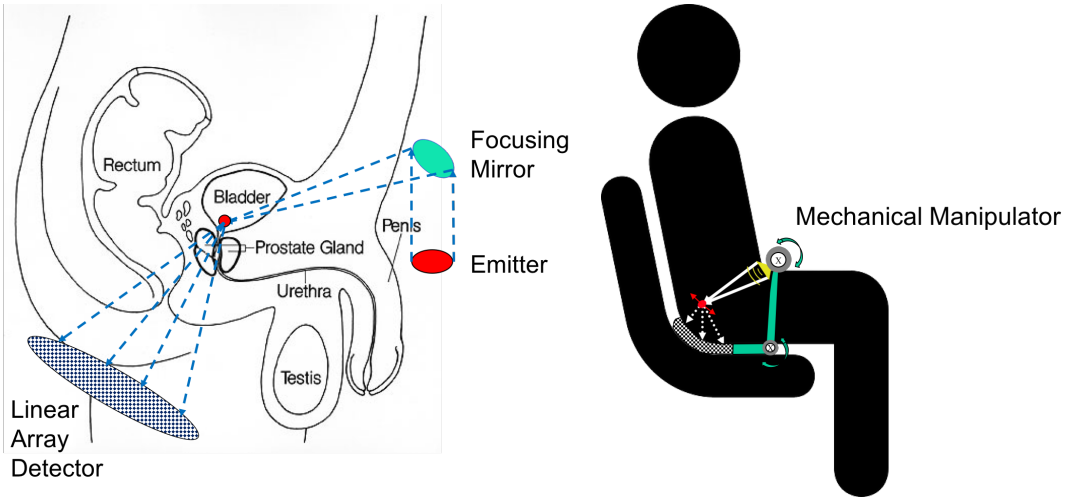

Figure 7.2 The placement of DACI for prostate disease examination [79]

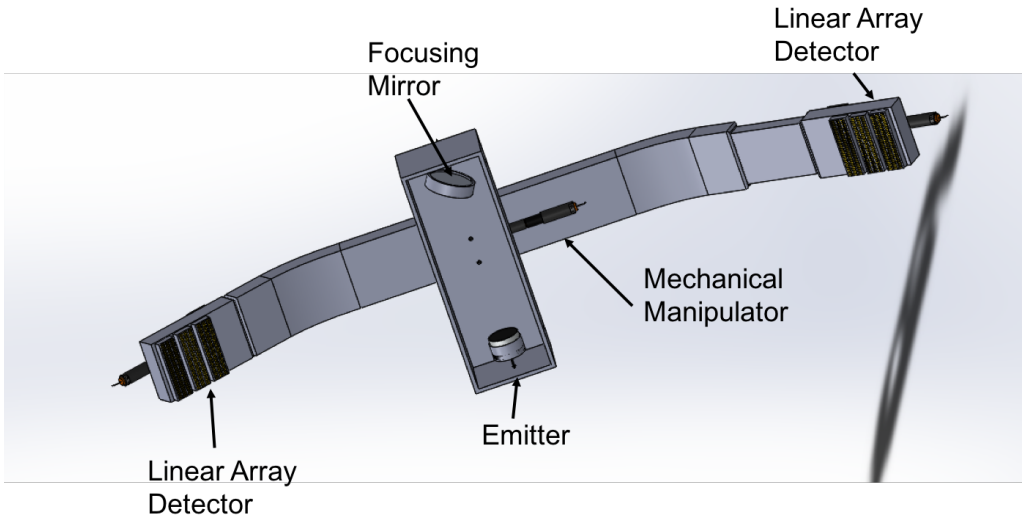

Figure 7.3 DACI geometry design for ovaries cancer diagnose

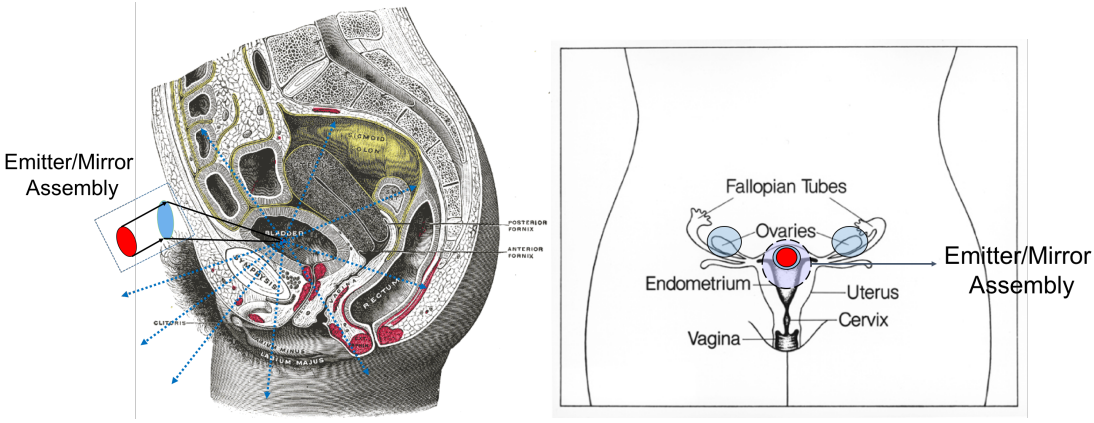

Figure 7.4 The placement of DACI for Ovaries Examination [80, 81]

The geometry configuration for female ovaries disease diagnosis has a similar design illustrated in Figure 7.3. And its placement on human body is displayed in Figure 7.4. The transducers on the end of both sides of the handles are placed on top of the ovaries and receive an acoustic signal from the virtual source in the bladder. The placement of the two detectors can be manipulated by the goniometer attached. The assembly of the emitter and the focusing mirror is placed in front and center of the patient emitting from just above the pelvic bone. Basically, these two designs give a general idea how we integrated the ergonomic considerations and the concept of the current DACI design. In order to give a more

straightforward view of the prototype designs, the short movie clips of both designs are linked in Appendix B: Future Prototype Design of DACI.

7.2.4 Reconstruct the 2D/3D Speed of Sound Variation

An important next step in the future is to reconstruct the 2D/3D speed of sound variation within the prostate phantom. This requires the knowledge of image reconstruction to select an appropriate method. The current scanning geometry only gives one 2D projection images of the prostate phantom. In order to locate the diseased tissues, the ability to fully render the image of the object is essential. The image reconstruction process needs a thoughtful plan of the translation of the virtual source position so that a set of useful projections can be captured as is achieved by the confocal imaging method. The scanning geometry involved plays an important role in terms of the projection path. Various types of image reconstruction need to be reviewed accordingly.

After obtaining the reconstructed phase image, the speed of sound variation within the measured region can be inferred based on the relationship between these two parameters, explained in Equation (2.15). As presented in Figure 4.6 and Figure 4.11, the one-dimensional speed of sound variations in both the ZEMAX and COMSOL models was estimated. The spatial component involved in the equation is basically the travel distance of the acoustic beam under investigation. The travel distance of the acoustic beam that propagates in the water tank includes three segments, i.e., the distance between the emitter and the mirror, the distance from the mirror to the focus probe position and the distance from the probe position to the receiver. For the reconstruction of 2D and 3D speed of sound variation, the spatial component can be solved and the speed of sound at different locations inside the specimen can be found by performing the image reconstruction [45].

7.3 Final conclusions

The general goal of the project is to design an acoustic imaging modality that is able to non-invasively distinguish the diseased tissues from the healthy tissues in

the prostate. In order to achieve that, the speed of sound is considered as the tool to characterize the alterations in the tissues' mechanical properties at different pathological states. This thesis presents a novel acoustic imaging modality that is able to measure the investigated acoustic beam diffusively scattered from a virtual source, which is located within the bladder or at the near surface the prostate. Both the amplitude and phase distributions were exploited with the current scanning configuration immersed in the water aquarium. By investigating the boundary behavior at the material discontinuity interfaces, the phase shift is found to be a function of the speed of sound and the density of the media on both sides of the interface. Also, the unwrapped phase variation along the travel path is linearly related to the speed of sound. Therefore, the 1D unwrapped phase distribution was used to estimate the 1D speed of sound variation, which provides quantitative information regarding the tissue variations. In addition, the amplitude information obtained from the DACI's setup was found to provide improved information compared to the conventional ultrasound. The thesis focused on the demonstration of the concept of virtual source using the simulation models by ZEMAX and COMSOL. The implementation of the USRP N210 platform enabled the development of two signal extraction methods used to interpret the phase and the amplitude data.

In conclusion, the diffusive scattering confocal acoustic imaging system (DACI) uses acoustic signal in the same range as conventional ultrasound but offers a completely different perspective to make contributions to the diagnosis of diseases of the body. The current proof-of-concept design was successful in measuring both the phase and the amplitude information of the acoustic signal passing through the prostate phantom. In the future, the 2D/3D speed of sound needs to be reconstructed to localize the lesions. This system design has a great potentiality to be developed into a practical, easy-to-use and cost-effective clinical device.

Bibliography

[1] Canadian Cancer Society's Advisory Committee on Cancer Statistics (2017). *Canadian Cancer Statistics 2017*. Available: http://www.cancer.ca/~/media/cancer.ca/CW/publications/Canadian Cancer Statistics/Canadian-Cancer-Statistics-2017-EN.pdf

[2] R. L. Siegel, K. D. Miller, and A. Jemal, "Cancer statistics, 2017," (in en), *CA: A Cancer Journal for Clinicians,* vol. 67, no. 1, pp. 7-30, 2017.

[3] U.S Food & Drug Administration, (May 27, 2016). *FDA approves new diagnostic imaging agent to detect recurrent prostate cancer*. Available: https://www.fda.gov/NewsEvents/Newsroom/PressAnnouncements/ucm503920.htm, (Accessed on: Dec. 9th, 2017)

[4] K. Bouchelouche, S. T. Tagawa, S. J. Goldsmith, B. Turkbey, J. Capala, and P. Choyke, "PET/CT imaging and radioimmunotherapy of prostate cancer," 2011, vol. 41, pp. 29-44: Elsevier.

[5] C. J. Harvey, J. Pilcher, J. Richenberg, U. Patel, and F. Frauscher, "Applications of transrectal ultrasound in prostate cancer," *The British journal of radiology,* 2014.

[6] S. Phipps, T. H. J. Yang, F. K. Habib, R. L. Reuben, and S. A. McNeill, "Measurement of tissue mechanical characteristics to distinguish between benign and malignant prostatic disease," *Urology,* vol. 66, no. 2, pp. 447-450, Aug 2005.

[7] R. S. C. Cobbold, *Foundations of biomedical ultrasound*. Oxford University Press, 2006, pp. 3-324.

[8] J. Mamou and M. L. Oelze, *Quantitative ultrasound in soft tissues*. Springer, 2013, pp. 21-42.

[9] J. W. S. B. Rayleigh, *The theory of sound*. Macmillan, 1896.

[10] J. Woo, "A short history of the development of ultrasound in obstetrics and gynecology," *See* http://www.ob-ultrasound.net/history1.html *(last checked 14 May 2017),* 2002.

[11] F. A. Firestone, "Flaw detecting device and measuring instrument," ed: Google Patents, 1942.

[12] K. T. Dussik, "Über die Möglichkeit, hochfrequente mechanische Schwingungen als diagnostisches Hilfsmittel zu verwerten," *Zeitschrift für die gesamte Neurologie und Psychiatrie,* vol. 174, no. 1, pp. 153-168, 1942.

[13] G. D. Ludwig and F. W. Struthers, "Considerations underlying the use of ultrasound to detect gallstones and foreign bodies in tissue," ed: NAVAL MEDICAL RESEARCH INST BETHESDA MD, 1949.

[14] G. D. Ludwig, "The velocity of sound through tissues and the acoustic impedance of tissues," *The Journal of the Acoustical Society of America,* vol. 22, no. 6, pp. 862-866, 1950.

[15] J. J. Wild and D. Neal, "Use of high-frequency ultrasonic waves for detecting changes of texture in living tissues," *The Lancet,* vol. 257, no. 6656, pp. 655-657, 1951.

[16] J. J. Wild and J. M. Reid, "Application of echo-ranging techniques to the determination of structure of biological tissues," *Science (New York, NY),* vol. 115, no. 2983, pp. 226-230, 1952.

[17] J. J. Wild and J. M. Reid, "Further pilot echographic studies on the histologic structure of tumors of the living intact human breast," *The American journal of pathology,* vol. 28, no. 5, p. 839, 1952.

[18] J. J. Wild, "The scientific discovery of sonic reflection of soft tissue and application of ultrasound to diagnostic medicine and tumor screening," ed. Brighton, England: Third Meeting of the World Federation for Ultrasound In Medicine and Biology, 1982.

[19] D. H. Howry and W. R. Bliss, "Ultrasonic visualization of soft tissue structures of the body," *The Journal of laboratory and clinical medicine,* vol. 40, no. 4, pp. 579-592, 1952.

[20] J. H. Holmes, D. H. Howry, G. J. Posakony, and C. R. Cushman, "The ultrasonic visualization of soft tissue structures in the human body," *Transactions of the American Clinical and Climatological Association,* vol. 66, p. 208, 1955.

[21] J. H. Holmes, W. Wright, E. P. Meyer, G. J. Posakony, and D. H. Howry, "Ultrasonic contact scanner for diagnostic application," *The American journal of medical electronics,* vol. 4, no. 4, pp. 147-152, 1964.

[22] J. H. Holmes, "Ultrasonic studies of the bladder," *The Journal of urology,* vol. 97, no. 4, pp. 654-663, 1967.

[23] G. Kossoff, W. J. Garrett, and G. Radovanovich, "Grey scale echography in obstetrics and gynaecology," *Journal of Medical Imaging and Radiation Oncology,* vol. 18, no. 1, pp. 63-111, 1974.

[24] Y.-c. Fung, *Biomechanics: mechanical properties of living tissues*, 2nd ed. Springer-Verlag New York, 1993, pp. 242-314.

[25] S. Fields and F. Dunn, "Correlation of echographic visualizability of tissue with biological composition and physiological state," *Acoustical Society of America,* Sept. 1973.

[26] W. D. O'Brien, "The relationship between collagen and ultrasonic attenuation and velocity in tissue," *Ultrasonics Int,* vol. 77, pp. 194-205, 1977.

[27] J. D. Pohlhammer and W. D. O'Brien, "The relationship between ultrasonic attenuation and speed in tissues and constituents: water, collagen, protein and fat," *Medical physics of CT and ultrasound: Tissue imaging and characterization,* no. 6, 1980.

[28] S. A. Goss and W. D. O'Brien Jr., "Direct ultrasonic velocity measurements of mammalian collagen threads," *Acoustical Society of America,* Feb. 1979.

[29] S. A. Goss and F. Dunn, "Ultrasonic propagation properties of collagen," *Physics in medicine and biology,* vol. 25, p. 827, Sept. 1980.

[30] J. C. Bamber, "Speed of sound," in *Physical Principles of Medical Ultrasonics*, C. R. Hill, J. C. Bamber, and G. R. t. Haar, Eds. Second ed. Chichester, UK: John Wiley & Sons, Ltd, 2005, pp. 200-224.

[31] J. F. Greenleaf, S. A. Johnson, W. F. Samayoa, and F. A. Duck, "Algebraic reconstruction of spatial distributions of acoustic velocities in tissue from their time-of-flight profiles," in *Acoustical holography*: Springer, 1975, pp. 71-90.

[32] J. F. Greenleaf and R. C. Bahn, "CLINICAL IMAGING WITH TRANSMISSIVE ULTRASONIC COMPUTERIZED-TOMOGRAPHY," *IEEE Transactions on Biomedical Engineering,* vol. 28, no. 2, pp. 177-185, 1981.

[33] I. D. Ansell, "Histopathology of prostatic tumors," in *The Endocrinology of Prostate Tumours*, R. Ghanadian, Ed. 1st ed.: Springer Netherlands, 1983, pp. 15-33.

[34] R. B. Shah and M. Zhou, "Anatomy and Normal Histology of the Prostate Pertinent to Biopsy Practice," in *Prostate Biopsy Interpretation: An Illustrated Guide*: Springer, 2012, pp. 1-10.

[35] C. Morrison, J. Thornhill, and E. Gaffney, "The connective tissue framework in the normal prostate, BPH and prostate cancer: analysis by scanning electron microscopy after cellular digestion," *Urological Research,* vol. 28, no. 5, pp. 304-307, Oct 2000.

[36] T. A. Krouskop, T. M. Wheeler, F. Kallel, B. S. Garra, and T. Hall, "Elastic moduli of breast and prostate tissues under compression," *Ultrasonic Imaging,* vol. 20, no. 4, pp. 260-274, Oct 1998.

[37] F. A. Duck, *Physical Properties of Tissues*. Academic Press, 1990, pp. 73-124.

[38] K. K. Shung and G. A. Thieme, *Ultrasonic scattering in biological tissues*. CRC press, 1992.

[39] Kaye & Laby Online, "2.4.1 The speed and attenuation of sound," Tables of Physical & Chemical Constants,16th ed.: National Physical Library, 2005. [Online]. Available: www.kayelaby.npl.co.uk.

[40] A. Zielinski, "ELEC 571 A01 Underwater Acoustic Systems," Course Notes, 2013.

[41] R. A. Herring, "Confocal scanning holography microscope," ed: Google Patents, 2009.

[42] S. Lai, R. A. McLeod, P. Jacquemin, S. Atalick, and R. Herring, "An algorithm for 3-D refractive index measurement in holographic confocal microscopy," *Ultramicroscopy,* vol. 107, no. 2, pp. 196-201, 2007.

[43] R. A. Herring, P. Jacquemin, B. D. Sawicka, and S. Atalick, "Developing a Confocal Acoustic Holography Microscope for non-invasive 3D temperature and composition measurements," *Ultramicroscopy,* vol. 109, no. 7, pp. 830-836, 2009.

[44] S. Atalick, "Confocal acoustic holography for non-invasive 3D temperature and composition measurement," M.A.Sc, University of Victoria, 2007.

[45] K. McCaugherty, "Spatially-filtered continuous-wave acoustic tomography for breast cancer detection," M.A.Sc, University of Victoria, 2012.

[46] Olympus NDT, (2011). *Ultrasonic Transducers Technical Notes*. Available: https://www.olympus-ims.com/en/resources/white-papers/ultrasonic-transducer-technical-notes/, (Accessed on: Oct.11st., 2017)

[47] M. B. Zerhouni and M. Rachedine, "Ultrasonic calibration material and method," ed: Google Patents, 1993.

[48] Computerized Imaging Reference Systems, Inc., (2013). *Tissue Equivalent Ultrasound Prostate Phantom Model 053S, 053L & 053L-EF*. Available: http://www.cirsinc.com/products/new/77/tissue-equivalent-ultrasound-prostate-phantom/?details=images, (Accessed on: July 18th 2017)

[49] A. M. Wyglinski and D. Pu, *Digital communication systems engineering with software-defined radio*. Artech House, 2013, pp. 131-152.

[50] R. H. Hosking, Software-Defined Radio Handbook, 13th ed. NJ, United States: Pentek, Inc., 2017. [Online]. Available: http://www.pentek.com/pildocs/8363/techother/DGTLRCVRHBK43.PDF.

[51] Ettus Research. *USRP Hardware Driver and USRP Manual: UHD and USRP Manual*. Available: files.ettus.com/manual/md_usrp2_build_instructions.html, (Accessed on: Aug. 2nd, 2017)

[52] Ettus Research. *USRP Hardware Driver and USRP Manual: USRP 2 and N2x0 Series*. Available: http://files.ettus.com/manual/page_usrp2, (Accessed on: Aug. 2nd, 2017)

[53] National Instrument, (Mar 30, 2016). *What is I/Q Data?* Available: http://www.ni.com/tutorial/4805/en/, (Accessed on: June 29th, 2017)

[54] National Instrument, (2013). *A Digital Downconverter for the NI 5734*. Available: http://www.ni.com/example/31525/en/, (Accessed on: Aug. 17th, 2017)

[55] N. Pandeya and N. Temple. (2016). *About USRP Bandwidths and Sampling Rates*. Available: https://kb.ettus.com/About_USRP_Bandwidths_and_Sampling_Rates, (Accessed on: June. 28th, 2017)

[56] Ettus Research, (2017). *LFRX Daughterboard 0-30 MHz Rx*. Available: https://www.ettus.com/product/details/LFRX, (Accessed on: Aug. 17th, 2017)

[57] Ettus Research, (2017). *LFTX/LFRX*. Available: https://kb.ettus.com/LFTX/LFRX, (Accessed on: Aug. 1st, 2017)

[58] Mathworks, (2017). *Sample- and Frame-Based Concepts*. Available: https://www.mathworks.com/help/dsp/ug/sample-and-frame-based-concepts.html, (Accessed on: Aug. 7th, 2017)

[59] E. G. Williams, *Fourier acoustics: sound radiation and nearfield acoustical holography*. Academic press, 1999, pp. 1-13.

[60] National Instruments, (2016). *Understanding FFTs and Windowing*. Available: http://www.ni.com/white-paper/4844/en/, (Accessed on: Aug. 12nd, 2017)

[61] N.-H. Kim. Zemax LLC, (2015). *How to Create a Simple Non-Sequential System*. Available: http://www.zemax.com/os/resources/learn/knowledgebase/how-to-create-a-simple-non-sequential-system, (Accessed on: Aug. 14th, 2017)

[62] D. Hill. Zemax LLC, (2005). *How To Enter Glass Data at Specific Wavelengths*. Available: http://www.zemax.com/os/resources/learn/knowledgebase/how-to-enter-glass-data-at-specific-wavelengths, (Accessed on: Aug. 14th, 2017)

[63] A. Arora. Zemax LLC, (2007). *How to Model Scattering Efficiently*. Available: http://zemax.com/os/resources/learn/knowledgebase/how-to-model-scattering-efficiently, (Accessed on: Aug. 14th, 2017)

[64] S. Gangadhara. Zemax LLC, (2009). *How to Identify Specific Rays Using Filter Strings*. Available: http://www.zemax.com/os/resources/learn/knowledgebase/how-to-identify-specific-rays-using-filter-strings, (Accessed on: Aug. 14th, 2017)

[65] COMSOL, (2017). *COMSOL Multiphysics® The Platform for Physics-Based Modeling and Simulation*. Available: https://www.comsol.com/comsol-multiphysics, (Accessed on: Aug. 14th, 2017)

[66] COMSOL, (2017). *Acoustics Module Software for Acoustics and Vibration Analysis*. Available: https://www.comsol.com/acoustics-module, (Accessed on: Aug. 14th, 2017)

[67] *Acoustics Module User's Guide*, COMSOL 5.0 ed. COMSOL, Oct 2014.

[68] *COMSOL Multiphysics Model Library Manual*, COMSOL 5.0 ed. COMSOL, Oct 2014.

[69] COMSOL Multiphysics, (2014). *Acoustics Module Model Library Manual (COMSOL 5.0 ed.)*. (Accessed on: Sept. 11st, 2017)

[70] LIN ENGINEERING, "1.8° Size 17 High Torque Motor 4218," 454467, Distributed by: Jameco Electronics, Accessed on: Aug. 21st, 2017.

[71] Arduino, (2017). *What is Arduino?* Available: https://www.arduino.cc/en/Guide/Introduction, (Accessed on: Aug. 20th, 2017)

[72] Atmel Corporation, "8-bit AVR Microcontroller with 4/8/16/32K Bytes In-System Programmable Flash," ATmega48PA/88PA/168PA/328P, 2009.

[73] The MathWorks, Inc., (2017). *Arduino Support from MATLAB*. Available: https://www.mathworks.com/hardware-support/arduino-matlab.html, (Accessed on: Aug. 20th, 2017)

[74] Newport Corporation, (2017). *High Speed LTA Motorized Actuator, 50 mm travel, LTA, 3/8-40 thread*. Available: https://www.newport.com/p/LTA-HS, (Accessed on: Aug. 21st, 2017)

[75] Newport Corporation, (1999). *ESP300 Motion Controller/Driver User's Manual*. Available: http://forums.ni.com/attachments/ni/170/209840/1/ESP300.pdf, (Accessed on: Aug. 21st, 2017)

[76] The MathWorks, Inc., (2017). *Support Package Hardware Setup*. Available: https://www.mathworks.com/help/supportpkg/usrpradio/ug/support-package-hardware-setup.html, (Accessed on: Aug. 22nd, 2017)

[77] JDS Uniphase Corporation, "Helium-Neon Laser Heads 1100 Series," 2005.

[78] Liverpool John Moores University, (2017). *Phase unwrapping*. Available: https://www.ljmu.ac.uk/research/centres-and-institutes/faculty-of-engineering-and-technology-research-institute/geri/phase-unwrapping, (Accessed on: Sept. 5th, 2017)

[79] National Cancer Institute Visuals Online, (2001). *Prostate*. Available: https://visualsonline.cancer.gov/details.cfm?imageid=1779, (Accessed on: Oct. 16th, 2017)

[80] Henry Gray (1825-1861). Bartleby.com: Gray's Anatomy, (1918). *Anatomy of the Human Body*. Available: http://www.bartleby.com/107/illusl166.html, (Accessed on: Oct. 16th, 2017)

[81] National Cancer Institute Visuals Online, (2001). *Reproductive (Female)* [B&W, Medical Illustration]. Available: https://visualsonline.cancer.gov/details.cfm?imageid=1783, (Accessed on: Oct. 16th, 2017)

Appendix A: Verify MATLAB Connection to USRP Radio

```
probesdru

ans =

    'Win32; Microsoft Visual C++ version 12.0; Boost_105600;
UHD_003.009.004-vendor

     -- Opening a USRP2/N-Series device...
     -- Current recv frame size: 1472 bytes
     -- Current send frame size: 1472 bytes

     UHD Warning:
         The MTU (1472) is larger than the FastSendDatagramThreshold
(1024)!
         This will negatively affect the transmit performance.
         See the transport application notes for more detail.
     -- Creating WSA UDP transport for 192.168.10.2:49156
     -- Creating WSA UDP transport for 192.168.10.2:49158
     -- Creating WSA UDP transport for 192.168.10.2:49157
     -- Creating WSA UDP transport for 192.168.10.2:49159
      ____________________________________________________
     /
     |       Device: USRP2 / N-Series Device
     |     ______________________________________________________
     |    /
     |    |       Mboard: N210r4
     |    |   hardware: 2577
     |    |   mac-addr: 00:80:2f:0a:e3:07
     |    |   ip-addr: 192.168.10.2
     |    |   subnet: 255.255.255.255
     |    |   gateway: 255.255.255.255
     |    |   gpsdo: none
     |    |   serial: F47153
     |    |   FW Version: 12.4
     |    |   FPGA Version: 11.1
     |    |
     |    |   Time sources: none, external, _external_, mimo
     |    |   Clock sources: internal, external, mimo
     |    |   Sensors: mimo_locked, ref_locked
     |    |     ____________________________________________________
     |    |    /
     |    |    |       RX DSP: 0
     |    |    |   Freq range: -50.000 to 50.000 MHz
     |    |     ____________________________________________________
     |    |    /
     |    |    |       RX DSP: 1
     |    |    |   Freq range: -50.000 to 50.000 MHz
     |    |     ____________________________________________________
     |    |    /
     |    |    |       RX Dboard: A
     |    |    |   ID: LF RX (0x000f)
```

```
      |   |   |   Serial: E3R13Y5RL
      |   |   |
_____________________________________________________
      |   |   |    /
      |   |   |   |       RX Frontend: AB
      |   |   |   |   Name: LFRX (AB)
      |   |   |   |   Antennas:
      |   |   |   |   Sensors:
      |   |   |   |   Freq range: -32.000 to 32.000 MHz
      |   |   |   |   Gain Elements: None
      |   |   |   |   Bandwidth range: 64000000.0 to 64000000.0 step 0.0
Hz
      |   |   |   |   Connection Type: IQ
      |   |   |   |   Uses LO offset: No
      |   |   |
_____________________________________________________
      |   |   |    /
      |   |   |   |       RX Frontend: BA
      |   |   |   |   Name: LFRX (BA)
      |   |   |   |   Antennas:
      |   |   |   |   Sensors:
      |   |   |   |   Freq range: -32.000 to 32.000 MHz
      |   |   |   |   Gain Elements: None
      |   |   |   |   Bandwidth range: 64000000.0 to 64000000.0 step 0.0
Hz
      |   |   |   |   Connection Type: QI
      |   |   |   |   Uses LO offset: No
      |   |   |
_____________________________________________________
      |   |   |    /
      |   |   |   |       RX Frontend: A
      |   |   |   |   Name: LFRX (A)
      |   |   |   |   Antennas:
      |   |   |   |   Sensors:
      |   |   |   |   Freq range: -32.000 to 32.000 MHz
      |   |   |   |   Gain Elements: None
      |   |   |   |   Bandwidth range: 32000000.0 to 32000000.0 step 0.0
Hz
      |   |   |   |   Connection Type: I
      |   |   |   |   Uses LO offset: No
      |   |   |
_____________________________________________________
      |   |   |    /
      |   |   |   |       RX Frontend: B
      |   |   |   |   Name: LFRX (B)
      |   |   |   |   Antennas:
      |   |   |   |   Sensors:
      |   |   |   |   Freq range: -32.000 to 32.000 MHz
      |   |   |   |   Gain Elements: None
      |   |   |   |   Bandwidth range: 32000000.0 to 32000000.0 step 0.0
Hz
      |   |   |   |   Connection Type: Q
      |   |   |   |   Uses LO offset: No
      |   |   |
_____________________________________________________
```

```
      |   |   |    /
      |   |   |   |       RX Codec: A
      |   |   |   |   Name: ads62p44
      |   |   |   |   Gain range digital: 0.0 to 6.0 step 0.5 dB
      |   |   |   |   Gain range fine: 0.0 to 0.5 step 0.1 dB
      |   |   |    ____________________________________________________
      |   |   |   /
      |   |   |   |       TX DSP: 0
      |   |   |   |   Freq range: -50.000 to 50.000 MHz
      |   |   |    ____________________________________________________
      |   |   |   /
      |   |   |   |       TX Dboard: A
      |   |   |   |   ID: LF TX (0x000e)
      |   |   |   |   Serial: E1R14X3TL
      |   |   |   |
_____________________________________________________________
      |   |   |   /
      |   |   |   |       TX Frontend: AB
      |   |   |   |   Name: LFTX (AB)
      |   |   |   |   Antennas:
      |   |   |   |   Sensors:
      |   |   |   |   Freq range: -32.000 to 32.000 MHz
      |   |   |   |   Gain Elements: None
      |   |   |   |   Bandwidth range: 64000000.0 to 64000000.0 step 0.0
Hz
      |   |   |   |   Connection Type: IQ
      |   |   |   |   Uses LO offset: No
      |   |   |   |
_____________________________________________________________
      |   |   |   /
      |   |   |   |       TX Frontend: BA
      |   |   |   |   Name: LFTX (BA)
      |   |   |   |   Antennas:
      |   |   |   |   Sensors:
      |   |   |   |   Freq range: -32.000 to 32.000 MHz
      |   |   |   |   Gain Elements: None
      |   |   |   |   Bandwidth range: 64000000.0 to 64000000.0 step 0.0
Hz
      |   |   |   |   Connection Type: QI
      |   |   |   |   Uses LO offset: No
      |   |   |   |
_____________________________________________________________
      |   |   |   /
      |   |   |   |       TX Frontend: A
      |   |   |   |   Name: LFTX (A)
      |   |   |   |   Antennas:
      |   |   |   |   Sensors:
      |   |   |   |   Freq range: -32.000 to 32.000 MHz
      |   |   |   |   Gain Elements: None
      |   |   |   |   Bandwidth range: 32000000.0 to 32000000.0 step 0.0
Hz
      |   |   |   |   Connection Type: I
      |   |   |   |   Uses LO offset: No
      |   |   |   |
_____________________________________________________________
```

```
      |   |   |    /
      |   |   |   |       TX Frontend: B
      |   |   |   |   Name: LFTX (B)
      |   |   |   |   Antennas:
      |   |   |   |   Sensors:
      |   |   |   |   Freq range: -32.000 to 32.000 MHz
      |   |   |   |   Gain Elements: None
      |   |   |   |   Bandwidth range: 32000000.0 to 32000000.0 step 0.0
Hz
      |   |   |   |   Connection Type: Q
      |   |   |   |   Uses LO offset: No
      |   |   |
_____________________________________________________
      |   |   |    /
      |   |   |   |       TX Codec: A
      |   |   |   |   Name: ad9777
      |   |   |   |   Gain Elements: None
```

Appendix B: Future Prototype Design of DACI

The short movie clip for better understanding of the future design for prostate diseases diagnosis is linked below:

https://www.dropbox.com/s/4e9u5pz66b3fj8z/DACI_prototype_prostate_RotationView.avi?dl=0 ,

whereas the one for the ovaries disease diagnosis is given in the following link: https://www.dropbox.com/s/xmiftlpqamgfu8z/Ovaries%20_Examination_Configuration_final.avi?dl=0